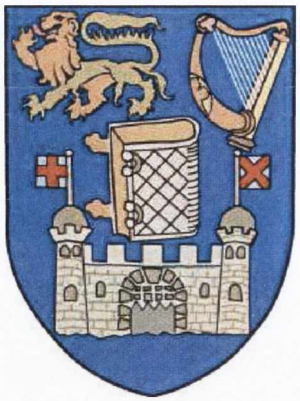

Electronic Transport on Carbon Nanotube Networks: A Multiscale Computational Approach

By

Luiz Felipe C. Pereira

A Thesis Submitted for the Degree of
Doctor of Philosophy

School of Physics

University of Dublin
Trinity College

2011

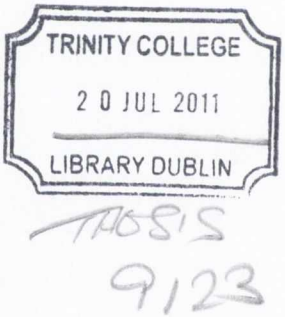

Declaration

I, Luiz Felipe C. Pereira, hereby declare that this dissertation has not been submitted as an exercise for a degree at this or any other University.

It comprises work performed entirely by myself during the course of my Ph.D. studies at Trinity College Dublin. I was involved in a number of collaborations, and where it is appropriate my collaborators are acknowledged for their contributions.

A copy of this thesis may be lended or copied by the Trinity College Library upon request by a third party provided it spans single copies made for study purposes only, subject to normal conditions of acknowledgement.

Summary

Carbon is arguably the most versatile of chemical elements. For the last 25 years research on carbon nanostrutures has been one of the most active areas of science. Carbon-based nanoelectronics is the most promising alternative to replace the ageing silicon-based technologies. In particular, carbon nanotubes present remarkable physical properties such as very low electrical resistance and very high mechanical strength. These characteristics have led to the development of nanotube composites which in turn led to the fabrication of nanotube network films. Films produced by deposition of carbon nanotubes show extraordinary electric conductance and mechanical resistance, making them excellent candidates for the development of flexible electronic devices. A nanotube film contains a complex interconnected network of randomly distributed nanotubes and bundles. The electronic transport characteristics of nanotube networks is defined by a combination of intrinsic nanotube transport properties with the morphology of the random network. Electrons can travel along a single nanotube with very low resistance, but have to tunnel through junctions between individual tubes. The junction resistance is considerably higher than the intrinsic resistance along a typical carbon nanotube. The production of transparent electrodes to be utilised in novel flexible displays requires very high electrical conductivities. Chemical treatments can be applied to lower the junctions resistance but the morphology of the network itself plays a significant role in the resistivity of nanotube films.

This work is focused on modelling the electronic transport properties of carbon nanotube films. We have aimed at developing a computationally efficient framework capable of modelling electronic transport on disordered nanotube networks. The approach developed consists of tackling the problem from two different length scales. On a macroscopic level, carbon nanotubes are modelled as rigid rods of

specified length and diameter. Disordered networks are generated by randomly distributing rods inside a containing volume representing the film. Within this approach it has been found that the connectivity of the networks scales universally with the volume fraction of the films, as well as with the aspect ratio of the rods. Meanwhile, in a microscopic level, nanotubes are described within an atomistic semi-empirical Hamiltonian. With the application of Green function methods, networks consisting of thousands of nanotubes have been simulated, and their conductance calculated. The combination of both length scales leads to a multiscale model of electronic transport through carbon nanotube networks. Theoretical predictions were compared and combined with experimental results providing an estimate for the average inter-tube resistance, which is in accordance with independent experimental studies. Furthermore, by considering a purely ballistic transport regime we have been able to estimate an upper bound for the conductivity of carbon nanotube films. The maximum conductivity calculated was found to scale universally with the density of the network, as well as the average length and diameter of the nanotubes and bundles in the film. When compared to the best experimental values reported our results indicate that nanotube films are reaching their conductivity limit. Furthermore, our simulations lead to the conclusion that metallic nanowire films (other than nanotubes) are better suited for applications in flexible displays. As an extension of the developed models we have considered two further applications. First, it was found that, in spite of their good electronic conductance, nanowire networks are not suitable as a medium to facilitate magnetic coupling. Finally, by considering a capacitive network model, we have been able to reproduce the onset of local electric activation observed in experiments with silver nanowire films.

Acknowledgements

I must begin by thanking my supervisor, Dr. Mauro Ferreira, for his guidance, enthusiasm, patience and support throughout the last four years. Mauro has given me the opportunity to study under his guidance and secured the financial support required. For these I will be always grateful. It has been a pleasure to work with Mauro over these past years, and it will be an honour to keep up with our friendship in the many years to come.

I would like to thank Dr. Claudia G. Rocha for teaching me so many things about carbon nanotubes in my early Dublin days. Also, I would like to thank Claudia for her hospitality in Niterói. My former colleagues Dr. Andrew Wall and Dr. David Kirwan are duly acknowledged for the entertaining environment provided. Thanks go to my colleague Stephen Power for sitting through my endless practice talks.

I would like to thank Prof. Stefano Sanvito and his group, in particular Dr. Tom Archer, for sharing computational resources so generously and for providing such an stimulating work environment.

On a personal note, I must thank my family and friends in Brazil. I could not have gone this far without their support. I must also express my gratitude to Laura for her love and support. Life would not be as exciting without her.

Contents

List of Peer Reviewed Publications Resulting from this Work

- P.E. Lyons, S. De, F. Blighe, V. Nicolosi, **Luiz F.C. Pereira**, M.S. Ferreira, and J.N. Coleman. The relationship between network morphology and conductivity in nanotube films. *Journal of Applied Physics*, **104**, 044302, 2008.

- **L.F.C. Pereira**, C.G. Rocha, A. Latgé, J.N. Coleman, and M.S. Ferreira. Upper bound for the conductivity of nanotube networks. *Applied Physics Letters*, **95**, 123106, 2009.
  (Research Highlights, Nature Nanotechnology, doi:10.1038/nnano.2009.316)

- **Luiz F.C. Pereira**, C.G. Rocha, A. Latgé, and M.S. Ferreira. A computationally efficient method for calculating the maximum conductance of disordered networks: Application to 1-dimensional conductors. *Journal of Applied Physics*, **108**, 103720, 2010.

- **Luiz F.C. Pereira** and M.S. Ferreira, Electronic transport on carbon nanotube networks: a multiscale computational approach. *Nano Communication Networks*, (to appear) 2011.

- P.N. Nirmalraj, **Luiz F.C. Pereira**, M.S. Ferreira, J.N. Coleman and J.J. Boland. Local electrical activation in silver nanowire films, (in preparation) 2011.

List of Figures

Chapter 1

Introduction

1.1 A Brief History of Carbon Nanostructures

The research on carbon fibres began in the 19^{th} century stimulated by the need for materials with special properties. After World War II, on the primordial days of jet-planes and space exploration, the need for strong, stiff, and lightweight composite materials with superior mechanical and elastic properties was responsible for a revolution on carbon fibres research. Carbon fibres are the predecessors and macroscopic analogues of microscopic carbon nanostructures, such as fullerenes, nanotubes and graphene.

With the discovery of fullerenes by Kroto et al. [1] in 1985[1], the study of carbon filaments of very small diameters ($\sim$ 1 nm) became more systematic, and attracted the attention of several research groups worldwide. A new era in carbon research began with the first reported experimental observation of carbon nanotubes, performed by Sumio Iijima [2] in 1991, using transmission electron microscopy (TEM). In the following year Saito et al. [3] calculated the band structure for single-walled nanotubes using a tight binding method based on the zone folding of graphene's band structure. Their calculations showed that some of those nanotubes could be

[1]R. F. Curl, Sir H.W. Kroto and R. E. Smalley were awarded the Nobel Prize in Chemistry 1996 "for their discovery of fullerenes".

metallic, which was confirmed experimentally [4] a few years later. The carbon nanostructure revolution continued when Geim and Novoselov [5] reported the isolation of free standing graphene flakes in 2004[2]. Isolated graphene sheets were, until then, regarded as being structurally unstable.

It did not take long for the scientific community around the world to realise that carbon nanostructures, due to their remarkable physical properties, present promising applicability in a range of areas. High performance, ultra-small electronic devices; drug delivery systems for disease treatment; and bullet proof vests are just three examples in a plethora of possible applications. Since their inception, the study of carbon nanostructures has only increased, and has arguably become one of the most active topics of scientific research today [6, 7, 8, 9, 10].

1.2 Carbon Nanotubes

Carbon nanotubes can generally be divided in two broad categories. Multi-walled nanotubes (MWNT) can be roughly described as a series of graphene sheets rolled in the form of concentric cylinders. The first observation reported by Iijima [2] included only nanotubes of this type. MWNTs can have diameters from 2 to 100 nm and lengths extending up to a micrometer. Single-walled nanotubes (SWNT) are formed by a single cylindrically rolled sheet of graphene, with a typical diameter of 1 nm. SWNTs were successfully observed in isolation shortly after their multi-walled counterparts [11, 12].

1.2.1 Geometry of Carbon Nanotubes

The structure of carbon nanotubes can be described in terms of the atomic arrangement present in a graphene sheet. Graphene is an infinite plane of carbon atoms arranged in a honeycomb lattice. Graphite is formed by several sheets of

[2] A. K. Geim and K. S. Novoselov were awarded the Nobel Prize in Physics 2010 "for groundbreaking experiments regarding the two-dimensional material graphene".

graphene stacked on top of each other. Adjacent graphene layers interact with each other through weak van der Waals forces, and are only loosely bound. The same van der Waals forces, however, are responsible for holding carbon nanotubes together in the form of bundles.

Carbon is possibly the most versatile of the chemical elements, for it can form pure structures in 0D (fullerenes), 1D (nanotubes), 2D (graphene), and 3D (diamond and graphite). This versatility of carbon is due to the many ways in which its four valence electrons can combine to form chemical bonds. In the case of graphene and graphite, three of the valence electrons will combine to form σ-bonds in the form of in-plane sp^2 hybridised orbitals. These are very strong covalent bonds, and are responsible for the mechanical strength of the derived carbon structures. The remaining valence electron occupies a π-bonded orbital, which is oriented perpendicular to the plane of graphene. In graphite, the interaction between adjacent planes is due to these π-bonds, which are usually weaker than σ-bonds. The small strength of these inter-plane π-bonds is one of the factors responsible for the lubricating properties of graphite. It is also possible for the valence electrons of carbon atoms to form sp^3 hybridised bonds. The strong sp^3 bonds, as well as the three-dimensional lattice structure, are directly responsible for the mechanical strength of diamond.

Figure 1.1 presents the honeycomb arrangement of atoms on the graphene lattice. The structure can be viewed as a triangular lattice with two carbon atoms per unit cell. This lattice is usually defined by the primitive vectors $\mathbf{a}_1$ and $\mathbf{a}_2$ shown. The graphene lattice parameter a, is defined in terms of the distance between two adjacent carbon atoms as $a = |\mathbf{a}_1| = |\mathbf{a}_2| = a_{C-C}\sqrt{3} = 2.46$ Å, where the distance between carbon atoms is $a_{C-C} = 1.44$ Å.

On figure 1.1 it is also illustrated how a graphene sheet can be rolled-up to form a nanotube by connecting equivalent atoms located at points O and A, and B and B', respectively. A nanotube is uniquely defined by its *chiral vector* $\mathbf{C}_h$,

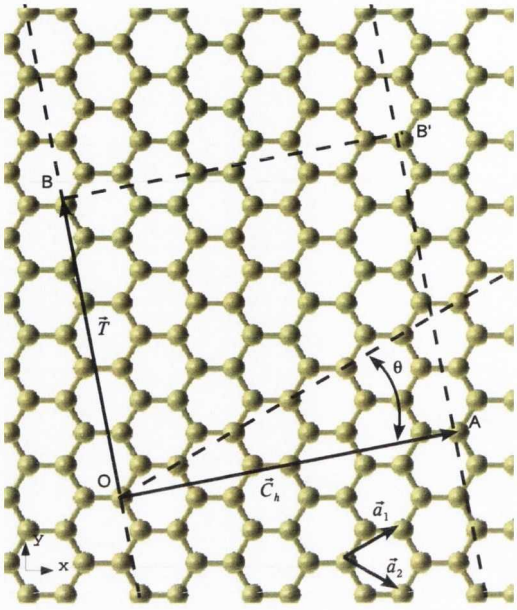

Figure 1.1: Schematic representation of a sheet of graphene. A nanotube structure is formed by rolling up the sheet to connect points O to A, and B to B', respectively.

given by

$$\mathbf{C}_h = n\mathbf{a}_1 + m\mathbf{a}_2 = (n, m), \tag{1.1}$$

where n and m are integer numbers, and are the so-called chiral indices of the nanotube. The vector $\mathbf{T}$ is the translational vector of the nanotube, and it is perpendicular to $\mathbf{C}_h$, and parallel to the nanotube axis. The unit cell of the nanotube is represented by the area enclosed in the rectangle $OBB'A$. The chiral angle θ is defined as the angle between $\mathbf{C}_h$ and $\mathbf{a}_1$, and can assume values in the range $0° \leq |\theta| \leq 30°$, which specifies the spiral symmetry of the nanotube.

Carbon nanotubes can be classified in two broad categories according to their symmetry: achiral and chiral. A nanotube is said to be achiral if it possesses inversion symmetry, and chiral otherwise. Achiral nanotubes can be further divided in two types with respect to their chiral indices: if $n = m$ it is said to be an *armchair* tube; if $n \neq 0$ and $m = 0$ it is a *zigzag* tube. Figure 1.2 displays the three possible geometric structures described. In the case of (n, n) armchair

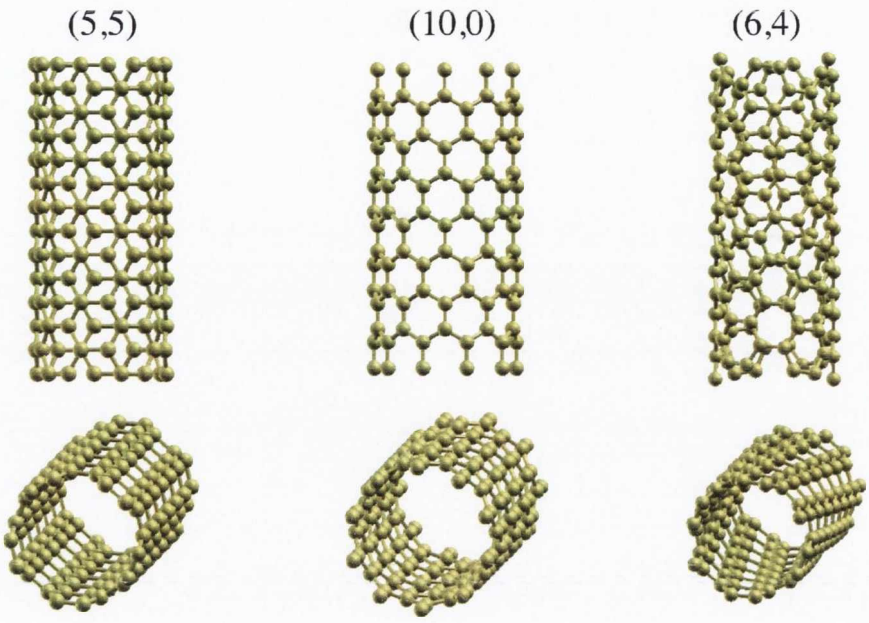

Figure 1.2: Geometric structure of three different carbon nanotubes. (5,5) is an armchair, (10,0) a zigzag, and (6,4) a chiral nanotube.

nanotubes, the unit cell is a single ring with $4n$ carbon atoms around the tube circumference. Meanwhile, in a $(n, 0)$ zigzag nanotube the unit cell is defined by two adjacent rings, each with $2n$ carbon atoms, resulting in a total of $4n$ atoms on the unit cell. Because of their spiralling structure, chiral nanotubes do not display inversion symmetry, and their unit cell is typically much larger than the ones for achiral nanotubes. Finally, the diameter of a generic (n, m) nanotube is given by

$$D = \frac{|\mathbf{C}_h|}{\pi} = \frac{2\pi r}{\pi} = \frac{a}{\pi}\sqrt{n^2 + m^2 + nm}. \tag{1.2}$$

In the next section some of the superior physical qualities of carbon nanotubes will be introduced. These remarkable electronic, thermal and mechanical properties are directly related to the geometrical structure of nanotubes, which have just been described.

1.2.2 Physical Properties

Research on carbon nanotubes is primarily instigated by their outstanding electronic, thermal, and mechanical properties. Even though real-world nanotubes are seldom defect-free, it has been shown theoretically and experimentally that even defected structures present exceptional intrinsic properties. The amount of defects in a nanotube is essentially determined by the synthesis process, the most traditional ones being laser ablation, arc-discharge and chemical vapour deposition (CVD). Currently, CVD growth is the most widespread fabrication technique and the most promising to provide industrial-scale deposition. Some of the advantages of CVD over other methods are its lower cost, and the capability of growing nanotubes directly on a desired substrate.

The work presented in this thesis is exclusively focused on the electronic properties of carbon nanotubes and network films. In the following subsections we introduce the electronic properties of nanotubes, followed by a very brief description of other physical properties, concluding with a brief discussion on nanotube–polymer composites.

Electronic Properties

The imposition of boundary conditions along the circumferential direction defined by the chiral vector $\mathbf{C}_h$ quantises the component of the electronic momentum in this direction. Meanwhile the momentum component along the tube axis remains continuous for a nanotube of infinite length. In essence, the energy bands of a nanotube are a set of one-dimension energy dispersion relations which are obtained by slicing up the 2D band structure of graphene. In the graphene lattice, σ and π electronic orbitals are decoupled by symmetry, leading to a convenient simplification. The σ energy bands are located far from the Fermi energy, whereas the π bands are close to the Fermi energy.

The electronic properties of carbon nanotubes are very sensitive to the wrapping

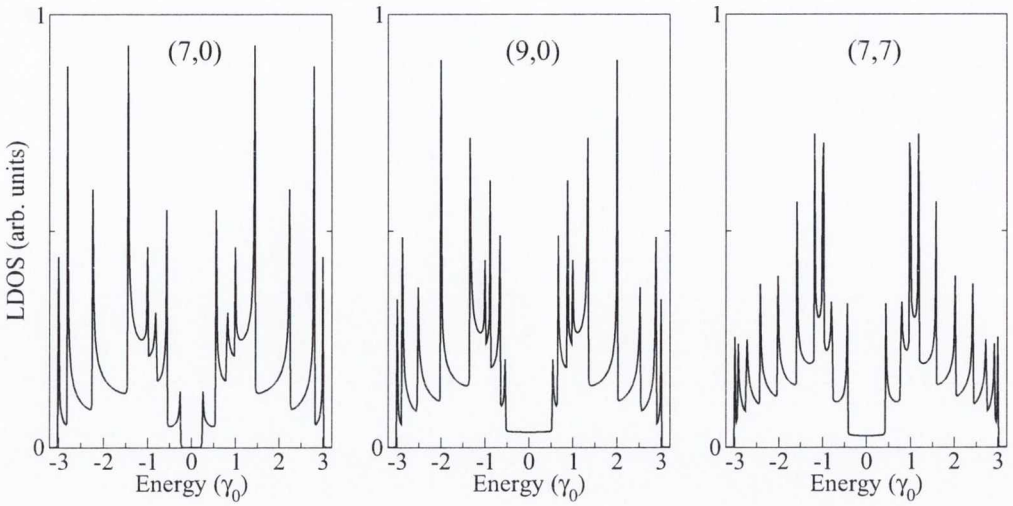

Figure 1.3: Calculated local density of states of a $(7,0)$ semiconducting zigzag carbon nanotube; a $(9,0)$ metallic zigzag nanotube; and a $(7,7)$ armchair nanotube. The spikes are van-Hove singularities, a characteristic signature of $1D$ systems. Energy in units of γ_0, defined as the electronic hopping parameter in chapter 2.

direction, and are essentially determined by the nanotube chiral indices (n, m). This sensitivity is a direct consequence of the momentum quantisation. If the situation is such that the Fermi surface of graphene is intersected by quantisation lines then the respective nanotube is metallic. In general, single-walled nanotubes are metallic if $n = m$; semiconducting with a very small energy band gap if $(n-m)$ $mod\ 3 = 0$; and semiconducting with a gap that depends on the diameter of the nanotube otherwise [3]. All armchair nanotubes $(n = m)$ are metallic, whereas some zigzag nanotubes behave as metallic and others as semiconductors. About 2/3 of SWNTs are semiconductors and 1/3 are metallic.

Figure 1.3 shows the calculated density of states (DOS) of one armchair and two zigzag nanotubes. The DOS were obtained with the Green function methods introduced in chapter 2. As expected for 1-dimensional systems, pronounced van-Hove singularities are present in the form of spikes in the local density of states. At the centre of the band, it is possible to observe a plateau, whose width decreases with the diameter of the nanotube. It has been confirmed experimentally that the number of states in the plateau is inversely proportional to the diameter of the

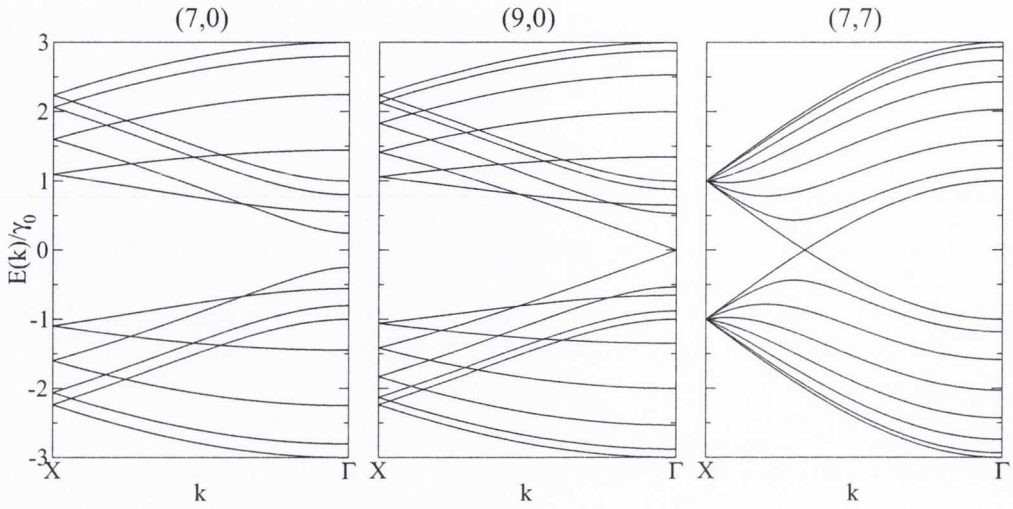

Figure 1.4: Band structure of carbon nanotubes. The $(7,0)$ zigzag nanotube shows a clear energy band gap, while $(9,0)$ is a zero gap semiconductor. The metallic structure of $(7,7)$ has two energy bands crossing the Fermi energy at $E(k) = 0.0\gamma_0$, where γ_0 is defined in chapter 2 as the tight binding hopping parameter. See also figure 2.3.

nanotube [4].

The calculated π band structure of armchair and zigzag nanotubes is shown in figure 1.4. The electronic structure is calculated from the tight binding model Hamiltonian and γ_0 is the electronic hopping parameter, as described in chapter 2. The zigzag $(7,0)$ nanotube, shows a clear energy band gap. If at least one energy band crosses the Fermi energy the system is metallic, as it is shown for the $(7,7)$ nanotube. Observe the particular case of the $(9,0)$ zigzag nanotube, which is a zero-band gap semiconducting system.

Carbon nanotubes are extremely conductive. Because of their 1-dimensional nature, electronic transport along nanotubes is essentially ballistic [13]. The absence of decoherent scattering causes their electrical resistivity to be very low, and allows nanotubes to carry very high currents. Because of this ballistic transport behaviour, it is expected that the resistance in a nanotube-based electronic device should come primarily from contacts with electrodes and possibly other nanotubes. Figure 1.5 shows the conductance of nanotubes as a function of the electronic energy, calculated with the Kubo formula to be introduced in chapter

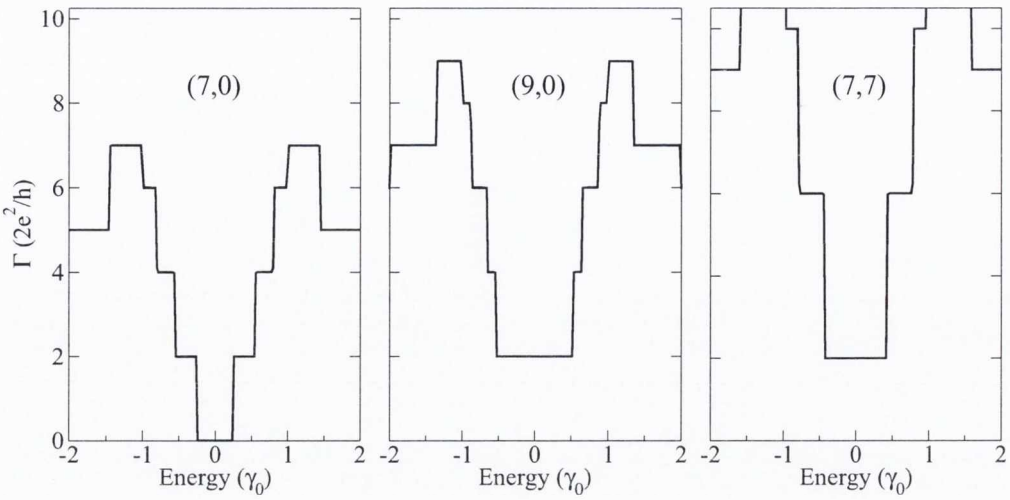

Figure 1.5: Conductance spectrum of carbon nanotubes. Metallic tubes have two conductance channels at the Fermi energy $E_F = 0.0\gamma_0$, where γ_0 is the electronic hopping parameter defined in chapter 2. See also figure 2.6.

2. The number of bands available at a specific energy equals the total number of conducting channels at that energy. Each conductance channel accounts for one quantum of conductance, defined as $\Gamma_0 = 2e^2/h$. In the case of metallic nanotubes there are two bands crossing the Fermi level at $E = 0.0\gamma_0$, and so the conductance along the tube equals $2\Gamma_0$ at the Fermi energy.

External factors such as the presence of an electrostatic gate or specific dopants can alter the conductance of nanotube in a controlled fashion. By exploring this property, proof-of-concept devices based on SWNTs have been demonstrated experimentally. Chemical sensors [7, 14] and field effect transistors [15, 16, 17] are among the different nanotube-based devices that explore these unique electronic transport properties.

Thermal Properties

Carbon-based materials present excellent thermal conductivity properties. This is mainly due to the strength of sp^2 and sp^3 bonds carbon atoms can form. In fact, it has been known for a number of years that graphite and diamond are excellent heat conductors.

Carbon nanotubes are also expected to be very conductive for phonons and to show a high thermal conductivity because of its sp^2 bonds. Theoretical calculations predict a thermal conductivity as high as 6600W/mK for isolated SWNT at room temperature [18]. Meanwhile, experiments have measured thermal conductivities in excess of 2000 W/mK for SWNT [19] and 3000 W/mK for MWNT [20]. These values are comparable to the thermal conductivity of diamond, which is one of the best heat conductors available. The superior thermal conductivity of nanotubes has led to the proposal of using them in connectors between high temperature devices and heat sinks.

Mechanical Properties

Carbon nanotubes are believed to be the strongest and stiffest materials known to date, in terms of tensile strength (the stress at which a material breaks or becomes permanently deformed) and elastic modulus (or Young's modulus, defined as the ratio of stress to strain in the elastic deformation regime). This impressive strength is, again, a result of the covalent sp^2 bonds present between carbon atoms in these structures. Under excessive tensile strain, nanotubes will undergo plastic deformation, becoming permanently deformed, before breaking. Under compression nanotubes are not so strong, and because of their hollow structure and high aspect ratio (length/diameter), will undergo buckling or kinking under compressive or bending stress, possibly returning to its initial form (without deformation) once the stress is released [21]. Theoretical and experimental techniques have been used to investigate the effects of mechanical deformation on the electronic structure of CNTs [22, 23]. It was found that, in general, mechanical deformations affect the electronic structure of CNTs such that there is an increase in the electrical resistance of along the nanotubes.

It is generally believed that even though a macroscopic structure made of CNTs will not be as resilient to compression as individual nanotubes, the larger structures

will nonetheless retain some of the restoration properties. It should be no surprise that several studies have been performed to analyse and enhance the reinforcement of materials through introduction of carbon nanotubes, as it is presented next.

1.2.3 Composites

As previously described, carbon nanotubes possess superior physical qualities. Some of these properties could be utilised to improve the performance of other materials, by integrating nanotubes with them, in order to form composite structures. The collective behaviour of nanostructures can provide unique physical properties and enhanced device performance. One of the major advantages of the integration of nanoscale materials is the statistical averaging, which provides better reproducibility over a range of different samples.

In fact, a particularly promising type of integration are nanotube-polymer composites. A polymer is a macromolecule, formed by covalently bonded elementary units (monomers) forming a chain, which gets tangled due to interactions between different monomers. Experimental studies have shown that polymers readily form composites with carbon nanotubes [24], and typically just a few percent by volume of nanotubes is added to a polymer matrix with the objective of enhancing its physical properties. For example, the addition of a small quantity of nanotubes can increase the conductivity of ordinary polymers, known as poor electrical conductors, and form a conductive nanotube-polymer composite [25, 26]. Another example is the mechanical reinforcement of polymers by addition of carbon nanotubes. It has been shown that the addition of small quantities of nanotubes by volume to a polymer can greatly improve the mechanical properties of the composite material [27, 28, 29, 30]. It is important to work only with small quantities of nanotubes on the composite materials, so that the useful properties of the polymer are not destroyed. The extensive knowledge on polymer composites provides a huge advantage to this line of research, and the development of nanotube–polymer

composites with superior physical qualities led to the development of materials based solely on carbon nanotubes.

1.3 Carbon Nanotube Network Films

Films made solely of carbon nanotubes can be produced by chemical processing or directly grown on a substrate. In these films, individual nanotubes and bundles are randomly distributed forming a complex interconnected network. *Carbon nanotube network films* (also *CNT films* or *CNT networks*) can be regarded as a novel wonder material whose general physical qualities are defined by the collective behaviour of the ensemble of nanotubes in the film. Figure 1.6 shows a typical nanotube network film produced by deposition of commercially available SWNTs. The scanning electron micrographs have different resolution, as indicated in the figure. In general, individual nanotubes and bundles will tend to align in layers parallel to the surface of the substrate with an arbitrary orientation. However, because of the flexibility of nanotubes, many of these layers are interpenetrating. The thickness of the films can be controlled during fabrication and films become more isotropic as their thickness increases. It is also possible to control the longitudinal orientation of the nanotubes during the fabrication of the films [31, 32, 33, 34, 35, 36], although this is only advantageous to some of the possible applications. Carbon nanotube films present remarkable promise on the construction of flexible electronic devices such as transistors [34, 37, 38, 39], organic light emitting diodes [40, 41], and transparent electrodes [42]. Electronic transport across such films takes place through tunnelling between individual nanotubes, and their overall resistance is controlled by the quality of the inter-tube junctions throughout the network [31, 42].

Network films are made of a mixture of metallic and semiconducting nanotubes, and show a semiconductor–metal transition as the films thickness is increased. The range of possible application of the films depends on their thickness. For example,

(a) 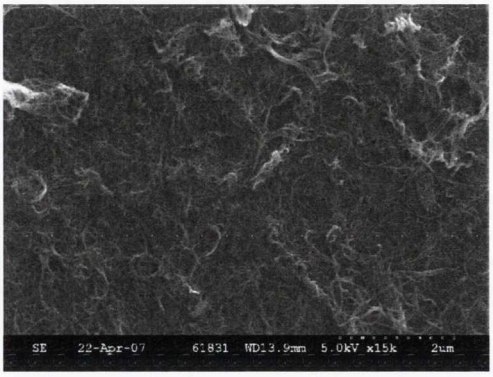

(b) 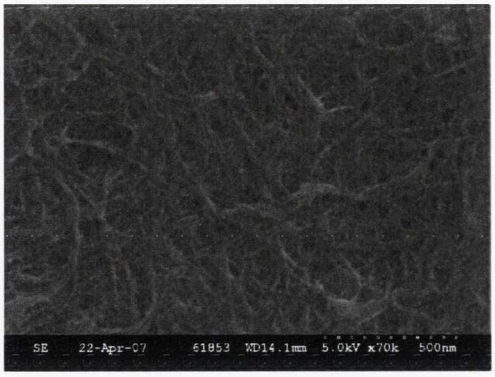

Figure 1.6: Scanning electron micrographs of a typical nanotube network film. The network was produced by deposition of commercially available nanotubes. The resolution in (b) is higher than in (a), as indicated in the scale bars. Images courtesy of Prof. Coleman's research group, Trinity College Dublin.

thin films with density close to the percolation threshold behave as semiconductors and can be used in thin film transistors [34, 35, 36, 37, 38, 39, 43]. Films with thickness in the range of $10 - 100$ nm show high optical transparency and electrical conductivity and can be used as a replacement for indium-tin-oxide (ITO) electrodes [40, 41, 44, 45, 46, 47, 48]. The geometric model introduced in chapter 3 is particularly focused on this thickness range, and as it will be shown is capable of accounting for the network structure found in this situation. Finally, CNT films about a micron thick are nanoporous and can be used as electrodes for supercapacitors [49], fuel cells [50], and battery applications [51].

Fabrication of Nanotube Films

Carbon nanotube network films can be produced by a variety of different methods. Similar to individual CNTs, network films can be directly grown by CVD. This technique can produce networks with aligned nanotubes as well as randomly oriented ones. In practice, networks with random orientations of CNTs are preferred for reproducibility and applications [37], but other techniques have also been developed to produce aligned arrays of nanotubes [31, 33, 34]. CVD can be used to provide macroscopic quantities of CNTs, and it produces films with individually

separated nanotubes, with few defects and good inter-tube contacts. Major disadvantages of the CVD method include the requirement of high vacuum and high temperatures.

Solution-based deposition methods are currently a popular alternative to direct growth techniques. A solution-based process can be carried out at room temperature; does not require high vacuum, is compatible with plastic substrates, and can be done at high speeds. Overall, solution-based deposition has a lower cost when compared to CVD. In a solution-based method, nanotubes first have to be dispersed in a solvent which will promote separation of the bundles [52, 53]. The resulting solution is then filtered or deposited on a substrate, and the system is let to dry in a controlled fashion. Another popular solution-based method is by inkjet printing. In this case the film is printed directly on the substrate and networks with very uniform density can be produced [54].

Mechanical Properties

The superior mechanical properties of individual carbon nanotubes are also present in films made of disordered CNT networks. Nanotube films show unprecedented mechanical flexibility, an extremely useful property for the fabrication of flexible electronic displays. In particular, nanotube films are being heavily explored as a possible replacement to the expensive ITO in electronic displays [48, 55]. ITO is brittle, and films based on this material experience large increase in electrical resistance after being bent a few times. CNT films retain their structure and electronic transport properties after several cycles of bending down to a very small radius [38, 39, 56]. For that reason, large sums are being invested to find a suitable replacement for ITO, and nanotube films appear as a strong contender.

Electronic Transport Properties

The first studies on the electronic properties of carbon nanotube films were reported a few years after Iijima's original observation of individual CNTs [2]. In one of these pioneering studies, de Heer et al. produced CNT films approximately 1 μm thick, in which nanotubes were aligned parallel or perpendicular to the substrate [31]. In the case of parallel alignment, de Heer et al. observed a strong anisotropy in the measured electrical resistance, such that it was much larger on the direction perpendicular to the nanotube alignment than on the longitudinal direction. The films produced in this study where small, such that the length of the film was comparable to the length of the bundles. Therefore, in the longitudinal direction the electronic transport took place along individual CNTs and bundles, with little inter-tube hopping. On the other hand, when the transport took place along the direction perpendicular to the nanotube alignment, the electrons had to tunnel through several CNT junctions before reaching the opposite electrode, considerably increasing the electrical resistance measured. Similar results were reported more than a decade later by Pint et al. [57], where much thinner films were considered.

The effect of temperature on the electronic transport properties of carbon nanotube films has also been investigated by experimental groups. The dependence of the film resistivity with the temperature was first reported by de Heer et al. [31] and Omel'Yanovskii et al. [58], which have shown how the film resistivity decreases as the temperature is increased. The decrease in resistivity with temperature, a typically nonmetallic behaviour, has been explained in terms of temperature induced hopping, in accordance with the variable-range hopping theory of Mott [59]. Similar results for thinner films were also reported by Pint et al. [57].

A pioneering work on the application of nanotube films as thin-film transistors was reported by Snow et al. in 2003 [37]. In this work, networks with randomly oriented CNTs were placed between metallic source and drain electrodes and the resistance of the devices was measured as a function of the channel length. The

authors found that the device resistance shows a power law dependence on the channel length, and that the respective exponent depends on the density of the network. Through current–voltage measurements Snow et al. have shown that high on–off current ratios could be obtained for devices with low network densities. Devices fabricated with high density networks show a low on–off current ratio, due to the presence of charge carrying paths formed by metallic CNTs. In this case, the authors argued that a method proposed by Collins et al. [60] could be used burn the parasitic metallic paths by the application of a high bias voltage through the network. Shortly after, Bradley et al. reported on the production of flexible nanotube network transistors [38], in which a film with randomly distributed CNTs was deposited over a polymer substrate. In this work the authors demonstrated the production of flexible field-effect transistors with high on–off current ratios, and whose performance was not heavily affected by bending of the device, as confirmed by current–voltage measurements. In a further development, Takenobu et al. demonstrated the fabrication of transparent and flexible CNT network transistors, whose high-performance was also not affected by bending of the film [39]. The authors presented data clearly indicates that their devices are capable of operating on a high on–off current ratio while bent down to very small radii.

In 2005, Kumar et al. presented the first computational study of nanotube network transistors, capable of reproducing some of the experimental results reported in the literature [61]. Through the investigation of percolating 2D random networks of sticks with a given length and diameter, Kumar et al. developed a computational framework capable of reproducing some of the measurements presented by Snow et al. [37] for devices with long channel length. Furthermore, the work of Kumar et al. also presents an analytical treatment for devices with short channel length, in a ballistic or diffusive transport regime. Finally, this work provided the first clear evidence that the electronic transport properties of nanotube networks

could be understood in terms of finite-sized rigid-rods percolation and inter-tube coupling strength. Further developments of the theory, which include networks with a mixture of metallic and semiconducting carbon nanotubes, were presented by Kumar et al. in 2006 [62]. A follow-up work by Pimparkar et al. presented an alternative analytical theory to explain the current–voltage characteristics of CNT network transistors where the networks are below the percolation limit [63]. The theory developed by Pimparkar et al. presents an excellent agreement with measurements of on- and off-current as a function of the device channel length, as well as an estimation of the voltage bias pulse required to burn metallic nanotubes [60] in terms of the transistor device parameters. Topinka et al. have presented results of experiments and computer simulations on networks with varying fraction of metallic tubes [64]. In this work, the authors argue how it is possible to calculate the optimum ratio between metallic and semiconducting tubes in order to maximise the on–off ratio of CNT network transistors.

Experimental and theoretical studies reported by Kobacas et al. [35], and computer simulations reported by Behnam et al. [65] and White et al. [66] have investigated the effect of nanotube alignment on the performance of CNT thin films. These studies show that when the film is much longer the length of individual nanotubes, films with perfectly aligned CNTs have a larger measured electrical resistance than a film in which nanotubes are allowed to form a small angle with the longitudinal direction of the film. This result is not surprising, and can be easily understood by taking into consideration that the average number of neighbours per tube is smaller in the aligned films than in a film with randomly oriented CNTs. Consequently, there are fewer current carrying paths on aligned carbon nanotube films than on films with a small degree of misalignment.

On a very recent work reported by Jack et al. [67], computational modelling and experiments have been performed to study electrical conductivity in densely packed carbon nanotube networks. An almost comprehensive stochastic model has been

developed to reproduce distributions in length, diameter, orientation, and contact resistance found in real nanotube networks films. The authors apply their model to calculate the dependence of the film conductivity with average nanotube length and diameter and find results in excellent agreement with experimental results. Furthermore, the model also reproduces qualitative features on the effect of a magnetic field on the conductivity of CNT films. Jack et al. also compare results obtained with the stochastic model, where nanotube length and diameter follow a given distribution, to results obtained in corresponding simulations where all the nanotubes in the film are identical (same length an diameter). The calculated conductivity in the presence of a magnetic field differs by less than 10% between the stochastic model and the simpler model, which clearly indicates that having a realistic distribution of length and diameter is not of such importance for CNT networks simulations.

All of the results discussed above show that nanotube network films present electronic transport properties which are a combination of individual nanotube transport and tunnelling at inter-tube junctions. Transport on single nanotube devices can be heavily affected by the quality of the contacts with metallic electrodes, and contact resistance depends considerably on the metal in the electrode [68]. Ti, Pd, Pt, Cu, Au, and Ag are some of the metals that provide low contact resistances with CNTs. In the case of CNT films, the contact resistance with metallic electrodes is still under investigation [69, 70, 71].

CNT films contain a mixture of metallic and semiconducting species, and the electronic transport process can be extremely complex. However, because of CNTs remarkable ballistic conductance, the contact resistance between individual tubes is the single largest contribution to the resistance of network films [31, 42]. The junction resistance depends heavily on the type of nanotubes involved as well as their diameter [72, 73, 74, 75, 76].

Since the inter-tube resistance is much larger than the intrinsic nanotube resis-

tance, electrons will tend to travel as far as possible along the tube before hopping onto one of its neighbours. In the case of bundles, the electrons tend to propagate along the external tubes. The transport properties of CNT films depend on the average length and diameter of nanotubes and bundles in the film [37, 46, 67]. Networks with a higher density of nanotubes present more current carrying paths and the overall resistance of the films is also very sensitive to this factor [61, 63]. Finally, because of the high aspect ratio of CNTs, networks of carbon nanotubes have very low percolation thresholds. Even for modest surface coverage, nanotubes can form several conducting paths across the film. Percolation issues are very important for the application of CNT networks as transparent, flexible transistors [37, 61, 77, 78, 79]. In general, solution-based methods can be used to control the nanotube density in network films [77].

1.4 Optoelectronics: CNT Networks as Transparent Electrodes

One of the very the first investigations into the optoelectronic properties of random nanotube networks, with the objective of producing transparent electrodes was reported by Wu et al. [80]. In this work, the authors describe the production of thin, transparent and conductive carbon nanotube films and the transfer of these films to different substrates. The films were produced by filtration of a solution containing suspended nanotubes, and the film thickness was controlled by the nanotube concentration and the volume of solution filtered. The films produced present an optical transmittance comparable to ITO in the visible spectrum, being as high as 70% with a sheet resistance of about 30Ω. An an example application, Wu et al. used the CNT films to construct an electric field-activated optical modulator, which constitutes an optical analog of the nanotube network field-effect transistor. In 2006, Aguirre et al. reported on the production of organic light-emitting diodes

based on transparent carbon nanotube films [41]. The films were produced following the method described by Wu et al. [80] and consisted of networks made of randomly oriented CNTs. The organic light-emitting diodes produced by Aguirre et al. show a performance comparable to standard devices based on ITO, with the additional advantages of being flexible and easier to process.

The transparency of a thin film is intimately connected to its conductance. In particular, the relationship between optical transmittance T and sheet resistance R_s of a thin metallic film (suspended in air) is approximately described by [81]

$$T = \left[1 + \frac{188.5(\Omega)}{R_s}\frac{\sigma_{op}}{\sigma_{dc}}\right]^{-2}, \tag{1.3}$$

where σ_{op} is the optical conductivity of the film, and σ_{dc} its electrical conductivity. Equation (1.3) is only valid when the absorption of the material is much smaller than its reflectance, and when the film thickness is much less than the wavelength of interest. In general, CNT network films can be prepared to satisfy these conditions.

For applications in transparent electrodes a material is required to have high electrical conductivity and low optical absorbance [40]. Flexible displays require high transparency in the visible spectrum coupled with low film resistance [82]. Minimum industry standards (based on knowledge from ITO-based devices) require materials with sheet resistance $R_s \leq 100\Omega$, and optical transmittance $T \geq 90\%$, at a wavelength of 550 nm [56]. From equation (1.3), it is possible to evaluate that this condition may be satisfied if the electrical conductivity is much larger than the optical conductivity, such that the ratio σ_{dc}/σ_{op} is large. In particular, industrial requirements can be satisfied only if $\sigma_{dc}/\sigma_{op} \geq 35$. Along the development of CNT film fabrication, this ratio has been improved, but the best results reported for nanotube films so far have only achieved $\sigma_{dc}/\sigma_{op} = 13 - 16$ [56, 76, 83].

The optical conductivity depends on the chirality of individual nanotubes, and cannot be precisely controlled on CNT films. However, due to the mixture of

different types of nanotubes in a network film, σ_{op} is found to be approximately constant across a variety of nanotube films [84], and has been measured as 1.7×10^4 S/m [56, 85]. On the other hand, the electrical conductivity σ_{dc}, depends on a number of factors, including the degree of purity of the nanotubes; the doping level; the average bundle length; and the average bundle diameter. A number of strategies have been developed to control these factors. Attempting to increase σ_{dc} by lowering the tube-tube junction resistance seems to be the most accessible way of improving the performance of conductive films [76, 83, 86].

The lowest acceptable value of electrical conductivity to meet industry standards can be calculated at $\sigma_{dc} = 6 \times 10^5$ S/m. This level of conductivity has been achieved before, but for dense thick films which do not satisfy the transparency requirements [80]. Much work has been done on possible ways to improve σ_{dc} without compromising the film transparency. As things stand today, the best reported results for carbon nanotube networks is $\sigma_{dc} = 6 \times 10^5$ S/m with $T = 76\%$ [76], and it is still unclear if the required combination of R_s and T is indeed feasible [48, 55]. In fact, this is one of the major issues addressed in the present work, and we show that the limiting conductivity for carbon nanotube films is $\sigma_{dc} = 9 \times 10^6$ S/m, which corresponds to a transmittance as high as 99% at a sheet resistance $R_s = 90\Omega$, through equation (1.3). Even though these results do not exclude nanotube network films as a possible replacement for ITO transparent electrodes, it shows that the best available experimental results are already very close to the theoretical upper limit, and that other materials might be better suited to this particular application.

1.5 Layout of Thesis

The work presented in this thesis is focused on the investigation of electronic transport on disordered carbon nanotube networks. A multiscale modelling approach

has been developed in order to describe network films from their morphological characteristics and down to the quantum tunnelling taking place at nanotube junctions. Even though major focus has been given to carbon nanotube films, the methodology developed can be easily generalised to network films of other materials such as metallic nanowires and perhaps graphene flakes. All the theoretical techniques applied throughout this work are aimed at describing the systems in the most transparent and lightweight manner, but ensuring that a complete physical picture of all relevant matters is correctly described.

This thesis comprises six chapters. In chapter 2 the general theoretical framework will be introduced. First, the single-band tight binding approximation will be presented. It will be shown that a π-band Hamiltonian is well suited to describe all relevant electronic properties of carbon nanotubes. Secondly, the single particle Green function methodology will be introduced. Green functions are calculated directly from the chosen Hamiltonian, and give direct access to the density of states of a physical system. Next, the Kubo formalism for electronic transport calculations will be introduced. It will be shown how the conductance of pure and doped structures is calculated from the Kubo formula written in terms of Green functions. The chapter concludes with a brief description of how the usual Kubo formalism can be applied to tripartite systems, composed of two leads and a central scattering region.

Chapter 3 is concerned with modelling the macroscopic properties of nanotube networks. A geometric description based on randomly distributed rods will be introduced as a model to CNT networks. The connectivity of disordered ensembles will be examined in terms of basic parameters such as the density of the networks and the aspect ratio of individual rods. Resistive networks will be introduced as a simple representation to nanotube films. Existing methods for calculating the equivalent resistance in regular networks will be reviewed, and a method suitable for resistance calculations in random structures will be introduced. The chapter

concludes with the application of the developed methodology to analyse random resistive networks of rods. Simulation results will be compared and combined with experiments, and the average junction resistance in a real CNT network film will be estimated.

In chapter 4 the focus is on microscopic modelling. The electronic structure methods of chapter 2 will be applied to provide an atomistic description of carbon nanotubes and idealised nanowires. It will be shown how the Green function of an ensemble of nanoscopic elements can be written in a convenient form. The Kubo formula for the conductance will be directly applied to networks, following a computationally efficient framework. In conjunction with the geometrical modelling of chapter 3, a multiscale computational model will be developed, which relates theoretical models to real network films. Considering a fully ballistic transport regime, the upper bound for the electrical conductivity of nanotube networks will be estimated. This is an important quantity that tells us how much room for improvement there is in enhancing the conductivity of nanotube network films. Furthermore, this result can be used to assess if nanotube network films are indeed the most suitable material for the production of flexible electronic displays.

Chapter 5 presents two extensions of the methodologies developed in chapters 3 and 4. In the first half of the fifth chapter, the application of nanowire films as a non-magnetic spacing between magnetic moments will be considered. Indirect exchange coupling is known to be mediated by conduction electrons of the non-magnetic spacing material. The nanowire network model developed in chapter 4 can be directly applied and the coupling will be calculated from specific Green functions elements of the network. In the second half of the chapter, a capacitive network model will be applied to investigate the onset of local electrical activation on silver nanowire films. Very recent experimental measurements show that certain regions of Ag nanowire films can be activated by the application of a voltage difference between an electrode and the tip of an atomic force microscope.

Experimental current–voltage curves show a hysteresis-like behaviour and it has been hypothesised that this is caused by impurities located at nanowire junctions. When the voltage applied is high enough, an electric field causes a breakdown of the impurity, much like a capacitor under high voltage bias. It will be shown how the resistive network model developed in chapter 3 can be effortlessly modified to investigate the local activation observed in silver nanowire networks. The results can be directly compared with existing experimental measurements, and utilised to understand the phenomenology involved.

The thesis concludes with chapter 6, which contains a summary of the main results presented in each chapter, along with a brief description of possible extensions to this work.

Chapter 2

General Theory

In this chapter we present a description of the general methodology applied throughout this work. The *Tight Binding model* is introduced and applied to describe the electronic structure of carbon nanotubes. This is a relatively simple model, which nonetheless is capable of capturing all the relevant features of the band structure of carbon nanotubes. In the sequence, the *Green function* formalism is introduced along with some basic properties and applications. Green functions are calculated directly from the Hamiltonian and are intrinsically related to the density of states of a physical system. The effect of a perturbation on the electronic structure of a physical system can be calculated with *Dyson's equation*. The Green function of the perturbed system is obtained directly from that of the unperturbed system, without the need to diagonalise a new Hamiltonian. The perturbation might for example be the introduction of an impurity on the material, or even an interaction with another system. Based on Dyson's equation it is possible to calculate the Green function of very large systems with the *recursive method*. Calculating the Green functions recursively, very large periodic and non-periodic systems can be tackled in a very efficient fashion. The *Kubo transport formalism* is introduced as our method of choice for electronic transport calculations. The Kubo formula provides a direct expression for the conductance of a system in terms of specific

Green function elements. Finally, we show how the Green functions of a tripartite system can be calculated, such that the Kubo formula can be directly applied to calculate the conductance in carbon nanotube networks.

2.1 Electronic Structure: Tight Binding Model

The tight binding (TB) model provides a relatively simple description of the electronic structure of a physical system. A solid is described as a lattice formed by independent atoms separated by the lattice constant. The electronic wavefunction is written as a combination of localised atomic orbitals, one for each atom in the system. The precision of the tight binding approximation for a specific material depends on the length of the independent wavefunctions relative to the lattice constant, more specifically, it depends on the overlap between the wavefunctions of neighbouring atoms. If the overlap is small enough the approximation can be quite accurate, providing results in good agreement with more complex electronic structure methods or experimental measurements. The tight binding approach can also serve as a basis for more complex electronic structure methods, which are naturally not so computationally inexpensive. The eigenfunctions of the solid can be written as a Linear Combination of Atomic Orbitals (LCAO), similar to the molecular orbital approach. Even though the method can be applied to non-crystalline solids, its most common application is in systems with translational symmetry, where the atomic orbitals satisfy Bloch's theorem.

For sp^2 hybridised carbon materials the TB approximation considering only π valence electrons provides very good results for general electronic properties. This is because three of the valence electrons form in-plane covalent bonds, while the π orbital is perpendicular to the plane, being therefore completely decoupled from the others. The covalent σ-bonds have energies far from the Fermi level, and the only relevant electronic states in this region are the π orbitals.

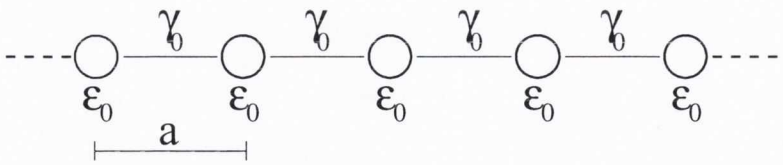

Figure 2.1: Schematic representation of an infinite linear chain. The distance between adjacent atoms is given by the lattice parameter a. The tight binding parameters are the on-site energy ϵ_0 and the nearest neighbour hopping integral γ_0.

In general, the tight binding method does not account for electron-electron interactions, but because of its simplicity and computational efficiency, allowed for great development on the study of materials (including carbon nanotubes) within its limits of application. Some systems do require the inclusion of more complex interactions, and thus should be treated by appropriate theoretical methods. High precision electronic structure methods are usually limited to periodic systems of sizes up to hundreds of atoms, and are therefore not suitable for a description of heavily disordered environments, such as the carbon nanotube networks considered in this work.

The following sections present some applications of the tight binding method, from the linear monatomic chain to graphene and carbon nanotubes. It will be shown how the TB approximation can be applied to calculate the band structure of graphene considering a single orbital tight binding Hamiltonian. In the sequence, it will be shown how to obtain the band structure of achiral nanotubes by imposing appropriate quantisation of the wave vector.

2.1.1 A Simple Application: The Linear Chain

The simplest system to which one can apply the tight binding electronic structure method is the infinite atomic chain. Figure 2.1 illustrates the atomic arrangement of a monatomic chain. In spite of its simplicity, the problem illustrates all the important features of the tight binding method and it is included here as a brief preparation to the application in graphene and carbon nanotubes.

Using Bloch's theorem we can write the electronic eigenfunctions as a linear combination of localised atomic orbitals in the form

$$|\psi_{\mathbf{k}}\rangle = \frac{1}{\sqrt{N}} \sum_{\mathbf{r}} e^{i\mathbf{k}\cdot\mathbf{r}} |\phi_{\mathbf{r}}\rangle, \tag{2.1}$$

where $\mathbf{k}$ is the wave vector, $\mathbf{r}$ specifies the atomic sites and $\frac{1}{\sqrt{N}}$ is a normalisation factor. Since we are dealing with a 1-dimensional system we can write $\mathbf{k} = k$. The electronic states of the system, can be found by solving the time-independent Schrödinger equation

$$\hat{H}|\psi_k\rangle = \varepsilon_k |\psi_k\rangle, \tag{2.2}$$

and the energy eigenvalues are calculated through a secular equation, written in the form

$$\det\left[\hat{H} - E\hat{S}\right] = 0, \tag{2.3}$$

where $\hat{S}$ is the overlap matrix, which represents the mixture between atomic orbitals in different sites. Assuming a fully orthogonal basis set, we can write $S_{k,k'} = \delta_{k,k'}$, where δ is the Kronecker delta, such that there is no overlap between orbitals in different atoms. The Hamiltonian matrix elements are given by $H_{k,k'} = \langle\psi_{k'}|\hat{H}|\psi_k\rangle$. In the tight binding approximation, each atom interacts only with its nearest neighbours, and the Hamiltonian can be written in terms of parameters defined as

$$\langle\psi_{k'}|\hat{H}|\psi_k\rangle = \begin{cases} \epsilon_0, & k' = k \\ \gamma_0, & k' = k \pm a \end{cases}.$$

where ϵ_0 is the on-site potential energy and γ_0 is the nearest neighbour hopping. In its essence, γ_0 is intimately related to the probability of an electron hopping from a given atom to one of its neighbours. The parameters of a specific tight binding Hamiltonian can be calculated by fitting the results to experimental measurements

or high precision ab-initio calculations at specific high symmetry points, as first introduced by Slater and Koster [87].

Solving the secular equation for the energy eigenvalues, we obtain the energy dispersion relation for the band structure of an infinite linear monatomic chain

$$\varepsilon_k = \epsilon_0 + 2\gamma_o \cos(ka). \tag{2.4}$$

This simple one band picture can be straightforwardly generalised to the case where the solid has more than one atom (or orbital) per unit cell. In the next sections we apply it for graphene and carbon nanotubes.

2.1.2 Band Structure of Graphene

The unit cell of graphene is made of two unequivalent carbon atoms (any two adjacent atoms in figure 1.1), thus two Bloch functions are needed to form its basis functions, which can be written as

$$|\psi_{\mathbf{k}}, \lambda\rangle = \frac{1}{\sqrt{N}} \sum_{\mathbf{r}} \sum_{s=1,2} e^{\imath \mathbf{k}\cdot\mathbf{r}} A_s^{\mathbf{k}} |\phi_{\mathbf{r}}, s\rangle, \tag{2.5}$$

where $\mathbf{r} = c_1\mathbf{a}_1 + c_2\mathbf{a}_2$ is the position of a unit cell, $|\phi_{\mathbf{r}}, s\rangle$ is the atomic orbital of atom s in the unit cell located at $\mathbf{r}$, and $\frac{1}{\sqrt{N}}$ is a normalisation factor.

Calculating the appropriate Hamiltonian matrix elements $H_{\mathbf{k},\mathbf{k}'}$ and the overlap matrix $S_{\mathbf{k},\mathbf{k}'}$, and using the secular equation we obtain the eigenvalues $\varepsilon_{\mathbf{k}}^{\lambda}$ of graphene. Adopting a zero overlap matrix, we obtain symmetric π and π^* bands, given by

$$\varepsilon_{\mathbf{k}}^{\pm} = \epsilon_0 \pm |\gamma_0| \sqrt{3 + 2\cos(\mathbf{k}\cdot\mathbf{a}_1) + 2\cos(\mathbf{k}\cdot\mathbf{a}_2) + 2\cos(\mathbf{k}\cdot(\mathbf{a}_1 - \mathbf{a}_2))}. \tag{2.6}$$

Expressing the lattice vectors explicitly as $\mathbf{a}_1 = a\mathbf{y}$ and $\mathbf{a}_2 = a\sqrt{3}/2\mathbf{x} + a/2\mathbf{y}$, and

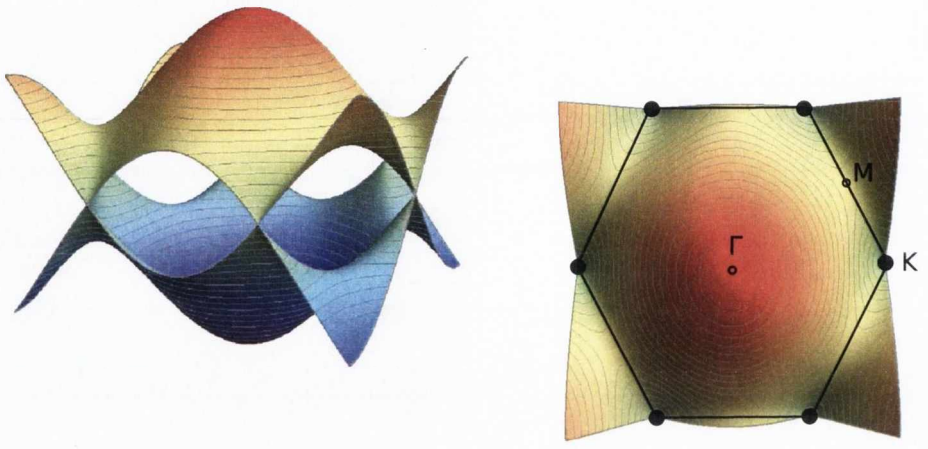

(a) (b)

Figure 2.2: (a)Tight binding band structure of graphene. (b)Representation of the Fermi surface of graphene, and three high symmetry points of its first Brillouin zone.

the wave vector as $\mathbf{k} = k_x\mathbf{x} + k_y\mathbf{y}$, we obtain

$$\varepsilon_{\mathbf{k}}^{\pm} = \epsilon_0 \pm |\gamma_0| \sqrt{1 + 4\cos(\frac{\sqrt{3}k_x a}{2})\cos(\frac{k_y a}{2}) + 4\cos^2(\frac{k_y a}{2})}. \tag{2.7}$$

In the case of graphene and carbon nanotubes, the nearest neighbour hopping integral has been calculated from first principle methods to be $\gamma_0 = 2.7$ eV [88].

Figure 2.2(a) illustrates the band structure of graphene, generated by plotting equation (2.7). Since we neglected all overlap terms beyond nearest neighbours, symmetric valence and conduction bands are obtained. In 2.2(b) we present an schematic illustration of the Fermi surface of graphene, composed of the six points in the hexagon shown. Also shown are three high-symmetry points of the first Brillouin zone of graphene, Γ, K and M.

2.1.3 Band Structure of Carbon Nanotubes

The band structure of a single wall carbon nanotube can be obtained from that of graphene by imposing the appropriate boundary conditions. The wave vector

associated with the $\mathbf{C}_h$ direction becomes quantised, while the wave vector in the direction of the translational vector remains continuous for a nanotube of infinite length. The quantisation of the wave vector is given by

$$\mathbf{C}_h \cdot \mathbf{k} = 2\pi q, \quad q \text{ integer.} \tag{2.8}$$

As a result the energy bands of a nanotube are a set of one-dimensional energy dispersion relations obtained by slicing up the 2D band structure of graphene in the circumferential direction.

For a (n, n) armchair nanotube the graphene sheet is rolled up along the $\mathbf{x}$ direction, and the allowed wave vectors along this direction are given by

$$k_{x,q} = \frac{2\pi}{a\sqrt{3}}\frac{q}{n} \quad (q = 1, ..., 2n), \tag{2.9}$$

and thus, the energy dispersion relation for an armchair nanotube is given by

$$\varepsilon_k^q = \epsilon_0 \pm |\gamma_0| \sqrt{1 \pm 4\cos(\frac{q\pi}{n})\cos(\frac{ka}{2}) + 4\cos^2(\frac{ka}{2})}, \tag{2.10}$$
$$(-\pi < ka < \pi), \quad (q = 1, ..., 2n).$$

Analogously, for a $(n, 0)$ zigzag nanotube the rolling up takes place along the $\mathbf{y}$ direction. The allowed wave vectors are

$$k_{y,q} = \frac{2\pi}{a}\frac{q}{n} \quad (q = 1, ..., 2n), \tag{2.11}$$

and the energy dispersion relation for a zigzag nanotube is

$$\varepsilon_k^q = \epsilon_0 \pm |\gamma_0| \sqrt{1 \pm 4\cos(\frac{\sqrt{3}ka}{2})\cos(\frac{q\pi}{n}) + 4\cos^2(\frac{q\pi}{n})}, \tag{2.12}$$
$$(-\frac{\pi}{\sqrt{3}} < ka < \frac{\pi}{\sqrt{3}}), \quad (q = 1, ..., 2n).$$

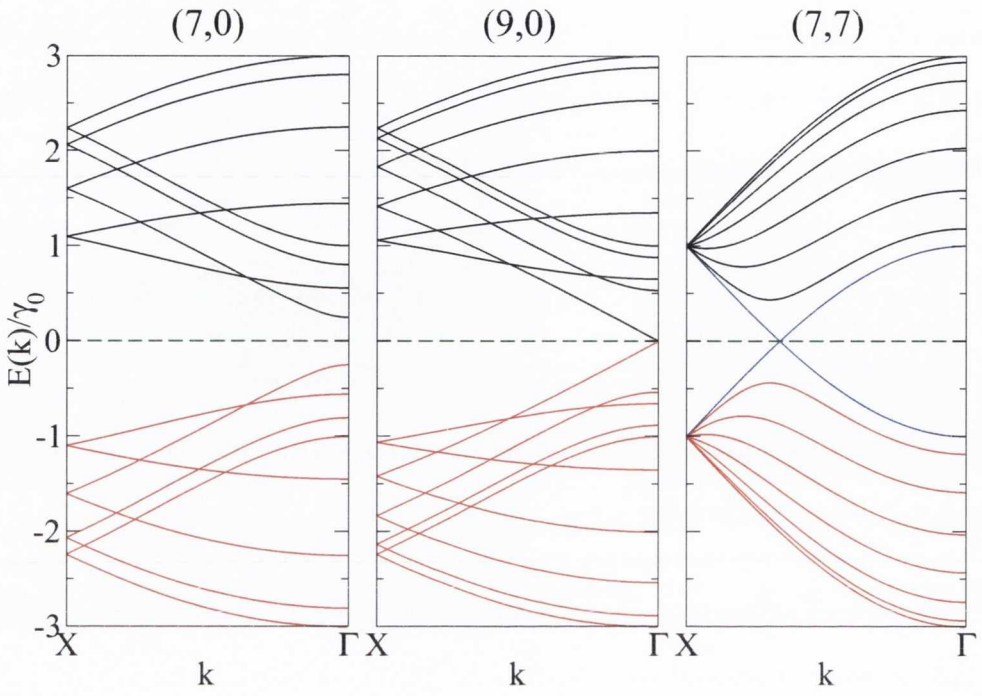

Figure 2.3: Energy dispersion relations for zigzag and armchair nanotubes. The zigzag (7,0) presents a clear defined energy gap, whereas (9,0) behaves as a metallic nanotube. The $(7,7)$ armchair nanotube is metallic. Notice the two bands crossing the Fermi energy at $E_F = 0.0\gamma_0$ (dashed line).

A nanotube is metallic when any of the quantisation lines cross the Fermi surface of graphene shown in figure 2.2(b), and semiconducting otherwise.

On Fig. 2.3 we plot the band structure of three different nanotubes, obtained with the above expressions, along the direction connecting the high symmetry points Γ and X. The Γ point is at the centre of the first Brillouin zone and corresponds to $k = 0$, whereas the X point corresponds to $k = \pm\pi/a$ for armchair nanotubes, and $k = \pm\pi/\sqrt{3}a$ for zigzag ones. $(7,0)$ is a semiconducting zigzag nanotube, and the energy band gap is quite clear. The other zigzag nanotube, $(9,0)$ has a metallic character, as the linear bands near the Γ point indicate. The metallic $(7,7)$ armchair nanotube has two energy bands crossing the Fermi level, located at $E_F = 0.0\gamma_0$.

An alternative and intrinsically related way of analysing the electronic structure of a material is by looking at its *density of states*. This quantity can be calculated

with the aid of Green functions. These mathematical structures are extremely useful in the study of several branches of theoretical physics, including, but not limited to condensed matter. In the next section, it will be shown how Green functions can be calculated directly from a Hamiltonian, and how they are related to the density of states. A simple formalism to estimate the effects of perturbations on the Green function of a system is also introduced with Dyson's equation. In the sequence, we move on to show how the conductance of a system can be written in terms of Green functions, which is a basis for the study of electronic transport in diverse materials.

2.2 Green Functions

Green function methods are arguably one of the most important and versatile items in the toolbox of a theoretical physicist. Green functions (GFs) are extremely useful in the study of meso- and nanoscopic physics [89]. In mathematics, the Green function provides a calculational tool to find the solution of a linear differential equation. This solution generally relates a response function with its source. In physics, the linear differential equation is usually the Schrödinger equation, which describes the electronic energy states of a system.

In typical solid state physics problems, the Green function of a system provides direct access to its density of states, which is an experimentally observable quantity. Theoretical predictions can be directly compared with experiments through, for example, scanning tunnelling microscopy [90]. Moreover, because the Green function can describe the propagation of electrons through a conducting system, a number of electronic transport methods have been developed based on direct application of Green functions [91, 92, 93, 94, 95].

Throughout this work we do not consider electron-electron interaction terms in the Hamiltonian, such that electrons interact only with the lattice potential. The

associated Green functions are often referred as single particle Green functions, and these are the focus of what follows.

The Green function associated with a given Hamiltonian can be defined as

$$\hat{\mathcal{G}}^{\pm} = \lim_{\eta \to 0} \left[(E \pm \imath\eta)\hat{1} - \hat{H} \right]^{-1}, \tag{2.13}$$

where $\hat{H}$ is the Hamiltonian chosen to describe the system, $\hat{1}$ is the identity operator, and the energy $E \to E \pm \imath\eta$ has acquired an infinitesimal imaginary part η. The small imaginary part added to the energy is necessary to avoid singularities on the Green function around eigenvalues of the Hamiltonian. The presence of a non-zero imaginary part destroys the Hermiticity of the operator and consequently the Green Function is not an observable. The limit can be taken in a positive (retarded) or negative (advanced) sense, which is denoted by $\pm$. The physical meaning of each limit is that the retarded Green function describes propagation away from the source, while the advanced Green function describes propagation towards the source. This distinction is particularly relevant when Green functions are used to calculate electronic transport on materials. For now, we can choose to work only with the retarded propagator.

The relation between the Green function and the density of states can be explicitly shown. Writing the Hamiltonian in a basis set of its eigenvectors $|\psi_\lambda\rangle$ we have

$$\hat{H} = \sum_{\lambda} |\psi_\lambda\rangle \varepsilon_\lambda \langle\psi_\lambda|. \tag{2.14}$$

Inserting this into equation (2.13), we obtain

$$\hat{\mathcal{G}} = \lim_{\eta \to 0} \sum_{\lambda} |\psi_\lambda\rangle \frac{1}{E + \imath\eta - \varepsilon_\lambda} \langle\psi_\lambda|. \tag{2.15}$$

In terms of a localised basis set $|j\rangle$, we can write the Green function as

$$\langle j|\hat{\mathcal{G}}|j'\rangle = \lim_{\eta\to 0}\sum_{\lambda}\langle j|\psi_\lambda\rangle\frac{1}{E+\imath\eta-\varepsilon_\lambda}\langle\psi_\lambda|j'\rangle \tag{2.16}$$

$$\langle j|\hat{\mathcal{G}}|j'\rangle = \lim_{\eta\to 0}\sum_{\lambda}\langle j|\psi_\lambda\rangle\frac{E+\imath\eta-\varepsilon_\lambda}{(E-\varepsilon_\lambda)^2+\eta^2}\langle\psi_\lambda|j'\rangle. \tag{2.17}$$

Setting $j = j'$ and taking the imaginary part we are left with

$$-\mathrm{Im}\langle j|\hat{\mathcal{G}}|j\rangle = \lim_{\eta\to 0}\sum_{\lambda}|\langle j|\psi_\lambda\rangle|^2\frac{\eta}{(E-\varepsilon_\lambda)^2+\eta^2}. \tag{2.18}$$

Comparing the above expression with the definition of the Dirac delta function

$$\delta(x) = \frac{1}{\pi}\lim_{a\to 0}\frac{a}{x^2+a^2}, \tag{2.19}$$

we can write

$$-\frac{1}{\pi}\mathrm{Im}\langle j|\hat{\mathcal{G}}|j\rangle = \sum_{\lambda}|\langle j|\psi_\lambda\rangle|^2\delta(E-\varepsilon_\lambda), \tag{2.20}$$

which is exactly the definition of the local density of states at site j. Furthermore, it is also possible to express the density of states explicitly as

$$\rho(E) = -\frac{1}{\pi}\mathrm{Im}\left\{\mathrm{Tr}[\hat{\mathcal{G}}(E)]\right\}, \tag{2.21}$$

where Tr represents the trace of the operator. From the density of states, several physical quantities can be calculated such as the number of particles, total energy, specific heat, conductivity, among others.

2.3 Dyson's Equation

Once we know the Green function $\hat{\mathcal{G}}$, associated with a given Hamiltonian $\hat{H}_0$, we might want to calculate the Green function $\hat{G}$, associated with a different Hamil-

tonian given by $\hat{H}_0 + \hat{V}$. One option is to diagonalise the new Hamiltonian, and use the definition of the Green function. However, there is a simpler method from the calculation point of view provided by Dyson's equation. Replacing the new Hamiltonian into equation (2.13), we obtain

$$\begin{aligned} \hat{G} &= \left[(E + \imath\eta)\hat{1} - (\hat{H}_0 + \hat{V})\right]^{-1} && (2.22) \\ &= \left[\hat{\mathcal{G}}^{-1} - \hat{V}\right]^{-1} && (2.23) \\ &= \left[\hat{1} - \hat{\mathcal{G}}\hat{V}\right]^{-1}\hat{\mathcal{G}}. && (2.24) \end{aligned}$$

Which can be multiplied from the left by $(\hat{1} - \hat{\mathcal{G}}\hat{V})$, to give Dyson's equation in its most common form

$$\hat{G} = \hat{\mathcal{G}} + \hat{\mathcal{G}}\hat{V}\hat{G}. \tag{2.25}$$

With direct application of equation (2.25) we can calculate the propagators of a perturbed system from those of the corresponding unperturbed system. This avoids the complication of having to diagonalise a new Hamiltonian. However, Dyson's equation in the above form still presents an inconvenience, which is the presence of $\hat{G}$ on the right hand side of the equation. If the perturbation $\hat{V}$ is weak, then we can expand (2.25) and keep only lower order terms, such that

$$\hat{G} = \hat{\mathcal{G}} + \hat{\mathcal{G}}\hat{V}\hat{\mathcal{G}} + \hat{\mathcal{G}}\hat{V}\hat{\mathcal{G}}\hat{V}\hat{\mathcal{G}} + \cdots . \tag{2.26}$$

Notice that the expansion is valid independent of the magnitude of $\hat{V}$, but only if the perturbation is small we can discard the higher order terms. With this simplification, the perturbed (or dressed) Green function $\hat{G}$ can be calculated directly from the unperturbed (or bare) Green function $\hat{\mathcal{G}}$, which is already known, and the small perturbation $\hat{V}$.

Alternatively, it is also possible to solve equation (2.25) for $\hat{G}$, as

$$(\hat{1} - \hat{\mathcal{G}}\hat{V})\hat{G} = \hat{\mathcal{G}} \tag{2.27}$$

$$\hat{G} = (\hat{1} - \hat{\mathcal{G}}\hat{V})^{-1}\hat{\mathcal{G}}, \tag{2.28}$$

which can be replaced back in equation (2.25) such that

$$\hat{G} = \hat{\mathcal{G}} + \hat{\mathcal{G}}\hat{V}(\hat{1} - \hat{\mathcal{G}}\hat{V})^{-1}\hat{\mathcal{G}}, \tag{2.29}$$

$$\hat{G} = \hat{\mathcal{G}} + \hat{\mathcal{G}}\hat{T}\hat{\mathcal{G}}, \tag{2.30}$$

where the scattering matrix was defined as $\hat{T} = \hat{V}(\hat{1} - \hat{\mathcal{G}}\hat{V})^{-1}$. Notice that, in general, even if $\hat{V}$ is energy independent, $\hat{T}$ is not necessarily so. Equation (2.30) also allows for the direct calculation of the dressed Green function associated with Hamiltonian $\hat{H}_0 + \hat{V}$, from the bare Green function associated with $\hat{H}_0$, and the perturbation $\hat{V}$. Furthermore, this approach does not require the perturbation to be small. Several systems can be treated by combining the use of Green functions and Dyson's equation. The perturbation can be, for example, an adsorbed atom on the system, a substitutional impurity, some sort of magnetic moment, or even a junction of the system with another one.

One apparent limitation of the GFs method is that the dimensions of the problem grow quickly with the number of particles involved. Consider a linear chain of identical atoms within a nearest neighbour tight binding Hamiltonian for example. For a finite chain, we can write the Hamiltonian matrix $\hat{H}$ and then numerically calculate its Green function $\hat{\mathcal{G}}$. The same is not true for an infinite system, since an infinite matrix cannot be defined for a numerical routine. One possible solution would be to consider very large finite matrices, but the problem would still be very computationally demanding. A solution for this problem is to apply the so-called *recursive Green functions method*. The method consists of considering the system

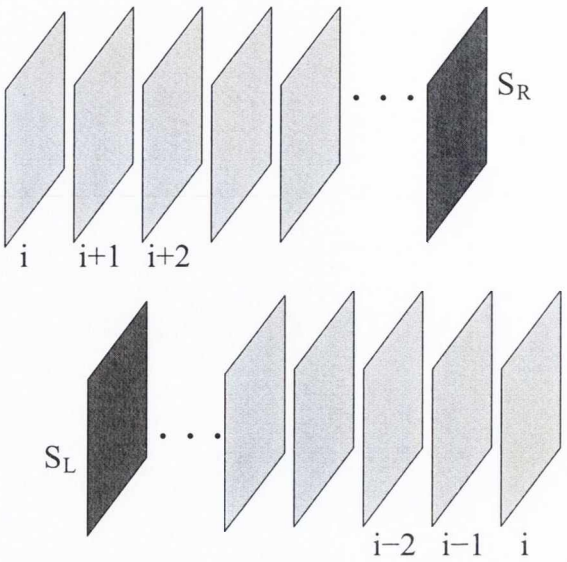

Figure 2.4: The recursive method can be applied to calculate the Green function of a layered structure as illustrated. Each layer is defined by its Hamiltonian $\hat{H}_i$ and respective GF $\hat{\mathcal{G}}_{ii}$. After a sufficient number of iterations the surface Green function of the semi-infinite structure is obtained.

as a layered structure, such that the whole infinite system can be built by adding layer over layer, one at a time [96]. In the next section we describe the method for a general system and apply it to carbon nanotubes.

2.3.1 The Recursive Method

The recursive Green function method can be applied to calculate the GF of a large system by considering it as a layered structure. Starting from a completely disconnected set of layers, Dyson's equation can be applied to connect adjacent layers one by one, by updating the Green function of the last connected element. The layers do not have to be identical, neither have the same size. All that is necessary is to write the appropriate Hamiltonians connecting each layer.

Consider a system as the one shown in figure 2.4, which is formed by an ensemble of disconnected layers, each one described by a Hamiltonian $\hat{H}_i$. The hopping matrices between adjacent layers is given by $\hat{t}_{i,i+1}$ and the respective adjoint $\hat{t}^{\dagger}_{i,i+1}$. Since the Hamiltonian of the system is Hermitian we have $\hat{t}^{\dagger}_{i,i+1} = \hat{t}_{i+1,i}$. The Green

function of each individual layer is given by $\hat{\mathcal{G}}_{ii} = \left[E\hat{I} - \hat{H}_i\right]^{-1}$. The propagators between the initial disconnected layers is naturally zero, thus $\hat{\mathcal{G}}_{i,i+1} = \hat{\mathcal{G}}_{i+1,i} = 0$. Using Dyson's equation to connect a layer labelled i to its neighbour $i+1$ we obtain

$$\hat{G}_{i+1,i+1} = \hat{\mathcal{G}}_{i+1,i+1} + \hat{\mathcal{G}}_{i+1,i+1}\hat{t}_{i+1,i}\hat{G}_{i,i+1}, \tag{2.31}$$

in a similar way we can write, with the aid of Dyson's equation

$$\hat{G}_{i,i+1} = \hat{\mathcal{G}}_{i,i}\hat{t}_{i,i+1}\hat{G}_{i+1,i+1}, \tag{2.32}$$

which replaced in the previous expression yields

$$\hat{G}_{i+1,i+1} = \left[\hat{1} - \hat{\mathcal{G}}_{i+1,i+1}\hat{t}_{i+1,i}\hat{\mathcal{G}}_{i,i}\hat{t}_{i,i+1}\right]^{-1}\hat{\mathcal{G}}_{i+1,i+1}. \tag{2.33}$$

In a similar construction, it is possible to connect layer i to its neighbour $i-1$. The Green function of the added layer will be given by

$$\hat{G}_{i-1,i-1} = \left[\hat{1} - \hat{\mathcal{G}}_{i-1,i-1}\hat{t}_{i-1,i}\hat{\mathcal{G}}_{i,i}\hat{t}_{i,i-1}\right]^{-1}\hat{\mathcal{G}}_{i-1,i-1}. \tag{2.34}$$

Equations (2.33) and (2.34) correspond to adding extra layers to the right hand side and to the left hand side of the original layer labelled i, respectively. Moreover, each equation gives the Green function of the element at the end, or surface, of the growing structure. With this interpretation in mind, after n layers have been added we can re-cast both equations as

$$\hat{S}_R^{n+1} = \left[\hat{1} - \hat{\mathcal{G}}_0\hat{t}_{LR}\hat{S}_R^n\hat{t}_{RL}\right]^{-1}\hat{\mathcal{G}}_0, \tag{2.35}$$

and

$$\hat{S}_L^{n+1} = \left[\hat{1} - \hat{\mathcal{G}}_0\hat{t}_{RL}\hat{S}_L^n\hat{t}_{LR}\right]^{-1}\hat{\mathcal{G}}_0, \tag{2.36}$$

where $\hat{\mathcal{G}}_0$ is the Green function of a single isolated layer. Equations (2.35) and (2.36) are recursive relations for the surface Green function of a structure grown by connecting independent layers. In the limit $\hat{S}^{n+1}_{R(L)} = \hat{S}^{n}_{R(L)}$, the surface Green functions converge to that of a semi-infinite structure. These relations are particularly useful in electronic transport calculations where it is necessary to have semi-infinite electrodes which mimic particle reservoirs.

Using the recursive method, and once again Dyson's equation, it is also possible to calculate the Green functions of an infinite structure. All that is necessary is to use Dyson's equation to connect two semi-infinite surface Green functions $\hat{S}_L$ and $\hat{S}_R$. The resulting expression for the propagator of the infinite structure is

$$\hat{G}_{ii} = \left[\hat{1} - \hat{S}_R \hat{t}_{RL} \hat{S}_L \hat{t}_{LR}\right]^{-1} \hat{S}_R. \tag{2.37}$$

As an illustration of the power of the recursive method, we apply it to calculate the Green function of pristine and doped carbon nanotubes, in the following section.

2.3.2 Application to Carbon Nanotubes

Applying the recursive Green function approach, we can calculate the Green function of infinite carbon nanotubes. Starting with a unit cell with $4n$ atoms, it is possible to write the unit cell Hamiltonian $\hat{H}_0$ as a $4n \times 4n$ matrix, from which the Green function matrix is calculated directly. The hopping matrices between adjacent unit cells connect the appropriate atoms in each side, and can also be written as $4n \times 4n$ matrices. Equations (2.35) and (2.36) are applied until each one converges to the semi-infinite nanotube propagators. Finally, the Green function of the infinite carbon nanotube is calculated from equation (2.37). Besides having the on-site propagators for each of the $4n$ carbon atoms in one unit cell, the calculated Green function also provides the propagators between any two atoms in

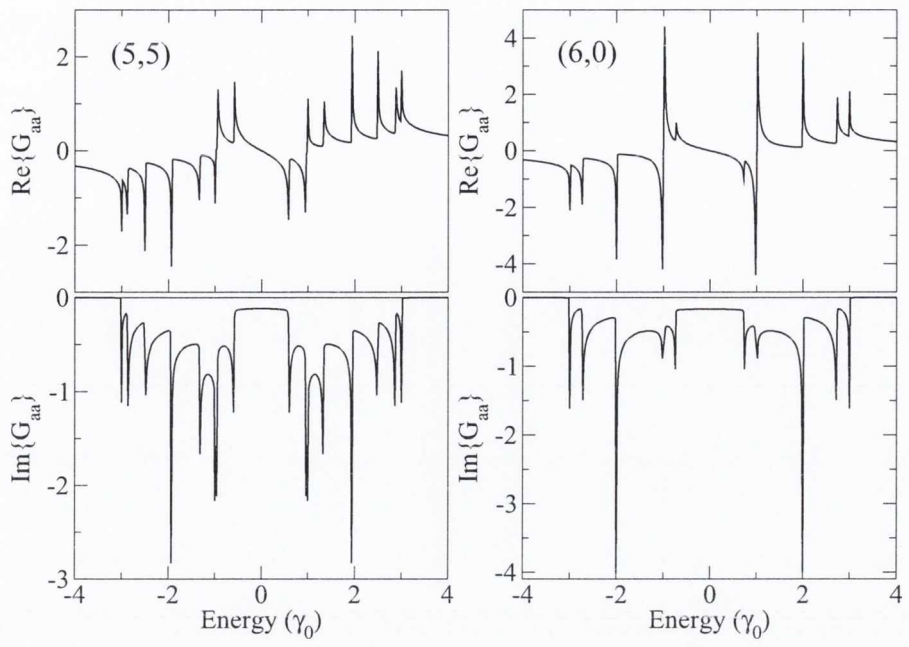

Figure 2.5: Green functions of pristine nanotubes calculated with the recursive method. Real and imaginary parts show singularities at specific energy values. The height of the spikes is inversely proportional to the small imaginary part η. For clarity we set $\eta = 10^{-3}$.

the same unit cell.

Figure 2.5 shows the energy dependence for real and imaginary parts of the on-site propagators for an armchair $(5, 5)$ nanotube and a $(6, 0)$ zigzag nanotube. Real and imaginary parts of the propagators show a series of singularities at specific energies. The spikes in the imaginary part are directly related to the Van Hove singularities characteristic of the density of states of 1D systems.

It is also possible to apply the recursive method to calculate the Green function of non-pristine carbon nanotubes. For example, some unit cells could contain different types of impurities adsorbed to one or more carbon atoms, and even have carbon atoms replaced by foreign elements. The recursive procedure described above is still applicable, as long as one can write the Green function of each unit cell, and the appropriate hopping terms between adjacent cells. In this fashion it is possible to study electronic transport across heterogeneous systems, with any concentration of impurities desired. The conductance is calculated from specific

Green function elements by direct application of the Kubo formula, as described in the next section.

2.4 Kubo Formula for Conductance

The frequency-dependent conductance of a system at zero temperature can be obtained, within linear response theory, from the Kubo formalism [97]. Specifically, the Kubo formula for the conductance is given by the expression [98]

$$\Gamma(\omega) = \frac{\pi}{\omega} \int dE \sum_{k,k';\, \varepsilon(k)<E_F<\varepsilon(k')} |\langle k|\hat{I}|k'\rangle|^2 \delta(E+\hbar\omega-\varepsilon(k'))\delta(E-\varepsilon(k)), \quad (2.38)$$

where $\hat{I}$ is the current operator, ω is the frequency, and E is the energy. The sum over k, k' is restricted to the eigenstates satisfying $\varepsilon(k) < E_F < \varepsilon(k')$, where E_F is the Fermi energy. In order to perform actual calculations, $\Gamma(\omega)$ can be expressed in terms of Green functions. Following the approach of Mathon et al. [99], it is possible to write the current operator $\hat{I}$ as the rate of charge crossing a surface S enclosing an arbitrary volume V. From Heisenberg's equation we can write

$$\hat{I} = \frac{ie}{\hbar} \sum_{i\in V} \sum_{j\notin V} \{\, |i\rangle t_{ij} \langle j| - |j\rangle t_{ji} \langle i| \,\}, \quad (2.39)$$

where the sum over i extends over all sites enclosed by S and the sum over j extends over all the sites outside the region.

Let us assume the volume V includes a semi-infinite part of a system, extending from the left as far as plane 0. The rest of the system then extends from plane 1 to infinite on the right. In this way, there is an imaginary "cleavage plane" located between planes 0 and 1 of the system. This cleavage plane does not necessarily correspond to a physical separation of the infinite system. It is just a convenient way to define a surface through which charge will flow. Assuming that each plane

only interacts with its nearest neighbours, we can write the current operator as

$$\hat{I} = \frac{\imath e}{\hbar} \sum_{a,b=1}^{N} \{ \, |0,a\rangle t_{0a,1b} \langle 1,b| - |1,a\rangle t_{1a,0b} \langle 0,b| \, \} \,, \tag{2.40}$$

where $|0,a\rangle$ represents an arbitrary atom a in plane 0, and $|1,b\rangle$ an equally arbitrary atom b in plane 1. The sum is over the total number of atoms in each plane, N.

Once we have defined the current operator, it is desirable to remove the restriction in the sum over eigenstates in equation (2.38). This can be accomplished with the aid of the Heaviside step function, defined as

$$\Theta(x) = \begin{cases} 1, & x \leq 0 \\ 0, & x > 0 \end{cases} \,.$$

We can then write

$$\sum_{k,k';\varepsilon(k)<E_F<\varepsilon(k')} |\langle k|\hat{I}|k'\rangle|^2 = \sum_{k,k'} |\langle k|\hat{I}|k'\rangle|^2 \Theta(\varepsilon(k) - E_F) \left[1 - \Theta(\varepsilon(k') - E_F + \hbar\omega)\right] . \tag{2.41}$$

Furthermore, using equation (2.40) we can expand the term with the current operator as

$$\begin{aligned} |\langle k|\hat{I}|k'\rangle|^2 &= -\frac{e^2}{\hbar^2} \left[\sum_{a,b=1}^{N} \langle k|0,a\rangle t_{0a,1b} \langle 1,b|k'\rangle - \langle k|1,a\rangle t_{1a,0b} \langle 0,b|k'\rangle \right] \\ &\times \left[\sum_{c,d=1}^{N} \langle k'|0,c\rangle t_{0c,1d} \langle 1,d|k\rangle - \langle k'|1,c\rangle t_{1c,0d} \langle 0,d|k\rangle \right] . \end{aligned} \tag{2.42}$$

Expanding the product we obtain

$$\begin{aligned} |\langle k|\hat{I}|k'\rangle|^2 &= -\frac{e^2}{\hbar^2} \sum_{a,b,c,d=1}^{N} [\langle k|0,a\rangle t_{0a,1b} \langle 1,b|k'\rangle \langle k'|0,c\rangle t_{0c,1d} \langle 1,d|k\rangle \\ &- \langle k|0,a\rangle t_{0a,1b} \langle 1,b|k'\rangle \langle k'|1,c\rangle t_{1c,0d} \langle 0,d|k\rangle \\ &- \langle k|1,a\rangle t_{1a,0b} \langle 0,b|k'\rangle \langle k'|0,c\rangle t_{0c,1d} \langle 1,d|k\rangle \end{aligned}$$

$$+ \quad \langle k|1,a\rangle t_{1a,0b}\langle 0,b|k'\rangle\langle k'|1,c\rangle t_{1c,0d}\langle 0,d|k\rangle] \tag{2.43}$$

We can now address the delta functions in equation (2.38). It has been shown in section 2.2 that the imaginary part of the on-site Green function is a delta function. Considering the advanced and the retarded Green functions, we can write

$$\hat{G}^- - \hat{G}^+ = 2\imath\eta\hat{G}^+\hat{G}^-. \tag{2.44}$$

From equations (2.13) and (2.15), we get

$$\begin{aligned} \hat{G}^- - \hat{G}^+ &= 2\imath\eta\sum_k |k\rangle \frac{1}{E-\varepsilon(k))^2-\eta^2}\langle k| && (2.45)\\ &= 2\imath\eta\sum_k |k\rangle\delta(E-\varepsilon(k))\langle k|, && (2.46) \end{aligned}$$

and we can define

$$\begin{aligned} \tilde{G}_{ij} &= \frac{1}{2\imath}(\hat{G}^-_{ij} - \hat{G}^+_{ij}) && (2.47)\\ &= \pi\sum_k \langle i|k\rangle\delta(E-\varepsilon(k))\langle k|j\rangle. && (2.48) \end{aligned}$$

Replacing equations (2.43) and (2.41) into (2.38), and using the relation in (2.48), we get

$$\begin{aligned} \Gamma(\omega) &= \frac{\pi}{\omega}\left(-\frac{e^2}{\pi^2\hbar^2}\right)\int dE\,\Theta(\varepsilon(k)-E_F)[1-\Theta(\varepsilon(k)-E_F+\hbar\omega]\\ &\times \mathrm{Tr}[\tilde{G}_{10}(E)t_{01}\tilde{G}_{10}(E+\hbar\omega)t_{01} - \tilde{G}_{00}(E)t_{01}\tilde{G}_{11}(E+\hbar\omega)t_{10}\\ &- \tilde{G}_{11}(E)t_{10}\tilde{G}_{00}(E+\hbar\omega)t_{01} + \tilde{G}_{01}(E)t_{10}\tilde{G}_{01}(E+\hbar\omega)t_{10}] \end{aligned} \tag{2.49}$$

The trace extends over all intra-plane degrees of freedom, and includes individual atoms, atomic orbitals, spin states, and any other degrees of freedom present in the system. Because of the presence of the Heaviside functions, the integration is

straightforward. In the limit $\omega \to 0$ we obtain the DC conductance as

$$\begin{aligned}\Gamma(\omega=0) &= \frac{2e^2}{h}\mathrm{Tr}[\,\tilde{G}_{10}(E_F)t_{01}\tilde{G}_{10}(E_F)t_{01} - \tilde{G}_{00}(E_F)t_{01}\tilde{G}_{11}(E_F)t_{10} \\ &- \tilde{G}_{11}(E_F)t_{10}\tilde{G}_{00}(E_F)t_{01} + \tilde{G}_{01}(E_F)t_{10}\tilde{G}_{01}(E_F)t_{10}\,], \qquad (2.50)\end{aligned}$$

which can be further simplified to read [99]

$$\Gamma(\omega=0) = \frac{4e^2}{h}\,\mathrm{Re}\left\{\mathrm{Tr}[\,\tilde{G}_{00}(E_F)t_{01}\tilde{G}_{11}(E_F)t_{10} - t_{01}\tilde{G}_{10}(E_F)t_{01}\tilde{G}_{10}(E_F)\,]\right\} \qquad (2.51)$$

Equation (2.51) expresses the Kubo formula in terms of Green functions of adjacent layers of a generic system. The choice of adjacent layers is arbitrary, and in general, they are chosen far from major scattering regions. Fisher and Lee [100] have shown that in the DC limit, the Kubo formula and the Landauer-Büttiker formulas are equivalent, by relating the Transmission Matrix of the later with the Green functions in equation (2.51). Finally, it is worth emphasising that equation (2.51) is quite general and can be applied to calculate the zero-bias conductance along several types of systems, including carbon nanotubes. In the following section we describe the procedure for the case of pristine and doped carbon nanotubes.

2.4.1 Application to Carbon Nanotubes

As we have mentioned in chapter 1, pristine metallic carbon nanotubes are ballistic conductors, suggesting that typical values for the mean free path of the conduction electrons are larger than the length of the system. These conduction electrons travel along the nanotubes being weakly scattered, and the material has a very low resistivity. It is possible to illustrate the use of the Kubo formula by applying it to calculate the conductance spectrum of pristine and even doped carbon nanotubes.

First, the recursive method is applied to calculate the advanced and retarded surface Green functions of pristine infinite nanotubes. The surface Green functions

are denoted by $\hat{S}_L^{\pm}$ and $\hat{S}_R^{\pm}$. Next, using Dyson's equation to connect both sides, we get the connected system Green functions

$$\begin{aligned}
\hat{G}_L^{\pm} &= \left(\hat{1} - \hat{S}_L^{\pm}\hat{t}_{LR}\hat{S}_R^{\pm}\hat{t}_{RL}\right)^{-1}\hat{S}_L^{\pm}, \\
\hat{G}_R^{\pm} &= \left(\hat{1} - \hat{S}_R^{\pm}\hat{t}_{RL}\hat{S}_L^{\pm}\hat{t}_{LR}\right)^{-1}\hat{S}_R^{\pm}, \\
\hat{G}_{RL}^{\pm} &= \hat{S}_R^{\pm}\hat{t}_{RL}\left(\hat{1} - \hat{S}_L^{\pm}\hat{t}_{LR}\hat{S}_R^{\pm}\hat{t}_{RL}\right)^{-1}\hat{S}_L^{\pm} = \hat{S}_R^{\pm}\hat{t}_{RL}\hat{G}_L^{\pm}.
\end{aligned} \tag{2.52}$$

The terms $\hat{G}_L^{\pm}$ and $\hat{G}_R^{\pm}$ are the Green functions of an infinite carbon nanotube, corresponding to adjacent unit cells separated by an imaginary "cleavage" plane. The last equation in (2.52) gives the advanced and retarded propagators between the adjacent planes. Finally, we obtain the conductance of the system by applying the Kubo formula in the form

$$\Gamma(E) = \left(\frac{4e^2}{h}\right)\mathrm{Re}\left\{\mathrm{Tr}\left[\tilde{G}_L\hat{t}_{LR}\tilde{G}_R\hat{t}_{RL} - \hat{t}_{LR}\tilde{G}_{RL}\hat{t}_{LR}\tilde{G}_{RL}\right]\right\}, \tag{2.53}$$

where we recall the auxiliary Green functions are defined as

$$\tilde{G} = \frac{1}{2\imath}\left[\hat{G}^{-} - \hat{G}^{+}\right]. \tag{2.54}$$

To calculate the conductance along a non-pristine carbon nanotube it is still possible to follow the same procedure, albeit at least one extra step is required. Once $\hat{S}_L^{\pm}$ and $\hat{S}_R^{\pm}$ have been calculated for pristine semi-infinite structures, we can use the add layer procedure, developed from Dyson's equation in the recursive method section, to include non-pristine unit cells in one (or both) sides. After all the defective sections have been added to the nanotube, and the surface Green functions updated, we resume to the applications of (2.52) and (2.53). In general, a few more pristine unit cells are added after the surface before calculating $G_{L(R)}^{\pm}$, such that the conductance is calculated far from the major scattering region.

Following the above description the conductance along pristine and doped car-

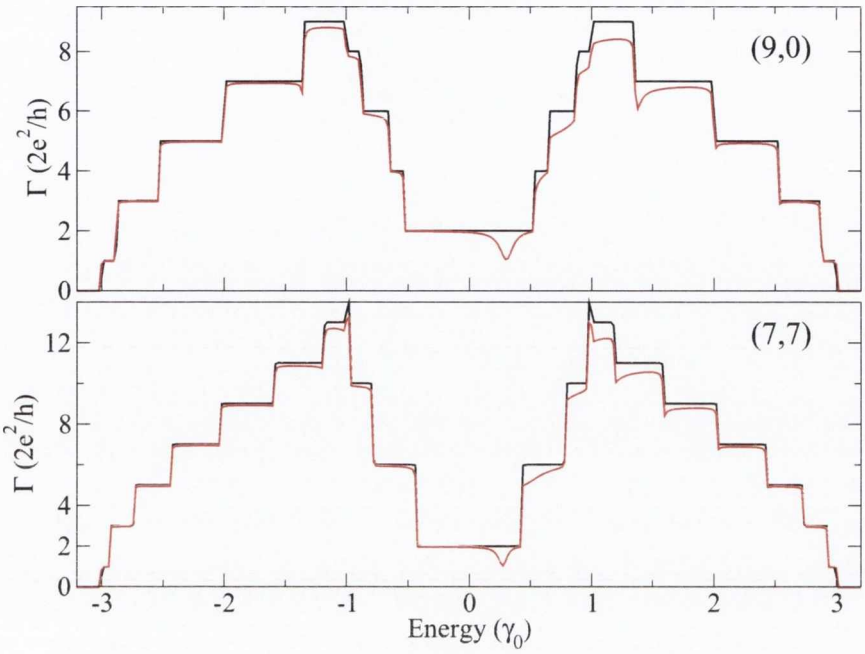

Figure 2.6: Zero-bias conductance along pure (black) and doped (red) metallic carbon nanotubes calculated using the Kubo formula. Pristine metallic tubes present two conducting channels at the Fermi level $E_F = 0.0\gamma_0$, which corresponds to a conductance of $4e^2/h$. The presence of a single adsorbed atom can reduce the conductance along the nanotube on a wide range of energies, as shown by the red solid line.

bon nanotubes is calculated. The doped nanotube has an impurity adsorbed to one of the carbon atoms on its surface. Figure 2.6 shows the conductance spectrum for the pristine and doped nanotubes considered. The presence of impurities or defects in nanotubes can affect the conductance dramatically. Vacancies or substitutional impurities are seen by conduction electrons as scattering centres, reducing the conductivity of the nanotubes [101]. Adsorbed impurities (single atoms or polymer chains) change the hybridisation of the carbon atom to which they are attached from the usual sp^2 to sp^3, which causes them to interfere with travelling electrons, particularly at resonance energies of the adsorbed structure [102]. The considered adatoms have an on-site energy $\epsilon = 0.5\gamma_0$, being above the Fermi level of the nanotubes by the same amount. It can be noticed that, for these metallic tubes, the adatom can reduce the conductance by one quantum (Γ_0) near the Fermi energy of the nanotube, leaving only one ballistic conducting channel available for electronic

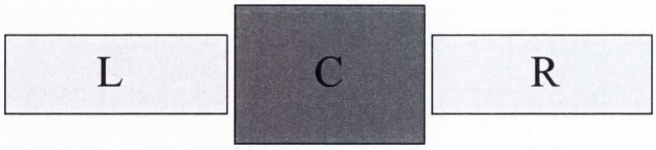

Figure 2.7: Schematic representation a physical system divided in left and right leads (L, R), and a central scattering region (C). The conductance through the system can be calculated with the Kubo formula.

transport. This phenomenon has led to the proposal of using carbon nanotubes as gas sensors, since certain molecules could easily be adsorbed at the nanotube surface [103].

Finally, the Kubo formula can be used to calculate the conductance of systems other than long layered structures. Since we are particularly interested in studying charge transport across disordered nanotube networks, we have to adapt the Kubo formalism to these systems. In the next section we show how the conductance of a tripartite system can be calculated directly from the Kubo formula, with an appropriate choice of Green functions.

2.5 General Method for Conductance

The Kubo formula can also be used to calculate the conductance of a tripartite system. In this case, a system is divided into semi-infinite leads and a central scattering region. The advantage of separating the system in three parts is that two of these – the leads – can in general be treated in a simpler way than the third one – the central scattering region. This is the standard construction implemented today in electronic transport calculation methods applied to meso- and nanoscopic systems. This general formalism was first introduced by Caroli, Comberscot and collaborators in a series of elegant papers in the 1970's [104, 105, 106, 107].

Figure 2.7 shows a schematic representation of a tripartite physical system composed of semi-infinite leads (L,R) and a central scattering region (C). In general,

the central region might be a single atom; a molecule; a portion of a carbon nanotube or a nanowire; or even a complex device such as an array of molecules or carbon nanotubes. The general procedure consists of starting from a completely disconnected system and work with some type of Dyson's equation to connect each part.

In order to calculate the conductance of the system shown in figure 2.7 with the Kubo formula, it is necessary to have the Green functions of the connected system on each side of the interfaces between L and C, or C and R. Starting from a completely disconnected system, we can write the Green functions as a block matrix

$$\hat{g} = \begin{pmatrix} \hat{g}_L & 0 & 0 \\ 0 & \hat{g}_C & 0 \\ 0 & 0 & \hat{g}_R \end{pmatrix}, \tag{2.55}$$

where each term in $\hat{g}$ is a matrix itself. These terms represent the Green functions of each of the three parts of the system, when disconnected from each other. Typically, $\hat{g}_L$ and $\hat{g}_R$ are surface Green functions of a semi-infinite structure, which physically represents an electrode or lead, and is calculated with the recursive method.

The connections between separate parts of the system are introduced through hopping matrices connecting adjacent parts. The connecting Hamiltonian can be written as

$$\hat{V} = \begin{pmatrix} 0 & \hat{V}_{LC} & 0 \\ \hat{V}_{LC}^{\dagger} & \hat{V}_{CC} & \hat{V}_{CR} \\ 0 & \hat{V}_{CR}^{\dagger} & 0 \end{pmatrix}, \tag{2.56}$$

where again each term is a matrix itself. The matrix $\hat{V}_{CC}$ accounts for the possibility of the central scattering region being composed of individual objects, as is the case in nanotube and nanowire networks.

The Green function of the whole interconnected system is calculated with

Dyson's equation, as $\hat{G} = \left(\hat{1} - \hat{g}\hat{V}\right)^{-1} \hat{g}$, and yields

$$\hat{G} = \begin{pmatrix} \hat{G}_L & \hat{G}_{LC} & 0 \\ \hat{G}_{CL} & \hat{G}_C & \hat{G}_{CR} \\ 0 & \hat{G}_{RC} & \hat{G}_R \end{pmatrix}. \tag{2.57}$$

The above described procedure has to be done for retard and advanced Green functions. Finally, the conductance can be directly calculated from the Kubo formula by using the respective Green functions of the fully connected system. Similarly to the case of a single carbon nanotube, the conductance of the tripartite system, in terms of Green functions is also given by

$$\Gamma(E) = \left(\frac{4e^2}{h}\right) \mathrm{Re}\left\{\mathrm{Tr}\left[\tilde{G}_L \hat{t}_{LR} \tilde{G}_R \hat{t}_{RL} - \hat{t}_{LR} \tilde{G}_{RL} \hat{t}_{LR} \tilde{G}_{RL}\right]\right\}, \tag{2.58}$$

where

$$\tilde{G} = \frac{1}{2i}\left[\hat{G}^- - \hat{G}^+\right]. \tag{2.59}$$

The procedure described in this section is analogous to the one usually implemented in conjunction with the Landauer-Bütiker formula [91, 108]. However, the methodology presented here has one advantage over the later because it does not require the calculation of the central region's Green function directly from the Hamiltonian. This advantage will become particularly clear in chapter 4 when we show how the Green function of an interconnected array of nanotubes can be written from just a few elements of an individual nanotube's propagators.

2.6 Summary of the Chapter

The general theoretical formalism applied throughout this thesis work has been introduced. The electronic structure of individual carbon nanotubes is described

within a single orbital tight binding Hamiltonian. In spite of its simplicity, this semi-empirical method is capable of capturing all the relevant information regarding the electronic band structure of nanotubes. The Green functions formalism was also introduced, which provides a direct and transparent way to treat a plethora of meso- and nanoscopic systems. In combination with Dyson's equation, the recursive Green function method was introduced, and applied to calculate the propagators of infinitely long carbon nanotubes. The Kubo transport formalism was also introduced and an expression for the conductance in terms of Green functions was derived. The conductance spectrum of pristine and doped carbon nanotubes was calculated by a combination of the recursive GF method with the Kubo formula. Finally, the chapter concluded with a simple generalisation of the Kubo formula, such that it can be directly applied to tripartite systems. This final development is a fundamental part of the investigation of electronic transport in carbon nanotube networks, presented in chapter 4.

Chapter 3

Macroscopic Modelling of Carbon Nanotube Networks

3.1 Introduction

Carbon nanotubes (CNTs) have a typical diameter of ≈ 1 nm, while their length is roughly ≈ 1 μm. Because of their high *aspect ratio*, defined as the length-to-diameter ratio, CNTs are generally considered as one-dimensional conductors. The high aspect ratio of individual carbon nanotubes is also present in CNT bundles, which are held together by van der Waals interactions, and can extend in length to ≈ 1 cm. Films made of carbon nanotube networks can be produced by deposition of solutions containing dispersed CNT bundles [54, 84]. A typical film produced by this technique is shown in figure 3.1, from which one can observe the small diameter of nanotubes and bundles, as well as the complex topology of the networks formed. The conductivity of CNT films can be measured by depositing metallic electrodes on the sides of the films, and employing a usual two probe method.

Modelling a complex structure such as carbon nanotube network films is a huge challenge. First, a successful model needs to account for the disordered nature of the arrays formed by individual nanotubes and bundles. Moreover, it is

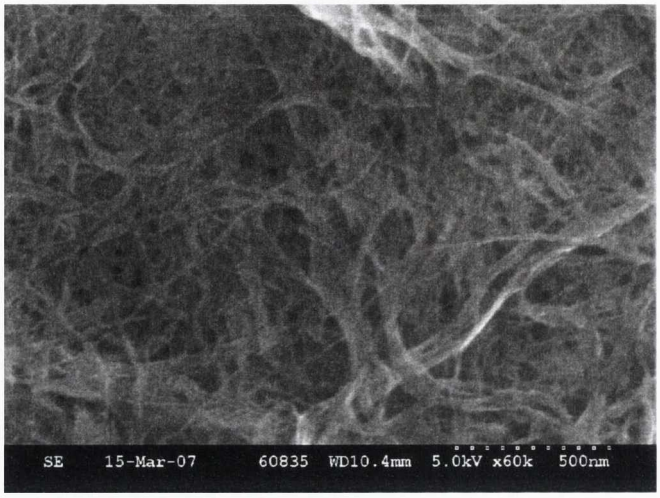

Figure 3.1: Micrograph of a typical carbon nanotube film produced by deposition of a solution containing dispersed nanotube bundles. Image is courtesy of J. N. Coleman's research group, Trinity College Dublin.

also necessary to account for the electronic coupling between individual nanoscopic components throughout the films. The geometrical aspects of individual CNTs and bundles call for the development of a model where each component is mimicked by a finite rigid rod. Furthermore, the disordered arrangements observed in the microscopy image of figure 3.1, is a perfect candidate to the application of percolation theory, among other methods developed for the study of complex systems.

Nanotube films can be modelled with the aid of standard stick percolation models, where rods of finite length and specified aspect ratio represent individual CNTs and bundles. This approach is very well suited to investigate the formation of interconnected paths along the networks, and this process can be analysed in detail. The study of percolation models by far predates the current interest on nanoscale systems, as well as nanotechnology itself. Carbon nanotube network models benefit from well established percolation studies, which can be extended and adapted to the particular case of interest.

Besides the geometrical structure of carbon nanotube network films, it is also necessary to understand how electronic transport takes place across the networks.

Since their first reported observation [2], carbon nanotubes have attracted much attention from the scientific community. One of the reasons for the huge interest on CNTs comes from their remarkable electronic transport properties, namely the fact that electrons can move along the length of an individual nanotube with very low resistance [6, 88, 109]. The remarkable ballistic transport characteristic of CNTs has almost instantaneously made them a wonder material for nanoscale electronic applications [9, 14, 15, 16, 110, 111].

However, large scale devices based on carbon nanotubes, such as CNT-based flexible electronic displays, cannot rely on ballistic charge transport alone. Despite the advances on fabrication methods for CNTs, the length of individual nanotubes and small diameter bundles is still limited to about 1 cm. Moreover, the production of pristine carbon nanotubes is extremely difficult to achieve, and the presence of impurities can have severe adverse effects on the conductance of nanotubes [6, 22, 88, 101, 112].

Electronic transport between individual nanotubes has been studied by experimental [73] and theoretical [75] works. It has been found that the resistance at CNT junctions is considerably higher than the intrinsic resistance along individual nanotubes. This is caused by the low probability of electrons tunnelling from one nanotube to another, which is a direct consequence of the weak interaction between CNTs through van der Waals forces. It is not hard to extrapolate the junction dominated resistance from a situation involving a single crossing to the case of a disordered network comprised of several thousand junctions per unit volume. This is precisely the case for carbon nanotube films. Even though it is possible to use high quality, high purity CNTs to produce thin films, the overall network resistance is dominated by the tunnelling barriers located at the junctions formed by nanotubes and bundles.

From a macroscopic point of view, it is possible to model the tunnelling barrier at junctions as Ohmic resistances. In practice, both the tunnelling barrier and the

resistor have the effective function of opposing the flux of electrons at that specific point. Therefore, a carbon nanotube film can be modelled as a disordered network of resistances, also known as a *resistive network*. In these networks, nodes represent perfect conductors and vertices are represented by Ohmic resistors. The resistance between arbitrary nodes of regular (as opposed to complex) resistive networks has been investigated by many authors over the years [113, 114, 115, 116, 117, 118, 119], and different methodologies have been developed to address the problem. However, resistive networks with a complex structure, such as scale-free or random graphs [120] for example, have not received the same degree of attention.

In this chapter we present our contribution to the study of electronic transport on carbon nanotube network films, which is a combination of rigid rod percolation models with the methods developed for the study of resistive networks. We begin by investigating how the density of the network is related to the junctions between individual rods, as well as the connections with the metallic electrodes, in section 3.2. The relation between network connectivity and concentration of conducting rods is very useful in the analysis of how the network morphology affects the conductance of nanotube films. In section 3.3 we review previous methods developed to calculate the equivalent resistance between arbitrary nodes of resistive networks, and present our own method, along with some applications on regular square lattices. Finally, in section 3.4, we apply our equivalent resistance calculation procedure to complex disordered networks of conducting rigid rods. The simulation results presented in section 3.4 are compared with experimental results, and present a remarkable qualitative agreement with studies of resistance on real carbon nanotube films. This chapter concludes with a brief summary in section 3.5.

3.2 Random Networks of Finite Rods

The complex disordered structure of carbon nanotube films can be modelled by standard geometric percolation models. Single nanotubes and small diameter bundles are modelled by finite-sized rigid rods of specific length and diameter. The structure of the film itself can be represented by a 3D box, which encloses the disordered array of rigid rods. It is important to defined a box with appropriate dimensions, such that most rods are located inside the box. Also, it is important to attempt to reproduce other aspects present on the real systems we aim to simulate, such as the placement of metallic electrodes on the sides of the films for electrical resistance measurements.

Once the aspect ratio of the rods, defined as length-to-diameter ratio, and the dimensions of the enclosing box are defined, it is also necessary to specify the total number of rods inside the box, i.e. the number of nanotubes in the film. The total number of rods considered, as well as the dimensions of the box, determine the density of the film. The density of a specific CNT network film can also be expressed in terms of its volumetric fraction occupied by nanotubes. The *volume fraction* of a typical laboratory produced carbon nanotube film is related to the concentration of CNTs in the solution used to produce the film, and to the volume of solution used. In the laboratory, the volume fraction can be calculated directly from the known density of carbon nanotubes and the measured density of the film. In our simulations, the volume fraction depends on the total number of rods distributed inside the box, and can be directly computed for each configuration of rods generated.

In our computer simulations, each rod is placed in a random location inside the box, and is oriented in a random direction defined in a 3D space. By choosing random orientations for the rods we aim to compensate, at least partially, for their lack of flexibility, as mentioned in chapter 1. Individual rods are allowed to overlap

with other rods, and each rod might also have part of its volume located outside the box. Each ensemble of randomly positioned rigid rods gives rise to a random complex network of interconnected 1-dimensional elements, capable of capturing the most important morphological features found on carbon nanotube films. Figure 3.2 shows a typical configuration generated with $N = 300$ identical rigid rods of length-to-diameter ratio equal to 20.

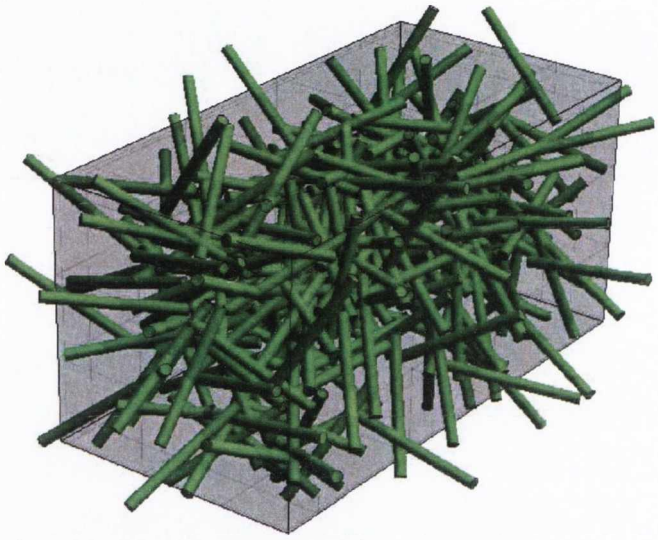

Figure 3.2: Illustrative representation of rigid rods randomly placed inside a rectangular box. There is a total of $N = 300$ identical rods inside the box, each with aspect ratio $\ell/D = 20$.

It is possible to map the interconnections between rods throughout the network by considering the centre-to-centre distance between each pair of rods, illustrated in figure 3.3. The centre-to-centre distance is first calculated at the end point of the rods, and then it is minimised through a numerical procedure. If the smallest centre-to-centre distance between a given pair of rods is smaller than their diameter, then this pair is said to be connected. By calculating the distance between each possible pair of rods in the network we map all the connections present in the network. Furthermore, following this procedure we obtain the list of contacting "neighbours" of each rod. In general, each rod will have an arbitrary number of such neighbours, whereas the number of connections (neighbours) per rod follows

some probability distribution with a well defined mean. The average number of connections per node defines the connectivity of the network. Networks with a low density of rods, i.e. a small volume fraction, are expected to have low connectivities, while networks with a large volume fraction will have high connectivities. In other words, the density of junctions in a network film depends directly on its volume fraction.

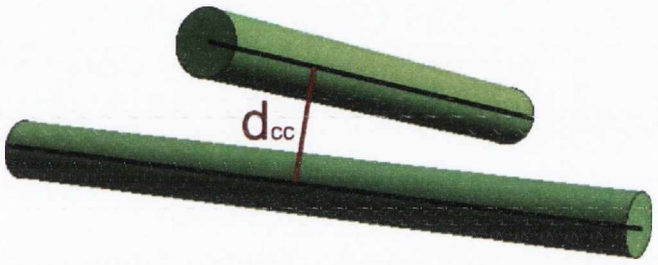

Figure 3.3: Schematic representation of the centre-to-centre distance between two rigid rods, d_{cc}. Starting from the centre-to-centre distance at the end of the rods, the distance is minimised though a numerical procedure. If the minimum value of d_{cc} is smaller than the diameter of the rods, than these rods are deemed connected.

Since we are interested in simulating electronic transport across random network of conducting rods, we have to include the placement of metallic electrodes in our model films. Contacts to electrodes are crucial to electronic transport studies, and we aim to address this issue as accurately as possible. In general experimental realisations, metallic electrodes are placed at opposing ends of a film, and the resistance is measured between these electrodes in a usual two probe method. In our model, the electrodes are modelled by two opposing faces of the 3D box. In other words, we consider metallic electrodes to be located on two opposing faces. Any rod crossing one of the designated electrode faces is considered to be in contact with that specific electrode, and we map which of the rods in the network are in this situation.

3.2.1 Simulation Details

In the simulations, individual carbon nanotubes are represented by rigid rods of length ℓ and diameter D, with a well defined aspect ratio given by ℓ/D. The geometry of the film itself is mimicked by a rectangular cuboid, whose dimensions are defined in terms of the rod length ℓ. In all the results reported here, we have considered the box to have dimensions given by $2\ell \times 2\ell \times 4\ell$. For each rod, a random position for one of its ends is generated inside the box, while the position of the other end is determined by the orientation of the rod. The total number of rods considered in each film is N, and along with ℓ and D, these are the parameters of the computer simulations.

We consider network films where the orientation of the rods is chosen at random from all the possible directions in a 3D space. The volume fraction of each configuration is calculated by summing up the volume occupied by all rods. A particular rod can have one of its endings located outside the box, and the portion located outside of the film is not considered when calculating the volume fraction. Rods are allowed to overlap with other rods, which might lead to an overestimation of the volume fraction, especially in the case of very dense networks. However, this possible overestimation of the volume fraction does not affect the morphology of the resulting networks.

Electrodes are located on the $2\ell \times 2\ell$ faces of the box, and rods crossing one of those faces are considered to be connected to that electrode. The box is defined with a separation large enough to avoid an individual rod being connected to both electrodes. Furthermore, we choose the box dimension such that the minimum path between the electrodes requires visiting at least 4 individual rods. This particular length was chosen in order to prevent short circuits between the electrodes.

For a fixed number of rods, and a box of fixed dimensions, a very large number of configurations can be generated by randomly distributing the rods. Therefore, a large number of independent configurations must be considered, and a careful

statistical analysis of the results must be carried out. All the results reported in the next section are obtained by averaging a large number of independent realisations, without discarding any configuration.

In order to determine which pairs of rods are connected we have to calculate the minimum distance between each rod and all the rods around it. Furthermore, identifying which rods cross the electrode faces also requires testing the criteria for all the rods close to the respective faces. Both procedures can be very time consuming from the computational point of view, and the computation time grows very rapidly with the total number of rods considered. In all of our simulations we have considered networks with a maximum of 1800 individual rods.

3.2.2 Results

In this section we present results for the dependence of the film volume fraction, V_f, as well as the average connectivity per rod, $\langle \alpha \rangle$, and the number of rods connected to the electrodes (per unit area), $\langle \alpha_E \rangle$, with the parameters of the model: N, ℓ and D. In general, the calculated quantities are expected to depend on the specific value of the parameters, however, whenever possible we intend to obtain universal relations for the network properties. Such universal scaling relations will provide a way to directly compare simulation results with experimental measurements, as well as combining both, in order to estimate quantities that cannot be directly measured in a laboratory.

We begin by analysing the relation between the total number of rods and the volume fraction of the resulting networks. As previously mentioned, nanotube network films can be produced by filtration of a solution containing dispersed CNTs. Experimental studies have found a direct relation between the volume of solution applied to the filter and the density (volume fraction) of the resulting

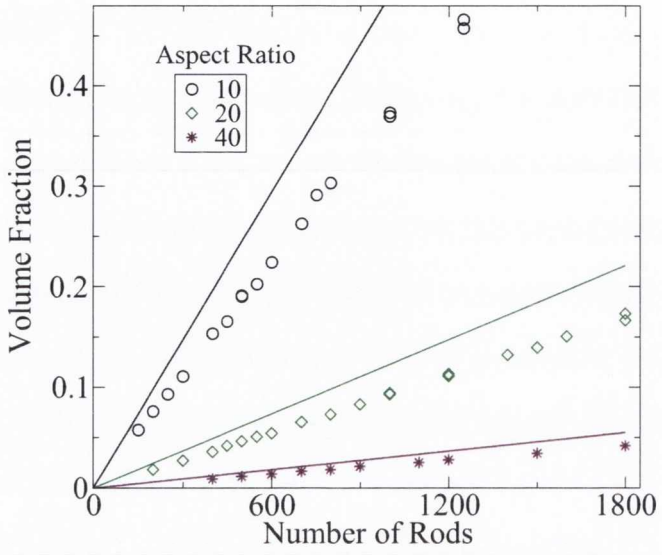

Figure 3.4: Dependence of the volume fraction on the total number of rods. Solid lines are given by equation (3.2), and data points are simulation results. Error bars are smaller than symbol sizes.

network [77]. The volume fraction can be directly calculated from its definition,

$$V_f = \frac{V_{tubes}}{V_{film}} = \frac{N v_{tube}}{V_{film}}, \tag{3.1}$$

where V_{tubes} is the total volume occupied by nanotubes, N is the number of tubes, v_{tube} is the volume occupied by a single nanotube, and V_{film} is the total volume of the film. Notice that by taking $V_{tubes} = N v_{tube}$ we neglect any overlap between individual tubes and assume that all nanotubes lie within the volume of the film. In terms of the simulation parameters $v_{tube} = \ell \pi D^2/4$ and $V_{film} = 16\ell^3$, such that the volume fraction can be written as

$$V_f = \frac{\pi}{64}\left(\frac{\ell}{D}\right)^{-2} N. \tag{3.2}$$

Figure 3.4 shows the relationship between the volume fraction and the total number of rods randomly placed inside the film. The data is shown for rods of different aspect ratio, which is controlled by adjusting the diameter of the rods. The solid

lines are given by equation (3.2), for the respective aspect ratio, while each data point is an average over several independent configurations simulated, with error bars smaller than symbol sizes. The difference between the analytical expression represented by the solid lines and the simulation data is a consequence of the assumptions made by setting $V_{tubes} = Nv_{tube}$ on the derivation of equation (3.2), while on the simulations V_{tubes} is directly computed by summing up the volume occupied by each cylinder inside the box representing the film and ignoring any portions of a rod laying outside of the film. If two rods overlap at some region inside the film, the overlapping volume is taken into account twice at the calculation of V_{tubes} in the simulations, but this double counting is only significant at very high densities. The simulation data shows a clear linear dependence of V_f with N, in accordance with the analytical derivation. This is an intuitive result from a geometrical point of view. Nonetheless, it is also in agreement with experimental observations [77], where the number of nanotube in the film is controlled by the volume of solution filtered.

Since we increase the aspect ratio of the rods by decreasing the diameter while not changing the length, rods of higher aspect ratio have a smaller individual volume when compared to rods of lower aspect ratio. Because of this, a larger number of rods of higher aspect ratio is required to obtain a network with the same volume fraction one would get with a smaller number of lower aspect ratio rods, as can also be seen in figure 3.4. The existence of such a direct relation between the total number of rods and the volume fraction of the networks, provides a direct way of comparing and combining simulation results with experimental measurements. On a real CNT film there are several thousand individual nanotubes, whereas computational resources limit simulations to only a few hundreds of rods. However, as we shall demonstrate, morphological properties of the networks, such as the connectivity and the density of junctions, are directly related to the volume fraction of the films, which connects experiment and simulation at least on a qualitative

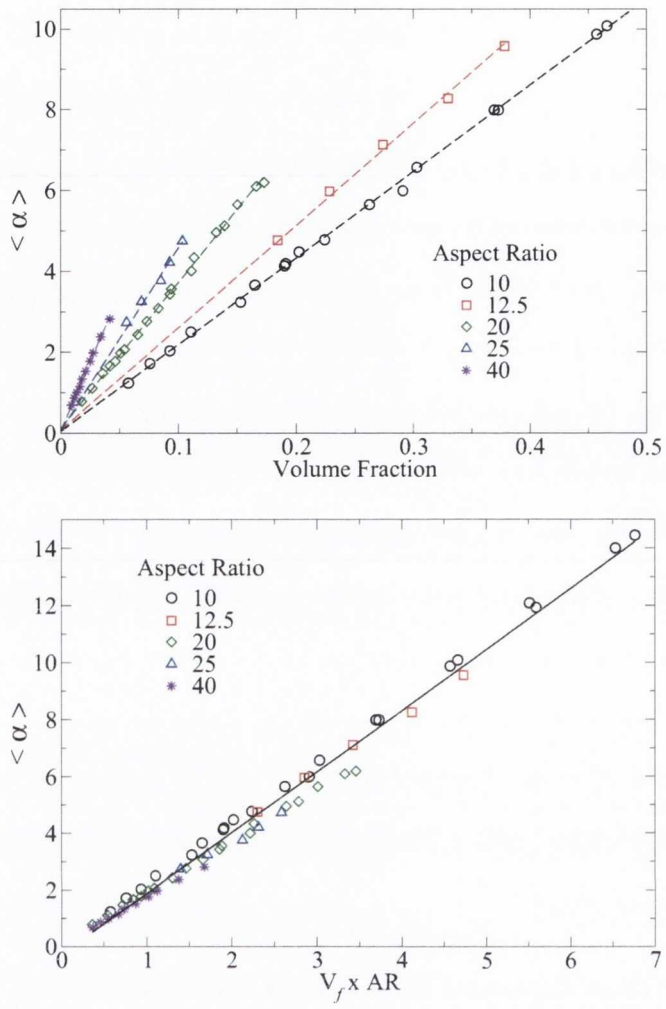

Figure 3.5: Top: Average network connectivity as a function of volume fraction. Bottom: Universal scaling of the connectivity with $V_f \times \ell/D$. Error bars are smaller than symbol sizes.

level.

We now proceed to analyse how the connectivity of the network depends on the concentration of rods. For a film of fixed dimensions, containing rods of identical aspect ratio, it is natural to expect that the average connectivity will increase with the volume fraction. There are more rods inside a finite volume, therefore more rods will be in contact. On the upper panel of figure 3.5 it is shown how the average connectivity per rod $\langle\alpha\rangle$, increases with the volume fraction V_f, for each aspect ratio considered. From the figure it is also clear that at a fixed volume

fraction, networks composed of higher aspect ratio rods have a higher connectivity. This is also in accordance with experimental observations that films made of high aspect ratio bundles have lower overall resistivity [84] due to a higher number of connections throughout the network. We return to this point in section 3.4, when we discuss the electrical conductivity of disordered resistive networks.

Based on a rod percolation model similar to the one considered here, a purely geometric argument has been used to propose that the mean number of junctions per nanotube (or bundle) is expected to behave as [121]

$$\langle \alpha \rangle = \beta \times V_f \frac{\langle \ell \rangle}{\langle D \rangle}, \tag{3.3}$$

where β is a constant independent of the nanotube (or bundle) diameter and length. Also, V_f is the volume of the film occupied by nanotubes, $\langle \ell \rangle$ is the average bundle length, and $\langle D \rangle$ is the average bundle diameter. In order to verify if our model satisfies this hypothesis, we plot the calculated average connectivity as a function of the scaled variable $V_f \times \ell/D$, in the bottom panel of figure 3.5. Remarkably, our results agree very well with the predicted relation, for all the aspect ratios considered. Besides providing a direct verification of equation (3.3), we extract from the linear least-square fit on the bottom panel of figure 3.5 the value of the constant $\beta = 2.14 \pm 0.03$, which is independent of the other factors in the equation.

From the average connectivity $\langle \alpha \rangle$, and the volume of a film it is possible to define the density of junctions by

$$N_J = \frac{\langle \alpha \rangle N}{2} \frac{1}{V}, \tag{3.4}$$

which is just the total number of connections in the network, divided by the total volume of the film. The factor of 2 in the equation accounts for double counting of connections. By using the calculated value of β it is possible to estimate the density of junctions of real films, which in turn provides valuable information

relating to electrical conductance in network films. This information can be used, for example, to predict the resistivity of films made with nanotubes provided by different commercial suppliers and different processing methods [76, 122]. We shall return to the relation between junction density and network conductance in section 3.4.

It is also instructive to analyse the probability distribution of connections per rod in the network. Figure 3.6 presents the distribution for the probability that an arbitrary rod will have α connections. The data is obtained by considering several random configurations with rods of aspect ratio $\ell/D = 10$. The vertical solid lines indicate the calculated average connectivity $\langle\alpha\rangle$ for each volume fraction specified. From the data it can be seen that the average number of connections per rod increases as the concentration of the network is increased, while the probability distribution becomes broader. The broadening of the distribution indicates that as the density of the networks increases, they actually become less homogeneous.

Another important factor to be extracted from our computer simulations is the number of elements connected to the electrodes. In figure 3.7 (upper panel) we show how the total number of rods crossing the electrode faces increases with the volume fraction of the film. Similar to the average connectivity of the network, the actual increase of $\langle\alpha_E\rangle$ with V_f depends on the aspect ratio of the rods, albeit in this case the dependence is more pronounced. In order to be of use when compared to experimental data, it is desirable to find a universal scaling dependence for $\langle\alpha_E\rangle$ in terms of the parameters V_f, ℓ and D, similar to the one in equation (3.3). Following an empirical approach, we find that the relation

$$\langle\alpha_E\rangle = \beta_E \times V_f \left(\frac{\ell}{D}\right)^2, \tag{3.5}$$

provides an excellent collapse of the data on a straight line, as shown on the bottom panel of figure 3.7. Moreover, the proportionality constant is found to be

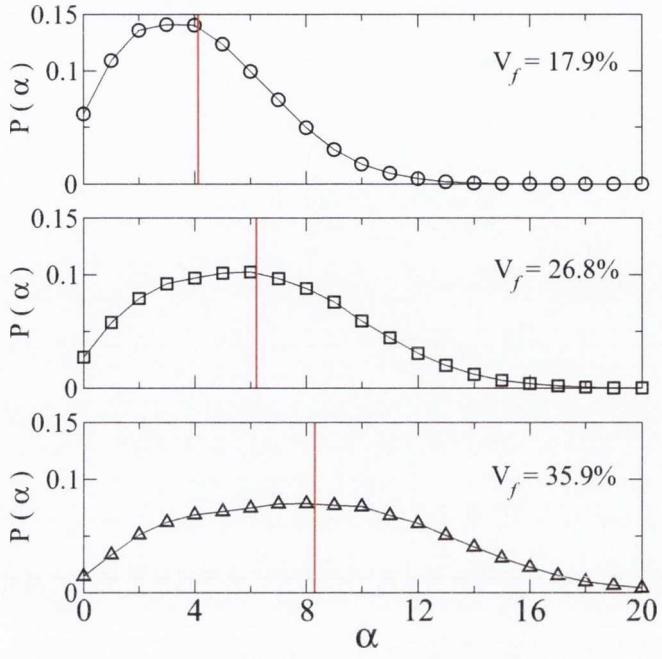

Figure 3.6: Connectivity probability distribution for random networks of finite rods with aspect ratio $\ell/D = 10$, and indicated volume fraction. Vertical solid lines indicate the calculated average connectivity. Each data point is an average over 100 independent configurations.

$\beta_E = 1.35 \pm 0.07$.

In practice, equations (3.3) and (3.5) can be used to provide numerical values for the connectivity of random networks of rigid rods, as well as the number of connections to electrodes, for any set of parameters chosen. The expressions provided for $\langle\alpha\rangle$ and $\langle\alpha_E\rangle$ can be used in combination with experimental data in order to estimate physical properties of real carbon nanotube films. For example, the density of junctions of a laboratory produced film can be estimated, providing valuable information about the inter-tube connections. Finally, equations (3.3) and (3.5) can also be coupled with electronic transport models to provide calculations for electrical resistance (or conductance) in random network films. In the next section we present a methodology to calculate the resistance of a network composed of Ohmic resistors. This methodology is later coupled with the results presented above, to provide calculations for the resistance of nanotube films from a purely

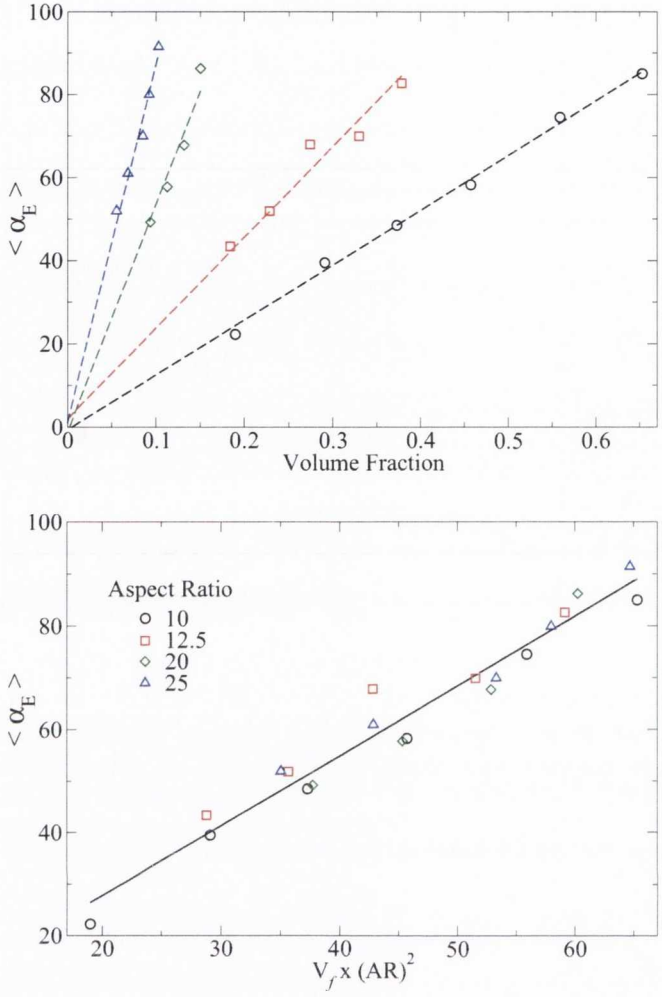

Figure 3.7: Top: Number of rods connected to electrodes as a function of the volume fraction. Bottom: Universal scaling of the electrodes connectivity with $V_f \times (\ell/D)^2$.

classical point of view in section 3.4. In chapter 4, the results presented in this section are coupled with a quantum transport model, providing a more realistic microscopic picture of electronic transport across nanotube network films.

3.3 Resistive Networks

In the particular case of films made of carbon nanotubes, the resistance of the nanotubes itself is negligible when compared to the resistance at the junctions. In this case, it is possible to model carbon nanotube films as networks of perfect

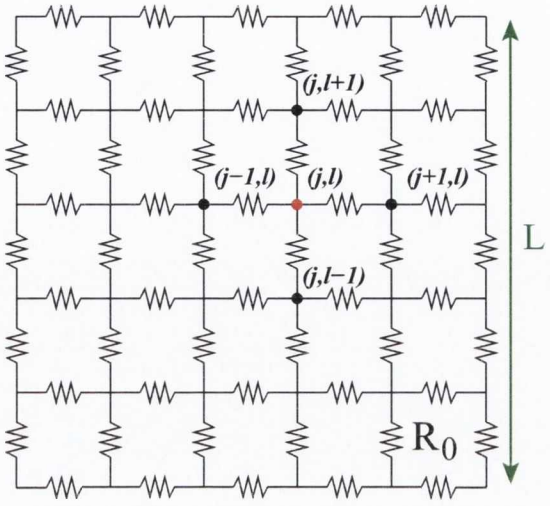

Figure 3.8: Schematic representation of a $L \times L$ square lattice with resistors R_0 between adjacent sites.

conductors connected by Ohmic resistors. Before considering truly disordered networks, it is instructive to start by studying the case of regular resistive networks. Although this is a much simpler system, it has some similarities with the case we are focused on. We begin this section by presenting two methodologies used to calculate the resistance between arbitrary nodes of regular resistive networks, i.e. regular lattices. We then introduce our own method, which has the advantage of being easily extendable to the study of non-regular (random) resistive networks.

Calculating the resistance between arbitrary nodes on a lattice of resistors has been a problem of scientific interest for several years [114, 115, 116, 123]. Consider for example a square resistive lattice as illustrated in figure 3.8, where each vertex contains a resistance R_0, and there is a total of $L \times L$ resistors in the lattice. What is the value of the equivalent electrical resistance between two arbitrary sites? Besides its applicability on the study of electrical resistance on conductive films, this problem also presents great potential as a teaching instrument with easy laboratory confirmation. Two independent approaches have been developed to tackle the problem in recent decades, and both can be applied to elucidate many features of this resistance problem.

The first approach, proposed by Venezian [117], introduced a method to calculate the resistance between two adjacent nodes on an infinite square grid of identical resistors. This method is based on a superposition of potentials and currents of two one-terminal configurations, in each of which a current from outside the lattice enters or exits through one single node. A few years later, Atkinson and van Steenwijk [118] generalised the original method to 3D and higher-dimensions, as well as other 2-dimensional lattices. Furthermore, these theoretical results were confirmed experimentally soon after by Denardo et al. [124], who explored the problem as an interesting laboratory demonstration.

The second independent approach has been developed by Cserti and collaborators, and relies on the application of lattice Green functions to calculate the equivalent resistance between arbitrary sites of a lattice [119, 125]. Lattice Green functions have been heavily studied by theoretical condensed matter physicists (see for example reference [89]), and the techniques developed by the community can be readily applied to this problem. Cserti derives an expression for the resistance between two arbitrary nodes of an infinite resistive lattice in terms of specific lattice Green function elements, which can in general be calculated analytically. Moreover, Cserti et al extend this methodology to account for perturbations in the networks, such as the removal of one or more resistors. In this case, the resistance between nodes is calculated from a perturbed Green function, obtained by the so-called Dyson's equation [125], which was introduced in chapter 2.

Both of the methods mentioned above provide analytic expressions for the total resistance between arbitrary nodes on 2D, 3D and higher-dimensional infinite regular lattices. In particular, the asymptotic behaviour of the equivalent resistance between two nodes as the distance becomes large was calculated independently by Venezian and Cserti, and can be expressed as

$$R(d) = \frac{R_0}{\pi}\left[\frac{\ln(8)}{2} + \gamma + \ln(d)\right], \tag{3.6}$$

where the distance d is large enough, and $\gamma \approx 0.5722$ is the Euler-Mascheroni constant (not to be confused with the electronic hopping parameters in chapter 4). This result implies a logarithmic divergence for the resistance between distant sites on an infinite square lattice of resistors.

Building on the methodology developed by Cserti, we propose yet another approach to this problem, specifically aimed at dealing with finite networks of resistors. Our methodology consists on the direct application of Ohm's law as well as Kirchoff's circuit laws to finite resistive networks. Similar do Venezian's construction, a current can be injected in an arbitrary node and extracted from another arbitrary site. The resistance between these arbitrary sites can then be calculated from the usual circuit laws. An equivalent approach to the one proposed here has been independently developed by Li and Chou [126] for the identification of backbones in standard percolation theory applications [1].

Considering the network represented on figure 3.8, the current that can be extracted from a site denoted by indices (j, l) is given by the net current from its nearest neighbours, which can be written as

$$I_{j,l} = \frac{1}{R_0}\left[(V_{j,l} - V_{j+1,l}) + (V_{j,l} - V_{j-1,l}) + (V_{j,l} - V_{j,l+1}) + (V_{j,l} - V_{j,l-1})\right], \quad (3.7)$$

$$I_{j,l} = \frac{1}{R_0}\left[4V_{j,l} - V_{j+1,l} - V_{j-1,l} - V_{j,l+1} - V_{j,l-1}\right], \quad (3.8)$$

where $V_{j,l}$ is the electrical potential on site (j, l). In order to keep the notation as light as possible, we introduce collective site indices which allow us to rewrite equation (3.8) as

$$I_A = \frac{1}{R_0}\left[\alpha_A V_A - \sum_{\delta}^{\alpha_A} V_{A+\delta}\right], \quad (3.9)$$

where δ represents the nearest neighbours of site A, and α_A is the total number of

[1] This work was brought to my attention by Prof. Alain Rochefort, during the *viva voice* examination.

neighbours. In matrix notation, it can be written in a compact form as

$$\mathbf{I} = \frac{1}{R_0}\mathbf{M}\mathbf{V}. \tag{3.10}$$

Only two elements of $\mathbf{I}$ are non-zero, the ones corresponding to the injection and extraction of current, being one positive and one negative. The matrix denoted by $\mathbf{M}$ has the general form

$$\mathbf{M} = \begin{pmatrix} \alpha_1 & -1 & 0 & 0 & \cdots \\ -1 & \alpha_2 & -1 & 0 & \cdots \\ 0 & -1 & \alpha_3 & -1 & \cdots \\ \vdots & \vdots & \vdots & \vdots & \ddots \end{pmatrix}, \tag{3.11}$$

where α_A is again the number of nearest neighbours of site A, and $M_{A,B} = -1$ if A and B are neighbours or zero otherwise. Notice that for a true finite lattice, boundary sites will have less connections than bulk sites. Moreover, with this approach it is also possible to consider perturbed networks, from which one or more resistors could have been removed, without having to apply Dyson's equation [125].

At this point, we can invert the matrix equation (3.10) to read

$$\mathbf{V} = R_0\mathbf{M}^{-1}\mathbf{I}. \tag{3.12}$$

By performing the calculation above, we obtain the value of the electrostatic potential in each and every node of the network. Moreover, from $\mathbf{V}$ we can calculate the potential difference across every resistor in the network, which provides a direct way of calculating the equivalent resistance between any two arbitrary points of the network. Furthermore, by constructing the appropriate matrix $\mathbf{M}$, it is possible to calculate the resistance between arbitrary nodes of any resistive structure,

including perturbed regular lattices and complex networks. All that is required is to describe the matrix $\mathbf{M}$ according to the specific network connectivity.

To calculate the resistance between two arbitrary sites A and B, we take

$$R_{A,B} = \frac{V_A - V_B}{I}. \tag{3.13}$$

Which can finally be expressed in terms of specific elements of the inverse of $\mathbf{M}$ as

$$R_{A,B} = R_0 \left([M^{-1}]_{A,A} + [M^{-1}]_{B,B} - [M^{-1}]_{A,B} - [M^{-1}]_{B,A} \right). \tag{3.14}$$

In this way we can calculate the resistance between two arbitrary points in any type of lattice, as long as we know the number of connections, and which sites are interconnected. It is not hard to generalise this result for the case where the resistance between nearest neighbours is not the same, or even for a distribution of different resistances. In order to do so, the $\frac{1}{R_0}$ term in equation (3.7) would have to be replaced by the specific resistance connecting the corresponding sites, and could be absorbed into the definition of $\mathbf{M}$.

We now proceed to show the application of the method for two simple cases. First, we calculate the resistance between sites along specific directions of a 2D square lattice as a function of the distance between the sites. In the sequence, we introduce a simple generalisation of the method described above in order to allow for multiple entry or exit points for the electrical current, and calculate the resistance between a group of sites and a single site. Finally, in the following section we couple this generalised methodology with the results of the previous section, and calculate the conductivity of stick percolation networks.

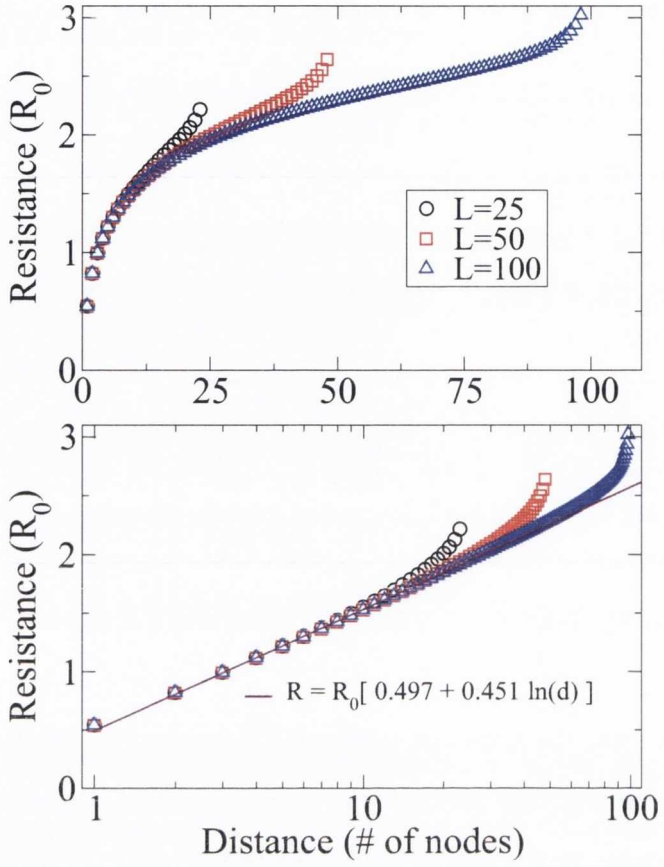

Figure 3.9: (Top) Resistance as function of distance between sites on a square resistive lattice. (Bottom) Resistance diverges logarithmically with the distance.

3.3.1 Results

On the upper panel of figure 3.9, we present the calculated equivalent resistance between two nodes on a square lattice network. The figure shows the dependence of the resistance as a function of the distance along a straight line, for square resistive lattices of dimensions $L = 25, 50$ and 100. For adjacent sites, where the distance $d = 1$, we recover the usual result of $\approx R_0/2$ [117, 119]. As the site from which the current is extracted approaches the borders of the lattice, finite size effects get more pronounced and we see an increase in the resistance. The logarithmic divergence of the resistance is clear from the bottom panel of the figure. In this case, the

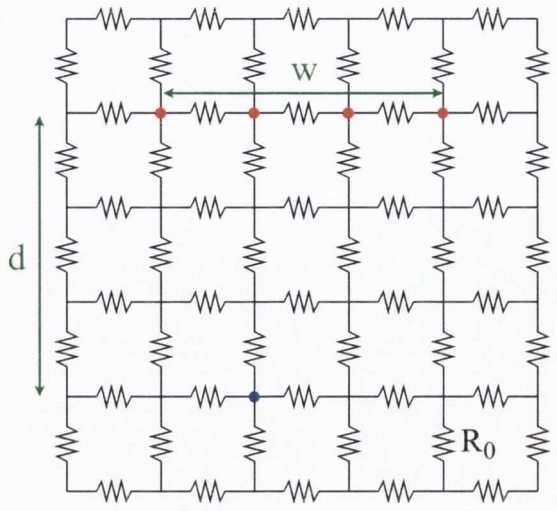

Figure 3.10: Schematic representation of a resistive lattice with multiple current injection points (red). Resistance is calculated between electrode and single extraction node (blue).

asymptotic limit for the resistance extracted from our calculations is found to be

$$R(d) = R_0 \left[0.497 + 0.451 \ln(d)\right]. \tag{3.15}$$

In spite of the finiteness of the networks considered, our method recovers the logarithmic divergence of the resistance as the distance between the insertion and extraction nodes gets large.

Our framework can be easily generalised to the case where there are multiple injection and/or extraction points for the electrical current. In this case, the current has to be divided among the injection/extraction sites, such that the total current injected equals the extracted current. For example, if a current I is injected in 10 sites, then each injection node receives a current $I/10$, and the total extracted current is I. Figure 3.10 illustrates a square lattice with $L \times L$ nodes, where the injected current is equally divided among w sites and extracted from a single site a distance d from the injection point. The distance d is defined as the perpendicular distance from the line of injection nodes to the extraction node, as indicated in figure 3.10. We investigate this particular arrangement, with view of considering

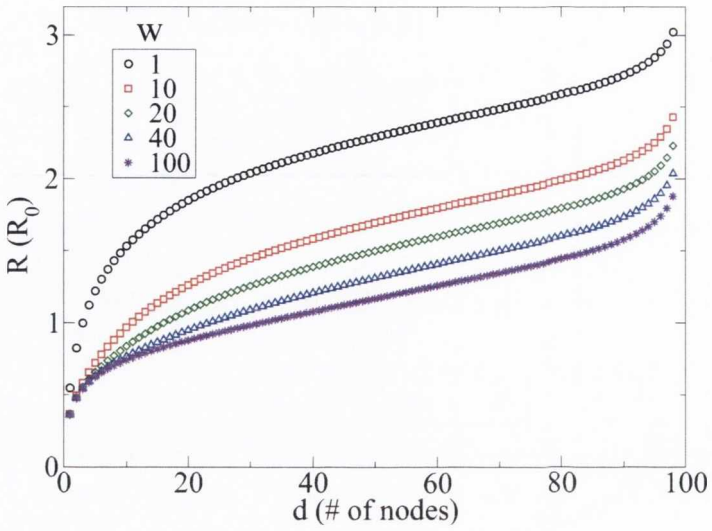

Figure 3.11: Resistance as a function of distance between sites on a square resistive lattice with multiple current injection points. The resistance is calculated between the multiple injection nodes and the single extraction point.

the presence of an electrode on the network. In the case illustrated, the equivalent resistance calculated is between the electrode and the single extraction node. Figure 3.11 shows the resistance between a group of w nodes forming an electrode and a single node located a distance d apart. It is observed that the resistance still increases with the distance approximately logarithmically. The data shows that the wider the electrode, the lower the resistance, with a minimum when the electrode spans the whole side of the lattice, i.e. $w = L$. This is not surprising because there are more paths between the injection and extraction points in this case, which will inevitably lower the equivalent resistance.

Finally, in the following section we proceed to present results for the resistance of complex resistive networks, obtained by combining the methodology described above, with the geometric modelling introduced in section 3.2.

3.4 Resistive Complex Networks

In this section, we finally return to our main objective, presented at the beginning of this chapter: to calculate the conductance across a disordered network of carbon nanotubes. Our methodology is based on the stick percolation model of section 3.2 in conjunction with the tools developed for the calculation of equivalent resistance between arbitrary nodes of a resistive network, presented in section 3.3.

In almost all situations of practical interest, with view of applications in electronic devices, nanotube films are produced such that the intrinsic resistance of CNTs is negligible when compared to the resistance of the inter-tube junctions. In this situation, the network of nanotubes in the film behaves very much like a network of Ohmic resistors, such as the ones introduced in the previous section. However, in a CNT film there is no ordered arrangement of sites, i.e., the networks formed by nanotubes are completely random and present an extremely complex topological structure. The traditional methods developed by Venezian [117] and Cserti [119] for calculating the resistance between arbitrary sites of a resistive network, are very successful in dealing with a plethora of regular networks but lack the flexibility to handle complex disordered structures such as the ones present on nanotube network films. This limitation has led us to develop a methodology analogous to the traditional ones, which is suited to tackle random networks, as well as regular arrangements of resistors.

In what follows we proceed to merge the results presented in the two previous sections. First, a random array of nanotubes (represented by finite-length rigid rods) is generated inside a containing box of specified dimensions. Then the volumetric fraction of the box occupied by rods is calculated. The junctions between rods in close proximity are mapped, and a list of neighbours of each rod is constructed. Similarly, rods that cross the electrode faces are identified, and that specific electrode is added to the list of neighbours. The inter-tube junction resis-

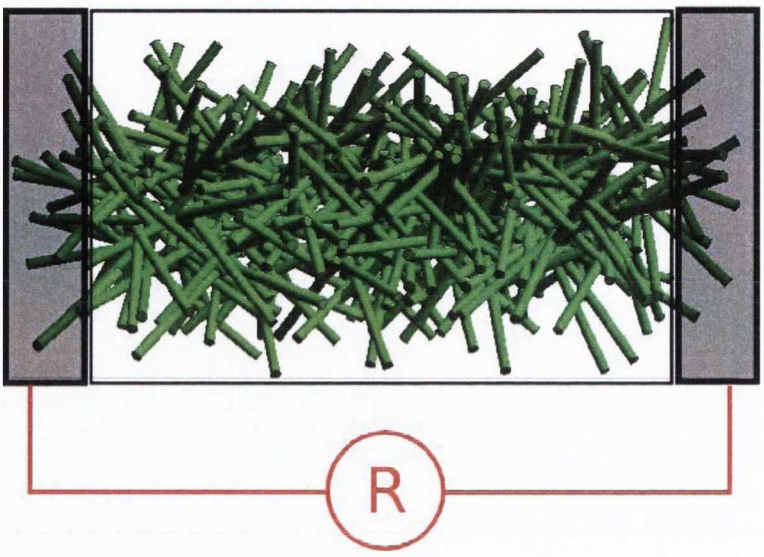

Figure 3.12: Schematic representation of the model used to calculate the resistance of carbon nanotube network films. Individual CNTs and bundles are represented by rods of finite length. Ohmic resistors R_0 are place at each nanotube junction. Total resistance across the film is calculated as the resistance between electrodes (shaded lateral rectangles).

tance experienced by conduction electrons are represented by Ohmic resistors (R_0) placed between every two rods in contact. Finally, the total resistance between the electrodes is calculated, and for the purpose of analysis, it is converted into conductance by taking its inverse.

Figure 3.12 illustrates in a schematic way the set up used in our calculations. Keeping in mind the practical motivations of our model, we analyse conductance results in terms of experimentally accessible quantities, such as the volume fraction of the networks, the density of junctions in the films, and the aspect ratio of the rods. In this case, the aspect ratio is an approximation to the ratio between average length and average diameter of carbon nanotube bundles, which can be obtained from microscopic analysis.

The calculation procedure is as follow:

1. Select N, ℓ and D;
2. Generate a random configuration of rods;
3. Construct matrix $\mathbf{M}$, and calculate $\mathbf{V}$ following description of section 3.3;

4. Calculate resistance between electrodes;
5. Repeat for several configurations and average results.

As previously mentioned, nanotube films are commonly produced from filtration of solutions containing dispersed CNTs. The disordered network is formed on the surface of the filter, and its density (and volume fraction) is directly proportional to the volume of solution filtered. For a fixed volume, a solution with low concentration of nanotubes will produce networks with small volume fraction, and a sparse structure. In this low concentration circumstances, there will be few percolating paths for the charge to move from one electrode to the other. In this case, films with high resistivity will be produced. On the other hand, if one starts with solutions presenting a high concentration of carbon nanotubes, it is expected that the films produced will have a low overall resistance, since there will be several percolating paths for the conduction electrons to move across the network.

It is more convenient to express the charge transport results in terms of the inverse resistance, i.e. conductance, defined simply as $\Gamma = 1/R$. Percolation theory predicts that for small values of V_f, the conductance behaves approximately as

$$\Gamma \sim (V_f - V_c)^t, \tag{3.16}$$

where V_c is the critical value of the volume fraction. The critical exponent t, depends only on the dimensionality of the embedding space. In our model the rods are randomly oriented in a 3D space, and for this case, the theory predicts $t = 1.94$ [127]. Beyond the percolation threshold, i.e. for networks with a volume fraction considerably larger than the critical value V_c, the conductance is found to increase linearly with V_f [128, 129].

Figure 3.13 shows how the network conductance increases with the volume fraction of the film, for three different values of aspect ratio of the rods. From the data it can be seen that for small values of V_f the conductance is very small or even

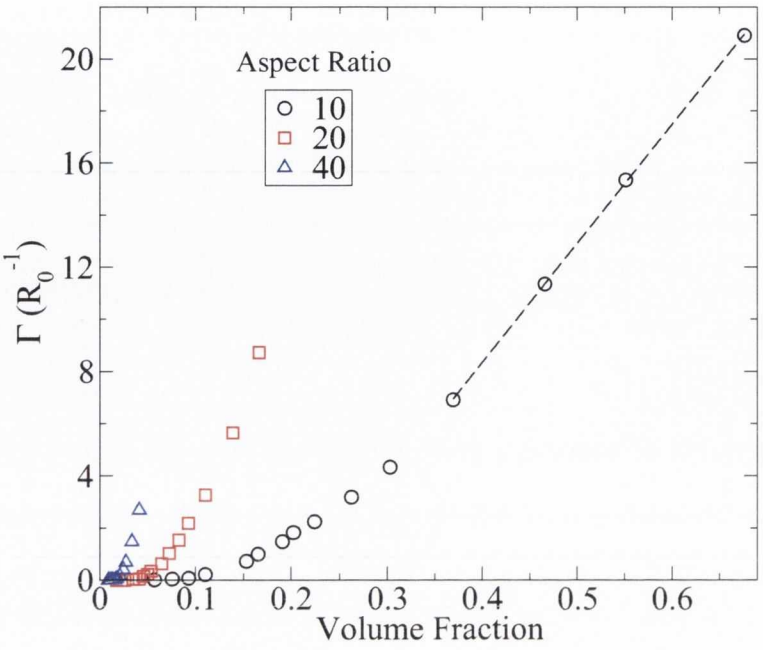

Figure 3.13: Inverse network resistance as a function of volume fraction. Simulating dense networks with high aspect ratio rods is too computationally demanding, but for small ℓ/D it is possible to achieve the linear dependence region. Dashed line is a linear fit to data.

vanishing, in perfect agreement with theoretical predictions. Simulating networks of large volume fraction for rods with high aspect ratio is very computationally demanding, and this issue has somewhat limited us in our calculations. However, it is possible to observe a crossover of the conductance from the percolation transition into a linear regime, as expected for dense networks. Besides being in accordance with theoretical predictions, our simulation results present a remarkable qualitative agreement with experimental measurements reported by Hu et al [77], reproduced here in figure 3.14.

The behaviour of Γ in the percolation region can be analysed in more detail in order to verify the agreement with the standard theory. In figure 3.15, we fit equation (3.16) with the expected scaling exponent $t = 1.94$, to our data near the percolation region. The agreement with theory is remarkable, and from the fit we also extract the value of the critical volume fraction for each aspect ratio considered. The calculated values of V_c are inversely proportional to ℓ/D, which

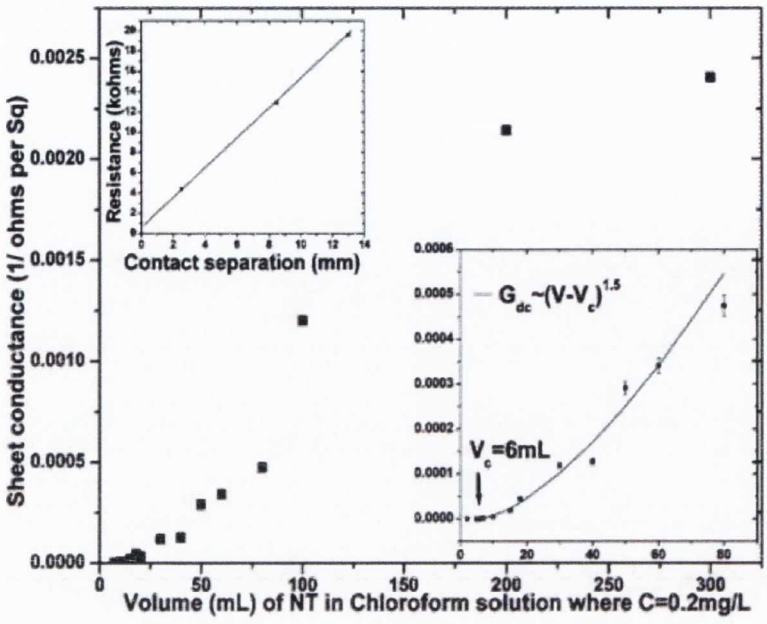

Figure 3.14: Conductance versus volume of CNT solution. Inset shows the power law fit in the percolation region, with a critical exponent $t = 1.5$. Figure reproduced from Hu et al. [77].

is an intuitive result and is also in agreement with previous theoretical predictions [128, 130, 131].

In section 3.2 we have shown how the connectivity of a random network of rods scales linearly with the product of the volume fraction with the aspect ratio of the individual rods. It is natural to expect the conductivity of the network to increase with its connectivity, which is indirectly demonstrated by the dependence of the conductance with the volume fraction (see figure 3.13). Moreover, it is also possible to analyse the dependence of the film conductance with the density of junctions, which has been defined in terms of the network connectivity as

$$N_J = \frac{\langle \alpha \rangle N}{2} \frac{1}{V}, \tag{3.17}$$

where N is the total number of rods inside the box of volume V. On figure 3.16 we plot the conductance as a function of $\langle \alpha \rangle N = 2N_J V$ on a log-log scale, and on a linear scale on the inset, for three different aspect ratios. Once again our

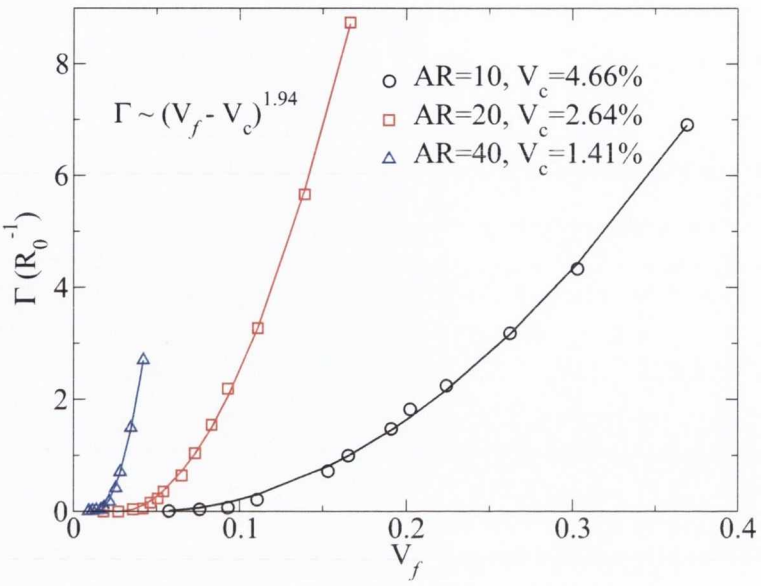

Figure 3.15: Network conductance as a function of the volume fraction near the percolation region. Solid lines are a fit of equation (3.16) with the appropriate 3D exponent $t = 1.94$.

calculations are limited by the computational resources required for simulations with the rods of large aspect ratio. However, it is possible to infer from the log-log plot that, at least for high enough concentrations of junctions, the conductance seem to converge to the linear dependence represented by the dashed straight line. Furthermore, in the inset we show the excellent collapse of all the data to the same straight line in a linear scale $\Gamma/R_0^{-1} = m \times 2N_J V$. In both scales used in figure 3.16, the dashed line has a slope $m \approx 8 \times 10^{-4}$.

We now turn to experiments, and combine our simulation results with laboratory measurements in order to estimate the actual value of the inter-tube resistance R_0. In figure 3.17 we present the conductivity of nanotube films versus the junction density on a log-log scale, as obtained by our collaborators at Prof. J.N. Coleman's group in TCD. Different symbols correspond to films prepared with different types of commercially available carbon nanotubes, as well as different solvents for the preparation of CNT solutions. Motivated by the linear dependence shown in the simulation results of figure 3.16, the dashed lines represent tentative linear least-

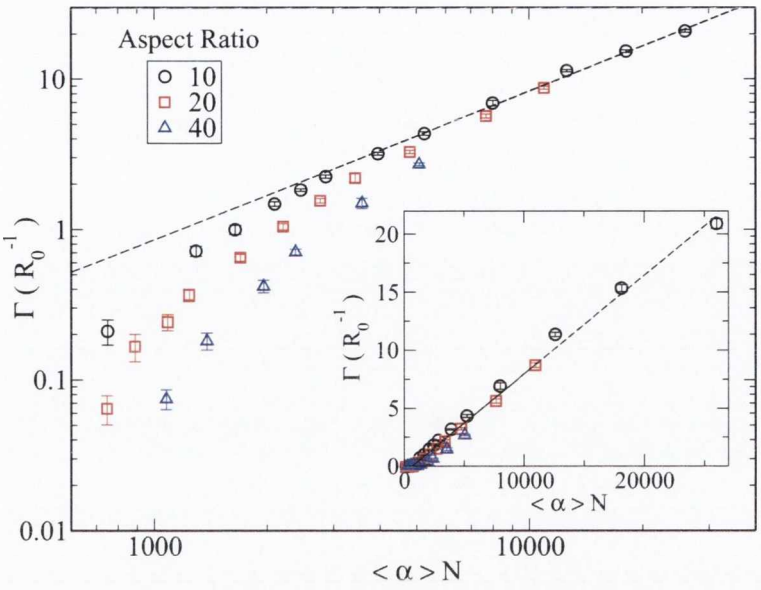

Figure 3.16: Film conductance increases linearly with density of connections for large enough densities. Log-log plot shows convergence to linear regime.

square fits to the data. Let us concentrate on the most conductive films, which seem to satisfy $\sigma = 4 \times 10^{-19} N_J$.

Using the information about the geometry of the box representing the film in the simulations, we can transform the calculated conductance into film conductivity, in order to estimate the average value for the junction resistance R_0. We begin with the linear relation derived from the simulation data, which can be written as

$$\Gamma = m \times \frac{2N_J V}{R_0}. \tag{3.18}$$

The simulated films have a volume $V = 2\ell \times 2\ell \times 4\ell = 16\ell^3$, thus

$$\Gamma = m \times \frac{32\ell^3 N_J}{R_0}. \tag{3.19}$$

The relation between conductance and conductivity is given by

$$\sigma = \Gamma \frac{L}{A}, \tag{3.20}$$

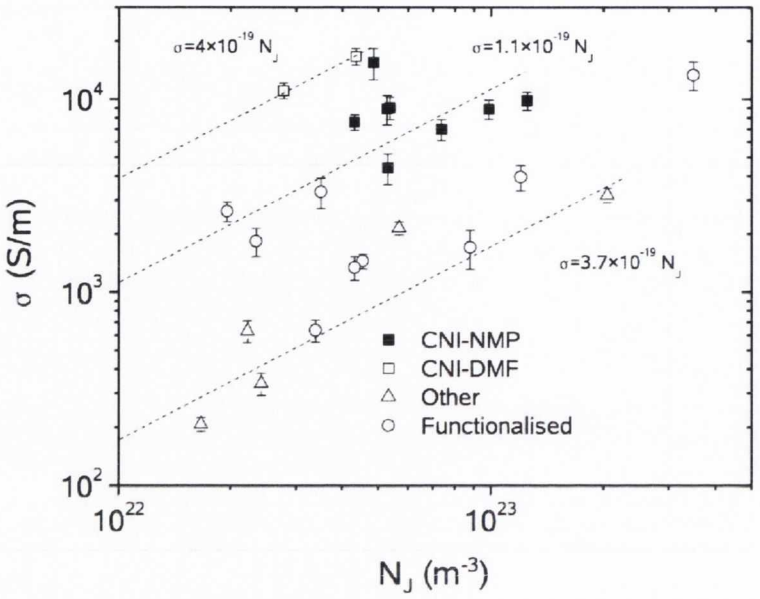

Figure 3.17: Approximate scaling of conductivity with density of inter-nanotube junctions. Dashed lines illustrate tentative linear fits to the different data sets as indicated by the equations. Legends label the respective supplier of nanotubes and the solvents used on the preparation of the films.

where $L = 4\ell$ is the length of the device and $A = 4\ell^2$ is the cross sectional area. Replacing this information in the above equation we end up with

$$\sigma = m \times \frac{32\ell^2 N_J}{R_0}. \tag{3.21}$$

Finally, we can write

$$R_0 = m \times \frac{32\ell^2 N_J}{\sigma}, \tag{3.22}$$

and replacing $m = 8 \times 10^{-4}$ and $\sigma = 4 \times 10^{-19} N_J$, results in

$$R_0 = 64 \times 10^{15} \ell^2 \quad (\text{in } \Omega/\text{m}^2). \tag{3.23}$$

A microscopic analysis of the CNI-DMF films estimate the average bundle length to be ~ 1 μm. Replacing $\ell = 1$ μm and $\ell = 10$ μm in the above expression for

the inter-bundle resistance results in $R_0 = 64$ KΩ and $R_0 = 6400$ KΩ respectively. This result is in good agreement with experimental measurements available in the literature. For example, Fuhrer et al. measured the resistance on single junctions of carbon nanotubes, considering metallic and semiconducting nanotubes [73]. The resistance at a junction between two metallic nanotubes was measured to be in the range 100 KΩ $\leq R_{MM} \leq$ 300 KΩ, whereas the junction resistance between two semiconducting nanotubes was measured in the range 430 KΩ $\leq R_{SS} \leq$ 2300 KΩ. Recent results from Nirmalraj et al. have found that the average junction resistance depends considerably on the diameter of the nanotubes and bundles in the junction, and can vary widely depending on the chirality of the nanotubes involved as well as the diameter of the bundles [76]. Nonetheless, junction resistances in the range 98 KΩ $\leq R_J \leq$ 2700 KΩ have been measured in thin films made of pristine CNTs.

It is important to point out that if one were in possession of reliable values for the junction resistance in terms of the tubes type these values could be easily incorporated into our proposed model. By including the actual value of the junction resistance between two metallic tubes, two semiconducting tubes, and a metallic and a semiconducting tube, into our model it should be possible to obtain predictive results. Furthermore, taking into consideration that one third of CNTs are metallic, it is straightforward to generate networks with a distribution of CNT junctions which corresponds to the ones found in real films. The calculated conductance of these model networks should be quantitatively comparable to experimental values. Unfortunately, an exact determination of these contact resistances by experimental methods is still an open problem.

3.5 Chapter Summary

In this chapter we have shown how a relatively simple procedure can be applied to model the complex features present in the morphological structure of carbon

nanotube network films. Individual nanotubes and bundles are mimicked by rigid rods of finite length and diameter, while the film is represented by a rectangular box of dimensions defined in terms of nanotube length.

The volumetric fraction of the film occupied by rods was found to be linearly dependent on the number of rigid rods in the network. The average number of connections per rod in a random network was found to scale universally with a combined variable given by the product of the volume fraction with the aspect ratio of the individual rods considered. Similarly, the number of rods connected to electrodes placed in opposing faces of the film was found to scale with the volume fraction times the square of the aspect ratio.

We have also presented a method, based on previously developed methodologies, to calculate the equivalent resistance between arbitrary points on a network of resistors. We have shown how the resistance between two nodes of a network increases with the logarithm of the distance between them, in agreement with analytic results.

Finally, we have combined the rigid rods percolation model with resistance calculations in order to obtain the conductance of model carbon nanotube network films. We have shown how our results are in perfect agreement with standard percolation theory, and how the conductance of nanotube films is affected by the morphology of the networks. Direct comparison of simulation results with experimental measurements are found to be in good agreement, and provide estimates for the junction resistance in real carbon nanotube films. These estimates are compatible with independent measurements reported in the literature.

The results presented in this chapter have been published in Reference [122].

Chapter 4

Microscopic Modelling of Carbon Nanotube Networks

4.1 Introduction

Individual carbon nanotubes (CNTs) present outstanding physical qualities such as remarkable mechanical strength, unique electronic structure, and ballistic charge transport [88]. With so many outstanding features it is not surprising that nanotubes are being mixed with other materials in order to improve some of their physical properties. Carbon nanotube–polymer composites have been investigated due to their promising applications in mechanical reinforcement of materials and on the production of conductive transparent electrodes [26, 29]. As a matter of fact, carbon nanotube network films have been attracting much attention from the scientific community thanks to their applicability in a range of future electronic devices [84]. Applications of CNT thin films include flexible transistors [34, 37, 38, 43, 45, 111, 132], transparent electrodes [80, 111, 133], and even loudspeakers [134]. CNT thin film transistors can be used in the development of novel chemical and biological sensors [9, 135, 136, 137, 138]. Transparent electrodes made of CNT thin films can be applied to the production of solar cells [133, 139]

and flexible electronic displays [43, 80, 140, 141]. In other recent reports, silver nanowires (NWs) [82] and graphene [55, 142] have been proposed as base materials for the production of transparent, flexible, and conductive thin film electrodes. Flexibility is a natural quality of carbon nanotubes and graphene, as well as of noble metal nanowires, which naturally extends to thin films produced with them.

The transparency of a thin film is intrinsically connected to its conductance. In particular, the relationship between optical transparency T and electrical resistance R of a thin metallic film (suspended in air) is approximately described by [81]

$$T = \left[1 + \frac{1}{2R}\sqrt{\frac{\mu_0}{\epsilon_0}}\frac{\sigma_{op}}{\sigma_{dc}}\right]^{-2}, \tag{4.1}$$

where μ_0 and ϵ_0 are the permeability and permittivity of vacuum, respectively; σ_{op} is the optical conductivity of the film, and σ_{dc} its electrical conductivity. Equation (4.1) is only valid when the absorption of the material is much smaller than its reflectance, and when the film thickness is much less than the wavelength of interest. In general, CNT films as well as nanowire films satisfy these conditions. For applications in flexible displays and transparent electrodes, a high transparency in the visible spectrum (usually measured at a wavelength of 550 nm) must be coupled with low film resistance. From the equation above, it is possible to evaluate that this condition may be satisfied if the electrical conductivity is much larger than the optical conductivity, such that the ratio σ_{op}/σ_{dc} is small.

The optical conductivity depends on the chirality of individual nanotubes, and cannot be precisely controlled on CNT films. However, due to the mixture of different types of nanotubes in a network film, σ_{op} is generally found to be approximately constant across a variety of nanotube films [84]. On the other hand, the electrical conductivity σ_{dc}, depends on a number of factors including the degree of purity of the nanotubes, the doping level, as well as the average bundle length and diameter. A number of strategies have been developed to control these fac-

(a) 

(b) 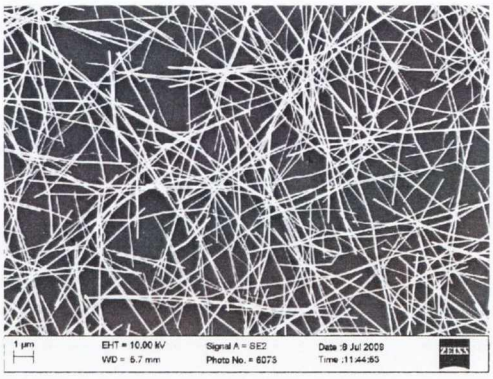

Figure 4.1: Scanning Electron Microscopy image of disordered complex networks on a) Carbon nanotube film, and b) Silver nanowire film. Images courtesy of J.N. Coleman's group, Trinity College Dublin.

tors, and attempting to increase σ_{dc} is the most accessible way of controlling the performance of conductive films.

As we have already discussed in previous chapters, the electronic transport in disordered network films takes place through electronic tunnelling across the entire film. Figure 4.1 displays microscopy images of a typical CNT film (a), and a Silver NW film (b). Among all the factors controlling the conductivity of thin films, the resistance at tunnel junctions between individual components of the network plays a dominant role. Recent studies have reported enhancements in the film conductivity as a result of improvements in the inter-tube contacts by means of chemical treatments [76, 86]. However, the highest electrical conductivities reported so far seem to be on the lower limit of the values needed for application on flexible displays, namely $\sigma_{dc} \approx 6 \times 10^5$ S/m [55, 56, 122]. Moreover, it is not clear if CNT films can indeed provide the electrical conductivities required. In particular, the structure of the networks formed in the films might play a role in limiting the electronic conductivity of CNT films. This means that no matter how much progress is made in lowering the junction resistance, there should be a maximum value for the conductivity, which is regulated by the network topology. To find this maximum value is our main goal in this chapter.

In chapter 3 we have shown how the morphology of the disordered CNT networks affects the electronic transport properties of the resulting films. In the present chapter we combine the macroscopic properties of CNT networks with an atomistic description of carbon nanotubes based on quantum electronic structure methods. We apply the resulting multiscale model to estimate an upper limit for the electrical conductivity of CNT films. In order to do so, we shall focus on ballistic electronic transport and disregard any source of decoherence that may affect the charge carriers.

The sequence adopted in this chapter is as follows. In section 4.2 we describe our theoretical approach to model the electronic structure of individual carbon nanotubes and idealised nanowires. We apply a general methodology based on semi-empirical tight binding Hamiltonians and the respective single particle Green functions, introduced in chapter 2. The choice of computationally inexpensive electronic structure method allows us to treat heavily disordered environments such as network films. Moreover, because our methodology is based on Green functions, it is easily transferable to account for networks made of CNTs, NWs and possibly graphene. In section 4.3 we show how the Kubo formula for electronic conductance can be applied to disordered networks. In the same section, we also argue how the network Green function can be described in a computationally efficient manner, which allows for the treatment of films with thousands of individual components. We begin section 4.4 by applying our computationally efficient methodology to calculate the conductance of random networks of idealised monatomic wires. These basic results are used to analyse the general features of the model. In the sequence, the multiscale methodology is applied to the specific case of carbon nanotube networks. We argue how the ensuing results can be used to estimate a limiting value for the conductivity of CNT networks in terms of properties of the films such as volume fraction and average bundle length and diameter. In the conclusion of this chapter, we describe how a comparison of the experimentally measured conductiv-

ities with the corresponding theoretical upper value provides a reasonable estimate of how much room there is for improvement. Finally, we describe how this valuable piece of information has been used, for instance, to establish that the best measured values of conductivities for nanotube-based films are too close to the upper limit predicted, which suggests that further improvements in their transport properties are unlikely. Furthermore, this conclusion indicates that metallic nanowires other than CNTs are the most likely candidates to be used in flexible displays.

4.2 Model

From a theoretical perspective, the description of electronic transport on carbon nanotube films involves the flow of charge through a percolating network of finite-sized elements connected to source and drain electrodes (see figure 3.12). Computational studies of this problem tend to concentrate on analysing the system in two very different length scales. The first approach, presented in detail in chapter 3, analyses the system in a macroscopic scale. Individual CNTs are modelled as perfectly conducting rigid rods of finite length-to-diameter ratio. Tunnel barriers at nanotube junctions are mimicked by Ohmic resistors. The film resistance is calculated as the resistance between opposing electrodes separated by a disordered network of identical resistors. As we have shown, this method provides results in reasonably good agreement with experiments. However, it is enlightening to explicitly consider the influence of the electronic structure of individual nanotubes on the transport properties of CNT networks. In particular, this approach can be applied to obtain an estimate for the maximum conductivity of CNT films, which can clearly indicate if nanotube networks are indeed the appropriate choice for the development of flexible electronic displays.

It is also possible to approach electronic transport problems from an atomistic viewpoint, most notably by means of *ab-initio* density functional theory cal-

culations (DFT) coupled with non-equilibrium Green function methods [94, 95]. However, the computational cost of these calculations can be considerably high. Moreover, all current DFT implementations require at least some degree of periodicity in order to handle large systems ($\approx 10^3$ atoms), which unfortunately is clearly not present in disordered CNT networks. Nonetheless, *ab-initio* methods have been used to investigate electrical resistance at single wall nanotube (SWNT) junctions [75], and more recent studies have extended these results considering the presence of O_2 and N_2 molecules [143] near the junction. The use of first principles methods for obtaining the quantum conductance between individual nanotubes is able to shed some light on the quality of the junction, but it is unable to reproduce the general observed features in network films because it is not capable of including disorder effects to the scale required. The alternative of carrying out a fully atomistic transport calculation within a heavily disordered environment is very desirable but it is currently too computationally demanding. It is therefore necessary to compromise if one wishes to combine the two features.

One possible approach consists of using computationally inexpensive semi-empirical methods to describe the electronic structure of carbon nanotubes. Tight binding model Hamiltonians are a very efficient and convenient way to describe the electronic structure of materials. As we have seen in chapter 2, the tight binding approximation provides very good results for the electronic properties of CNTs. Moreover, it is possible to obtain system-specific parameters from high precision *ab-initio* calculations [144, 145]. By describing the electronic structure of individual nanotubes with a simplistic model Hamiltonian, we can afford to account for disorder effects by considering hundreds, if not thousands, of CNTs, and several possible configurations for the structure of the random tunnelling networks formed in the films. Furthermore, quantitative results for the conductance of CNT films can be obtained when a precise parametrisation of the hopping terms and on-site energies is obtained from first principle methods, as mentioned above.

4.2.1 Tight Binding Hamiltonian and Green Functions

In general, the electronic structure of an individual wire (carbon nanotube or nanowire) is described by a semi-empirical tight binding Hamiltonian of the form

$$\mathcal{H}_\delta = \sum_i |\delta, i\rangle \epsilon_0 \langle \delta, i| + \sum_{\langle i,j \rangle} |\delta, i\rangle \gamma_0 \langle \delta, j|, \tag{4.2}$$

where $|\delta, i\rangle$ represents an electron on atom i of a wire labelled by δ, ϵ_0 is the on-site energy, γ_0 is the hopping integral parameter, and the sum $\langle i, j \rangle$ is over nearest-neighbouring atoms. This general form can describe several types of nanostructures, depending on the choice of atomic structure and on the orbital degrees of freedom represented by the states $|i\rangle$. Moreover, as we have already shown, the tight binding approximation provides excellent results when used to describe the electronic structure of CNTs.

Associated with the Hamiltonian $\mathcal{H}_\delta$, there are the retarded(+) and advanced(−) single-particle Green functions, defined in chapter 2 as

$$\mathcal{G}^\pm = [E^\pm - \mathcal{H}_\delta]^{-1}, \tag{4.3}$$

where $E^\pm = E \pm \imath\eta$, with η being a small positive imaginary part added to the electron energy E in order to avoid singularities. The above are also known as bare or undressed Green functions, and are automatically defined by the choice of Hamiltonian.

When the wires considered are monatomic linear chains, it is possible to solve Equation (4.3) analytically, and write an explicit expression for individual elements of the Green function. In this case, the (i, j)-th matrix element of the GF of a finite monatomic chain with L atoms described by the Hamiltonian in Eq.(4.2) is given by [89]

$$\mathcal{G}^\pm_{ij}(E) = \frac{2}{L} \sum_{m=1}^{L} \frac{\sin(i\frac{m\pi}{L+1}) \sin(j\frac{m\pi}{L+1})}{E^\pm - \left[\epsilon_0 + 2\gamma_0 \cos(\frac{m\pi}{L+1})\right]}, \tag{4.4}$$

which can be used to calculate any matrix elements of the GF, as needed. Equation (4.4) becomes identical to the Green function of an infinite linear chain in the limit $L \to \infty$. Furthermore, it is also possible to write an analytical expression for the surface element of the GF for a semi-infinite monatomic chain, which is written as [146]

$$\mathcal{S}^{\pm}(E) = \frac{(E^{\pm} - \epsilon_0) \pm [(E^{\pm} - \epsilon_0)^2 - 4|\gamma_0|^2]^{1/2}}{2|\gamma_0|^2}, \tag{4.5}$$

It is worth mentioning that the use of semi-infinite linear chains will become clear shortly when we address the issue of wires contacted to electrodes. The above expressions provide a way to directly calculate any Green function matrix elements as needed, which is a huge computational advantage when compared to calculating the whole GF.

For the case of finite carbon nanotubes, however, matters are not as simple. Even though it is possible to write an analytical expression for the Green function's matrix elements of infinite and semi-infinite nanotubes [147, 148] (both armchair and zigzag), it is not straightforward to do so for finite nanotubes. Therefore, we rely on a direct calculation of the whole Green function using Equation (4.3). Notice that this requires the numerical inversion of matrices with dimensions equal to the number of atoms in the particular nanotube.

As we have described in chapter 2, electronic transport calculations typically require the presence of particle reservoirs, which represent source and drain for the conduction electrons. In the case of transport simulations of carbon nanotube networks, semi-infinite nanotubes are employed to mimic the presence of particle reservoirs. These semi-infinite CNTs are solely described by the GF elements relative to the atoms on its final unit cell. In order to calculate surface GF elements of semi-infinite nanotubes, we apply efficient recursion methods, which are numerically stable and computationally inexpensive.

4.2.2 Network Green Functions

Once we have introduced how we calculate the electronic structure of individual wires, we move on to describe the electronic properties of a disordered network of interconnected wires. Following the general method described in chapter 2, we divide our system in three parts: two leads and a central region. The major difference between our particular approach and the usual one is that each one of the three parts of the system are themselves composed of several wires. The leads are represented by a number of semi-infinite wires, which act as particle reservoirs. Meanwhile, the central region of the system consists of the disordered network itself, represented by an ensemble of finite-sized wires. We begin by constructing the Green function matrices of a completely disconnected system. The inter-wire junctions are introduced in the form of electronic hopping terms between wires in the network, and between the network and the electrodes. Finally, we use Dyson's equation to calculate the GF of a fully connected network of wires which represents the disordered films.

Beginning from a disconnected tripartite system, we can write the complete Green function as a super matrix of the form

$$g^{\pm} = \begin{pmatrix} g_L^{\pm} & 0 & 0 \\ 0 & g_C^{\pm} & 0 \\ 0 & 0 & g_R^{\pm} \end{pmatrix}, \tag{4.6}$$

where $g_{L,R}^{\pm}$ are the GF matrix of the left and right electrodes, and $g_C^{\pm}$ is the GF of the central scattering region. At this stage, the network is an ensemble of non-interacting wires.

In this initial description of the disconnected system, each of the matrices in $g^{\pm}$ are in block diagonal form, with one block for each individual wire. The electrodes act as charge reservoirs which will be here represented by semi-infinite nanowires.

In other words, whenever a wires is contacted to either electrode we will represent it by a semi-infinite object. Therefore, there are $\langle \alpha_E \rangle$ diagonal blocks given by surface Green function elements of semi-infinite monatomic chains or carbon nanotubes. In general, the electrode GFs can be written as

$$g^{\pm}_{L,R}(E) = \begin{pmatrix} \mathcal{S}^{\pm}(E) & 0 & 0 & \cdots \\ 0 & \mathcal{S}^{\pm}(E) & 0 & \cdots \\ 0 & 0 & \mathcal{S}^{\pm}(E) & \cdots \\ \vdots & \vdots & \vdots & \ddots \end{pmatrix}, \tag{4.7}$$

where $\mathcal{S}^{\pm}(E)$ are advanced (or retarded) Green functions of the surface elements of semi-infinite wires, which mimic the particle reservoirs.

Similarly, the GF of the central scattering region consisting of a disconnected network with N wires is represented by a block diagonal matrix with N blocks, and it is written as

$$g^{\pm}_{C}(E) = \begin{pmatrix} \mathcal{G}^{\pm}(E) & 0 & 0 & \cdots \\ 0 & \mathcal{G}^{\pm}(E) & 0 & \cdots \\ 0 & 0 & \mathcal{G}^{\pm}(E) & \cdots \\ \vdots & \vdots & \vdots & \ddots \end{pmatrix}, \tag{4.8}$$

where we recall that $\mathcal{G}^{\pm}(E)$ is the Green function of a finite-sized pristine monatomic linear chain or carbon nanotube. In general, each diagonal block $\mathcal{G}^{\pm}(E)$ is a matrix whose dimension equals the total number of atoms on the individual wires.

It is now simple to connect individual wires throughout the network by introducing a perturbing potential bridging any two wires that should be in contact. This inter-wire coupling appears in the form of an electronic hopping term γ' in the Hamiltonian of the complete system, and is given by

$$V_{\delta,\delta'} = |\delta, j\rangle \gamma' \langle \delta', j'|, \tag{4.9}$$

where δ and δ' label the connecting wires, and j and j' identify the atoms in each one. Notice that δ and δ' must be different while j and j' are allowed to have the same value. These individual hopping terms can be grouped together in the form of a general perturbation potential written as

$$V = \begin{pmatrix} 0 & V_{LC} & 0 \\ V_{LC}^{\dagger} & V_{CC} & V_{CR} \\ 0 & V_{CR}^{\dagger} & 0 \end{pmatrix}, \tag{4.10}$$

where once again each term represents a matrix itself.

On the construction of the perturbing potential we assume that semi-infinite wires in the same electrode do not interact with each other. Furthermore, we assume that the central scattering region is large enough, such that there can be no direct hopping terms between semi-infinite wires located on different electrodes. The first assumption can be easily relaxed, and it should not have any significant effects on the results. The second assumption, however, should not be relaxed. The physical meaning of the second constraint, i.e., $[V_{LR}] = [V_{RL}] = [0]$, is to avoid short circuits on the system, which could manifest as spuriously high values for the conductance, and significantly affect the results.

The term V_{CC} is by far the most significant one, and also the one that lies at the heart of our methodology. In our model, $[V_{CC}]$ is a matrix constructed from a random network, generated from an ensemble of nodes with a given average number of connections per node. Equivalently, a random graph can also be defined by its total number of sites N, and the total number of connections on the graph $\langle\alpha\rangle N/2$. The process to construct $[V_{CC}]$ is as follows:

1. Select two unconnected wires at random: δ, δ' ;
2. Select one random atom in each wire to carry on the interaction: j, j' ;
3. Make $\langle \delta, j | V_{CC} | \delta', j' \rangle = \gamma'$;
4. Repeat until total number of connections equals $\langle\alpha\rangle N/2$.

A similar procedure is also applied to construct $[V_{LC}]$ and $[V_{CR}]$, where the interaction of the electrodes with the finite-sized wires is chosen by a randomised process. The inter-wire hopping term, represented as γ' is defined in analogy with the usual tight binding hopping integral parameter γ_0, and roughly represents the coupling between individual atoms in interconnected wires.

Remember that Equations (4.7) and (4.8) describe the GF of the completely disconnected network. The Green function of the interconnected disordered systems can be calculated with Dyson's equation,

$$G^{\pm} = \left[\hat{1} - g^{\pm}V\right]^{-1} g^{\pm}, \tag{4.11}$$

and it can be written in matrix form as

$$G^{\pm} = \begin{pmatrix} G_L^{\pm} & G_{LC}^{\pm} & 0 \\ G_{CL}^{\pm} & G_C^{\pm} & G_{CR}^{\pm} \\ 0 & G_{RC}^{\pm} & G_R^{\pm} \end{pmatrix}. \tag{4.12}$$

We now have the Green function of the whole interconnected network, including left- and right-hand side electrodes, central scattering region, and propagators between these three regions. Therefore, $G^{\pm}$ provides all necessary information with respect to the electronic structure of the disordered network, be it formed by linear monatomic chains or carbon nanotubes, and can be used to calculate the electronic conductance of the system.

As shown in the next section, choosing to represent the Green function of the network in the above described manner simplifies the calculation of the conductance, which can be computed directly from specific GF elements by using the Kubo formula.

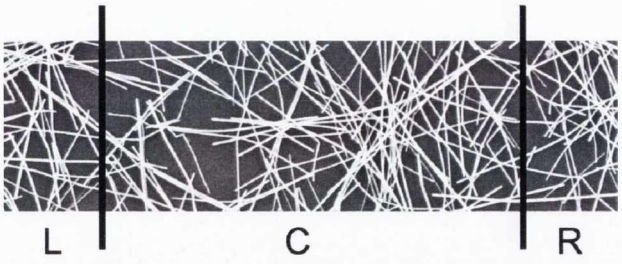

Figure 4.2: Schematic representation of the system, divided in left and right leads (L,R), and a central scattering region (C). The cleavage plane is placed between C and R.

4.3 Kubo Formula Applied to Networks

The zero-bias conductance of the system is calculated with the Kubo formula, introduced in chapter 2. The Kubo formalism provides a simple expression for the conductance by calculating the net electronic current across a reference plane in the system, often referred to as the cleavage plane, which is located between any two adjacent parts of the system. The current is expressed in terms of a few Green function matrix elements of the system, and the calculation becomes simple enough.

In analogy to the standard formalism first introduced by Caroli et al. [104], the system is divided in three parts. The location of the cleavage plane is arbitrary and can be chosen in the most convenient location for the case in question. Here it is placed between the central region and the right lead, as illustrated in Figure 4.2. Translating Figure 4.2 into words, regions L and R contain $\langle \alpha_E \rangle$ semi-infinite wires and region C contains a disordered array of N finite wires, forming a random network with an average number of connections per wire given by $\langle \alpha \rangle$. Having placed the cleavage plane between the regions C and R, the Kubo formula for the zero-bias conductance is written as [99, 149]

$$\Gamma(E_F) = \left(\frac{4e^2}{h}\right) \times \Re e \left\{ \mathrm{Tr} \left[\tilde{G}_C V_{CR} \tilde{G}_R V_{CR}^{\dagger} - V_{CR} \tilde{G}_{RC} V_{CR} \tilde{G}_{RC} \right] \right\}, \qquad (4.13)$$

where all the GFs are calculated at the Fermi energy E_F, and $\tilde{G}(E)$ are the causal GFs, defined as

$$\tilde{G}(E) = \frac{1}{2i}\left[G^{-}(E) - G^{+}(E)\right]. \tag{4.14}$$

4.3.1 Reducing Green Function Matrices

Even though it is possible to write an explicit expression for the Green function of the interconnected network as in equation (4.12), from which the matrix elements required by the Kubo formula in equation (4.13) can be obtained, it is an extremely challenging task. The difficulty arises from the size of the matrices involved. Consider for example, a network with $N = 100$ wires, where each wires has $L = 1000$ atoms. In this case, $g_C^{\pm}$ is a matrix of $(N \times L)^2 = 10^{10}$ elements, and $[V_{CC}]$ is a matrix of same dimension. Storing matrices of this size on the memory of computer clusters becomes a demanding computational task in itself, and inverting matrices of this dimension takes a considerable time, even if one applies advanced linear algebra routines. The solution to this conundrum presents itself in a most elegant way, and it relies on the fact that $g^{\pm}$ is block diagonal and that V is a sparse matrix. Therefore, the product $g^{\pm}V$ on Equation (4.11) is also sparse, or at least has many vanishing terms that will not affect $G^{\pm}$, i.e., several of the matrix elements in $G^{\pm}$ do not depend on the perturbation, whenever the corresponding element vanishes.

Let us consider an illustrative example, in which the matrix V_{CC} may look something like

$$V_{CC} = \begin{pmatrix} 0 & 0 & 0 & 0 & V_{1,5} \\ 0 & 0 & 0 & V_{2,4} & V_{2,5} \\ 0 & 0 & 0 & 0 & 0 \\ 0 & V_{4,2} & 0 & 0 & 0 \\ V_{5,1} & V_{5,2} & 0 & 0 & 0 \end{pmatrix}, \tag{4.15}$$

indicating that wire 1 has a single connection to wire 5; wire 2 is connected to wires 4 and 5; wire 4 is linked only with wire 2, and wire 5 is connected with wires 1 and 2. Note that in this pictorial representation wire 3 is not connected to any of its counterparts, a fact that fills the third row and third column of the matrix V with zero block matrices. In practical terms, the corresponding row/column in the matrix $G_C^{\pm}$ will not involve any V-dependent terms and is simply given by $\mathcal{G}^{\pm}$. It is easy to conclude that similar behaviour arises in terms of the intra-wire indices, that is, a connection between atom j of wire δ and atom j' of wire δ' will only involve the corresponding matrix elements of the g-matrix. Therefore, if a given NW is connected to three neighbours at intra-wire sites i, j and k, the matrix elements $\mathcal{G}_{i,i}^{\pm}$, $\mathcal{G}_{j,j}^{\pm}$, $\mathcal{G}_{k,k}^{\pm}$, $\mathcal{G}_{i,j,}^{\pm}$, $\mathcal{G}_{i,k}^{\pm}$, $\mathcal{G}_{j,k}^{\pm}$ (and the respective adjoint elements) are the only matrix elements appearing in the expression for the network GF of equation (4.11). This can be an enormous simplification when compared with the full diagonalisation method. Rather than inverting enormous matrices of dimension of $N \times L$, this technique allows us to express the network GF in terms of inverse operations of much smaller matrices, and whose sizes are defined by the total number of connections in the system, i.e. matrices of order $N \times \langle\alpha\rangle$.

Therefore, because of the particular structure in Dyson's equation, it is possible to reduce the Green function matrices, such that only the elements affected by the perturbation V are stored. Consider, for example, a CNT with a couple thousand atoms. If only 10 of these atoms interact with neighbouring nanotubes, then only the elements corresponding to these atoms and the propagators between them need to be stored, since only these will be affected by the perturbation. We take advantage of this property from the very beginning of our calculations. For instance, when constructing $g^{\pm}$, we only store the matrix elements corresponding to atoms affected by the inter-wire electronic hopping. Naturally, V has the same dimension as $g^{\pm}$, and we can perform calculations up to a thousand wires, each with a few thousand atoms.

4.4 Results and Discussion

We first apply our method to calculate the conductance of random networks of ideal nanowires, which here are modelled by monatomic linear chains. As we have already mentioned, it is possible to write analytic expressions for the Green functions of finite linear chains, therefore providing an opportunity to explore the features of our methodology with relatively small computational resources. Following these general results, we present calculations for the conductance of single walled carbon nanotube networks in a fully ballistic regime. The electronic transmission is analysed in terms of the network volume fraction and total number of junctions. We conclude this section by estimating an upper limit for the conductivity of carbon nanotube network films, which is directly extracted from our model, and compared with the best conductive films reported so far.

4.4.1 Ideal Nanowire Networks

Let us begin by analysing the conductance spectrum for an array of ideal monatomic wires. Figure 4.3(a) presents the conductance as a function of electronic energy for random networks with $N = 100$ wires with $L = 1000$ atoms each, and average connectivity $\langle \alpha \rangle = 6$ and $\langle \alpha_E \rangle = 1$. For each energy value, 100 independent configurations were considered, and the data presented is an average considering all realisations. It is known from the properties of random networks (See Ref. [120], for example) that $\langle \alpha \rangle = 6$ is above the percolation limit, which means that almost all the nodes are interconnected. Following the description in the previous section, each electrode is composed of a single semi-infinite wire, and thus the maximum theoretical value for the conductance of each configuration is limited by the electrodes to $\Gamma = \Gamma_0 = 2e^2/h$. Another feature that can be observed in the graph is that since we chose $\gamma' = \gamma_0$, the bandwidth of the network equals that of individual wires, which is $4\gamma_0$. The series of peaks and valleys on the conductance is caused

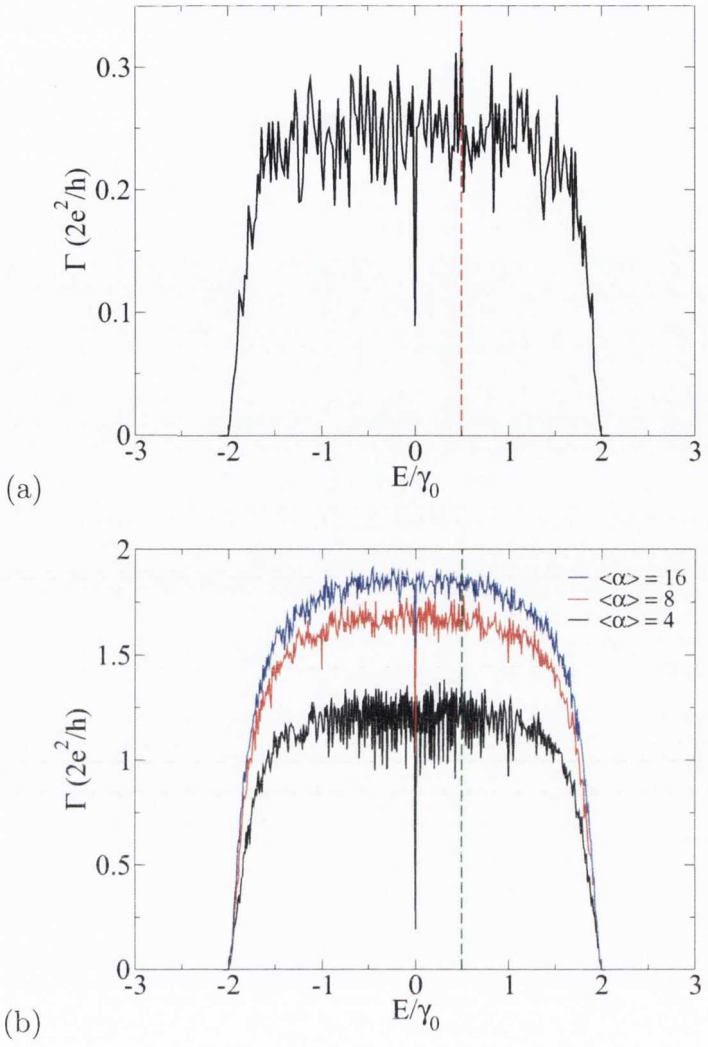

Figure 4.3: Conductance spectrum for networks with $N = 100$, $L = 1000$, and (a)$\langle\alpha\rangle = 6$, $\langle\alpha_E\rangle = 1$; (b)$\langle\alpha\rangle = 4, 8, 16$, $\langle\alpha_E\rangle = 5$. The vertical dashed lines at $E = 0.5\gamma_0$, indicate the fixed energy value at which the network conductance will be calculated in order to avoid the special situation arising due to resonance effects at $E = 0.0\gamma_0$.

by the finiteness of the wires, which present themselves as discrete energies in the spectrum. Whenever the electronic energy matches one of the eigenvalues of the finite chain's tight binding Hamiltonian we see a peak in the conductance, whereas a lower value for Γ is produced when there is a mismatch between the electronic energy and the Hamiltonian's eigenvalues.

On figure 4.3(b) we show how the connectivity of the network directly affects the conductance spectrum. We consider networks with $N = 100$, $L = 1000$, and

$\langle\alpha\rangle = 4, 8, 16$. It is clear that the average conductance increases with $\langle\alpha\rangle$, as it should since higher networks with larger connectivities present a larger number of conduction paths. In this case, we have fixed $\langle\alpha_E\rangle = 5$, which translates into a theoretical maximum conductance of $\Gamma = 5\Gamma_0 = 10e^2/h$. Once again there is a clear dispersion on the average conductance, however, it seems to decrease as $\langle\alpha\rangle$ is increased. This is expected since for higher connectivities independent configurations become more similar.

In both panels of figure 4.3 there is a clear drop on the average conductance at $E = 0.0\gamma_0$. These low conductance values are mainly caused by groups of atoms "dangling" from the conduction path. Atoms or molecules adsorbed on the external surface of nanotubes and nanowires affect the conductance along the longitudinal axis. In a tight binding description, it is possible to observe that lower conductance values arise when the energy of the conduction electrons matches one of the eigenvalues of the adsorbed structure [102]. In other words, when conduction electrons are in resonance with the eigenvalues of an adsorbed structure, the electrons tend to be heavily scattered, lowering the overall conductance along the axis of the wire. In the case of monatomic wire networks, each conduction path can be thought of as a long chain connecting source and drain electrodes, along which finite wire segments are attached. In this case, conduction electrons are heavily scattered when their energy matches one of the eigenvalues of the attached segment. The tight binding energy spectrum of a finite wire with L atoms is given by [150]

$$\varepsilon_m = \epsilon_0 + 2\gamma_0 \cos\left(\frac{m\pi}{L+1}\right); \quad 1 \leq m \leq L, \tag{4.16}$$

where the on-site energy ϵ_0 is set to zero. The eigenvalue $\varepsilon_m = 0.0\gamma_0$ corresponds to $\cos[m\pi/(L+1)] = 0$, which is only satisfied for $L = 2m - 1$ in equation (4.16). Therefore, $E = 0.0\gamma_0$ is always an energy eigenvalue of wire segments with an odd number of atoms. This particular feature makes $E = 0.0\gamma_0$ a special case, and

since we are interested in general features of network conductivity we should avoid it. To that end, it is necessary to consider an energy value that does not present any particular feature like the one just mentioned, therefore we set $E = 0.5\gamma_0$ as the fixed value of the electronic energy in our calculations. The dashed vertical lines in figure 4.3 indicate the chosen energy.

In order to better understand the role of each controllable parameter on the electronic transport across disordered networks, we investigate the effects of $\langle\alpha\rangle$ and $\langle\alpha_E\rangle$ independently. First we analyse how the connectivity between wires affects the conductance of the whole network. For general Erdös and Rényi random graphs [151], if the number of connections per node is too small, i.e. $1 \leq \langle\alpha\rangle < 2$, isolated islands tend to form instead of a connected percolating network and the conductance of the system is expected to vanish in the thermodynamic limit ($N \to \infty$). On the other hand, for $\langle\alpha\rangle = 2$ approximately 80% of the wires are interconnected, and a percolating cluster is always formed for $\langle\alpha\rangle \geq 2$. However, the electrodes must be connected to this largest cluster in order to form a conducting system. In particular, for $\langle\alpha\rangle = 2$, there is a 20% chance that any electrode wire will be connected to one of the smaller isolated islands, and will thus not contribute to the electronic transport across the network. For comparison, we state that on an Erdös and Rényi random graph with $\langle\alpha\rangle = 4$ the fraction of interconnected nodes is 98%, whereas for a graph characterised by $\langle\alpha\rangle = 6$ this fraction becomes 99.5% [120].

Figure 4.4 shows the dependence of the conductance at $E = 0.5\gamma_0$ as a function of the connectivity of the network. We consider networks with three different sizes $N = 100, 500, 1000$. The data was obtained considering wires of fixed length $L = 1000$ atoms, and the number of wires connected to each electrode (semi-infinite wires) is fixed at $\langle\alpha_E\rangle = 6$. The curves emphasise the influence of the network connectivity on the conductance, as the former is increased from its lower limit $\langle\alpha\rangle = 1$, up to values well beyond the percolation limit. Each data point is an

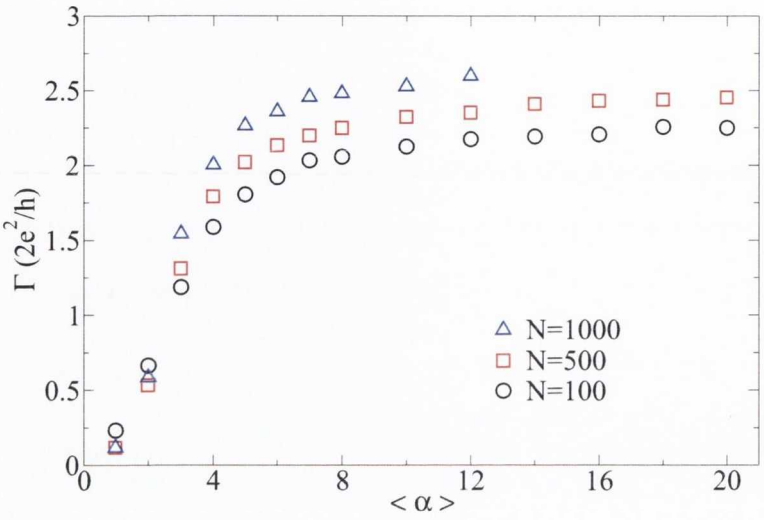

Figure 4.4: Conductance at $E = 0.5\gamma_0$ as a function of the connectivity of the network. Electronic transmission increases as more conducting paths become available. Legends indicate total number of wires. The length of the wires is fixed at $L = 1000$, and there are $\langle \alpha_E \rangle = 6$ connections to each electrode. Data averaged over 1000 independent configurations.

average over 1000 independent configurations, and all realisations were considered in the averaging procedure. The increase in conductance is caused by an increase in the number of available conducting paths for the electronic transport across the network. The saturation observed in the conductance of the networks as the connectivity is increased well beyond the percolation limit can be understood as a situation where the wires are fully interconnected. In this limit, the additions of extra possible paths for the electronic current will not have any noticeable effect on the conductance of the network. Furthermore, the increment in conductance with the number of wires N seen in figure 4.4, is also caused by the expansion of conducting paths, since the total number of unique connections in the network is given by $\langle \alpha \rangle N/2$.

Another major factor on the electronic transport of random nanowire networks is the number of wires connected to the electrodes. It is important to remember that each wire connected to an electrode provides a charge reservoir from where electrons come, and to where they finally go. Moreover, each one of these electrode

wires supports only one quantum of conductance, which can introduce a bottleneck effect on the system. For example, if $\langle \alpha_E \rangle = 1$, no matter how many conducting paths are present on the network, only one conduction channel is available for electrons moving from the network towards the drain electrode, and the maximum conductance is therefore limited to one quantum of conductance $\Gamma_0 = 2e^2/h$. On the other hand, for any connectivity beyond the percolation limit several conduction paths will be available on the network. Therefore, increasing $\langle \alpha_E \rangle$ will certainly improve the conductance of the network.

Figure 4.5 presents the direct effect of $\langle \alpha_E \rangle$ on the network conductance, for different values of $\langle \alpha \rangle$. The conductance of the whole network depends linearly on the number of connections to semi-infinite wires, with a slope that varies with the connectivity of the random network. The dashed lines are linear least-square fits to the data. As $\langle \alpha_E \rangle$ is increased the response in conductance is quite considerable, which indicates that once a percolating network is in place, the system's conductance is limited only by $\langle \alpha_E \rangle$. In any electronic device the quality of the electrode connections is crucial to the overall performance. In our model, as described above, the electrodes can act as a bottle neck to the electronic conductance, and as expected have a considerable influence on the overall conductance of the networks. On the inset, we show the variation of $d\Gamma/d\langle \alpha_E \rangle$ with the connectivity $\langle \alpha \rangle$, obtained from the slope of the linear-fitted lines. The slope reaches a maximum value for large enough connectivities, when an increase in the number of conducting paths available to the electrons does not alter the conductance of the network any further.

Finally, the conductance of random nanowire networks is expected to be strongly dependent on the probability of electrons to hop between neighbouring wires. This is directly related to the inter-wire hopping parameter. The inter-wire hopping is defined in analogy to the intra-wire hopping integral γ_0, and is denoted by γ'. In the tight binding model, the hopping integral represents the strength of the

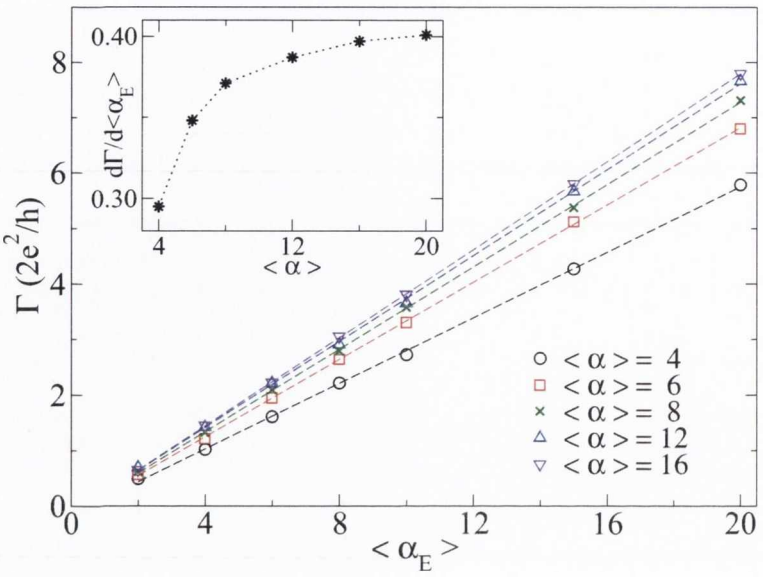

Figure 4.5: Network conductance as a function of the number of connections to electrodes, $\langle \alpha_E \rangle$. Inset: slope of the linear-fitted lines increases with the network connectivity $\langle \alpha \rangle$, towards a saturation point. Data is for $N = 100$, and $L = 1000$, averaged over at least 200 independent configurations.

bond between two atoms in a molecule or solid, therefore a higher value indicates a stronger coupling. In metallic nanowire and carbon nanotube films, the resistance arises mostly from inter-wire electron tunnelling, and thus, films with better coupled elements have lower overall resistance.

The inter-atomic (intra-wire) hopping is the only parameter in the tight binding model considered here, and so it is only natural that we choose to define the inter-wire hopping in terms of this parameter. That is to say, we analyse the influence of the ratio γ'/γ_0 on the conductance of the network. If the ratio is too small ($\gamma'/\gamma_0 << 1$) or too large ($\gamma'/\gamma_0 >> 1$) the mismatch between the couplings causes an adverse effect on the electronic transport through the system, lowering the conductance from its maximum possible value. In particular, considering only two semi-infinite wires connected to each other at the surface by a hopping γ' (forming an infinite linear chain), we can see on the upper panel of figure 4.6 that the maximum conductance occurs when the inter-/intra-wire couplings are equal to each other, *i.e.*, $\gamma'/\gamma_0 = 1$. This is not surprising if we bear in mind that

any contrast in the Hamiltonian parameters is a source of additional scattering. On the bottom panel of figure 4.6 we show the results for network conductance as a function of γ'/γ_0 for networks with $N = 100$, $\langle\alpha\rangle = 8$, $\langle\alpha_E\rangle = 6$, and $L = 1000$. In this case, it can be observed that the maximum conductance occurs for a ratio slightly larger than 1. This deviation from the unity ratio is caused by two independent factors. First, when an atom or molecule is adsorbed on the side of a nanowire or carbon nanotube, charge transfer effects can cause slight changes on the hopping parameters and on-site energies of atoms on the vicinity of the adsorption point. This correction can be calculated self-consistently in the so-called efficient screening approximation [145], but this correction is not taken into account in our calculations. Another factor interfering with the optimum hopping ratio has to do with the dangling clusters formed along the electronic current path. These can also affect the electronic transport by causing additional electronic scattering along the wires [102]. We have also observed that the actual maximum value of Γ and the ratio at which it occurs depends slightly on the fixed value chosen for the electronic energy.

So far we have presented results illustrating general properties of our computational framework applied to modelling the conductance of monatomic chain networks. It has been shown how the network parameters influence the electronic transport across the idealised films, and how the inter-wire hopping directly affects the films conductance. In the next section, this general methodology will be combined with the geometrical properties of carbon nanotube films, presented in chapter 3, in order to calculate the upper limit for the maximum conductivity of CNT films.

4.4.2 Application to Carbon Nanotube Networks

The results from the geometrical modelling presented in chapter 3 can now be combined with our quantum transport model, providing a multiscale approach to the

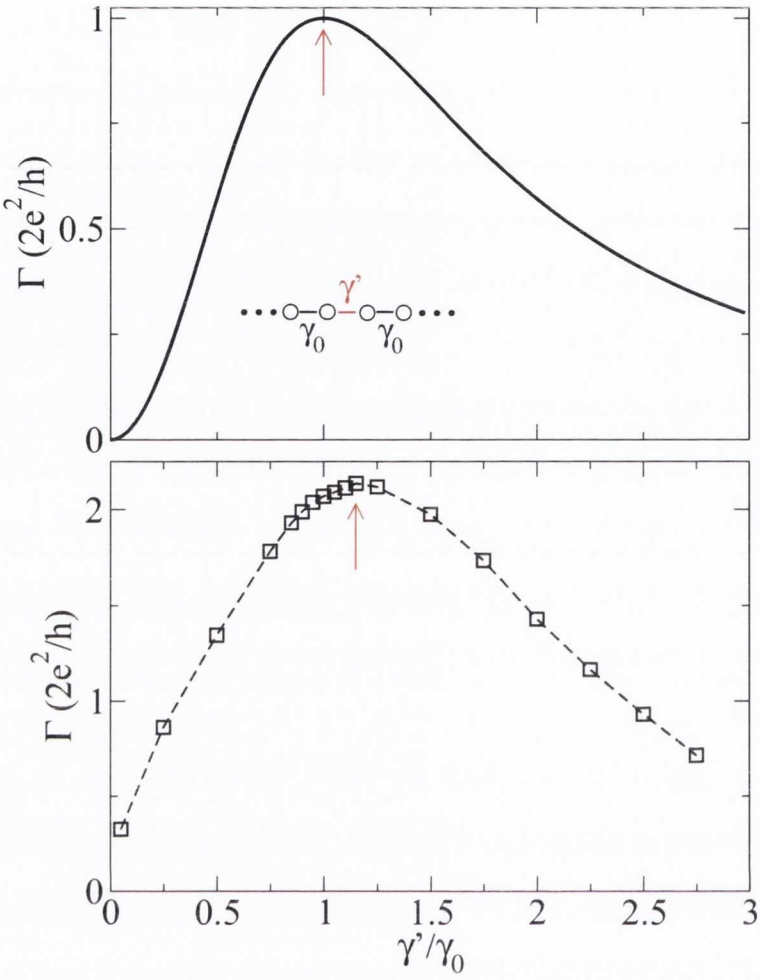

Figure 4.6: Top: Conductance of two semi-infinite chains connected by a hopping γ'. Bottom: Network conductance as a function of inter-wire/intra-wire coupling ratio. Maximum conductance is obtained around $\gamma'/\gamma_0 = 1.15$. $N = 100$, $\langle\alpha\rangle = 8$, $\langle\alpha_E\rangle = 6$, $L = 1000$, and 1000 independent configurations.

study of electronic transport in films containing networks of 1-dimensional conductors, namely carbon nanotubes. In chapter 3, section 3.2, we have presented results for the connectivity of disordered networks of rods. The results provide universal relations for the dependence of the network connectivity with experimentally accessible quantities such as the volume fraction of the films and the aspect ratio of individual wires, which also happen to be the parameters of our geometric percolation model. In particular, we have found that for a random network of rods with individual length ℓ and diameter D, inside a rectangular cuboid film of dimensions

given by $2\ell \times 2\ell \times 4\ell$, the average connectivity per rod is given by

$$\langle \alpha \rangle = (2.14 \pm 0.03) \times V_f \frac{\ell}{D}. \tag{4.17}$$

Furthermore, by considering that metallic electrodes are located on the opposing square faces of the film, and that any rod crossing these surfaces is taken to be in contact to that specific electrode, we found that the number of rods crossing each electrode can be written as

$$\langle \alpha_E \rangle = (1.35 \pm 0.07) \times V_f \left(\frac{\ell}{D} \right)^2. \tag{4.18}$$

Therefore, once the aspect ratio of the wires and the volume fraction of the film are chosen, $\langle \alpha \rangle$ and $\langle \alpha_E \rangle$ are automatically defined. These parameters are then fed into the general quantum transport model presented in the previous section, which yields the conductance for a network with the specified geometrical properties. Finally, since we have considered disordered networks to be defined inside a film of specified geometry, it is then possible to convert the network conductance into film conductivity. A result which can be directly compared with experimental measurements.

In the case of CNT films, the charge reservoirs are represented by semi-infinite nanotubes of same chirality of those in the network. Notice that this particular choice for the particle reservoirs is in complete accordance with our methodology. In practice, it accounts for the fact that each nanotube connected to an electrode serves as source or drain for the electron current. Once again, it is important to make sure that there are no short-circuits in the films.

We begin by investigating the conductance of networks made of $(5, 5)$ carbon nanotubes, which are classified as armchair CNTs and have a metallic band structure. The diameter of a $(5, 5)$ CNT is ≈ 0.68 nm, while the length depends on the number of unit cells considered. In a $(5, 5)$ SWNT, each unit cell has $4 \times 5 = 20$

atoms. We consider nanotubes of aspect ratio equal to $11, 16.5, 22, 27.4$, which correspond to lengths of 7.5 nm, 11.2 nm, 14.9 nm, 18.6 nm, respectively. For each of these aspect ratios, it is possible to vary the total number of carbon nanotubes in the films, such that the network volume fraction ranges from 0.065 up to 0.325. Moreover, through equations (4.17) and (4.18), the combinations of ℓ/D with V_f provide networks with $\langle\alpha\rangle$ in the range $3.6 - 7.5$, and $\langle\alpha_E\rangle = 27 - 77$.

In figure 4.7 it is shown how the network conductance depends on the volume fraction for the respective aspect ratios considered. Each data point is an average over at least 50 independent configurations, and the error bars represent the statistical error in the ensemble. Similarly to the resistive network results presented in chapter 3, there is a clear improvement in the conductance with a higher concentration of nanotubes. Moreover, we can also observe that higher network conductance values are achieved when the film is composed of nanotubes with larger aspect ratios. The dependence of the film conductance on the aspect ratio of individual nanotubes is in agreement with previous experimental studies [46, 152]. One possible way to account for this trend is to consider that, on average, a longer nanotube will have a larger distance between its junctions with other tubes. Therefore, on nanotubes with higher ℓ/D ratio the electrons will, on average, travel a longer distance along the tubes before experience heavy scattering caused by the inter-tube junctions.

It is also possible to analyse how the conductance depends on the total number of junctions in a network film of volume V, which was defined in chapter 3 as $N_J V = \langle\alpha\rangle N/2$. Figure 4.8 shows the averaged network conductance as a function of the total number of junctions in simulated films. We again see an increase in the overall film conductance as the aspect ratio of individual nanotubes is increased. Moreover, our model reproduce the approximate linear trend observed in experimental reports [122], which were also shown in the previous chapter.

Converting calculated values of network conductance into film conductivity can

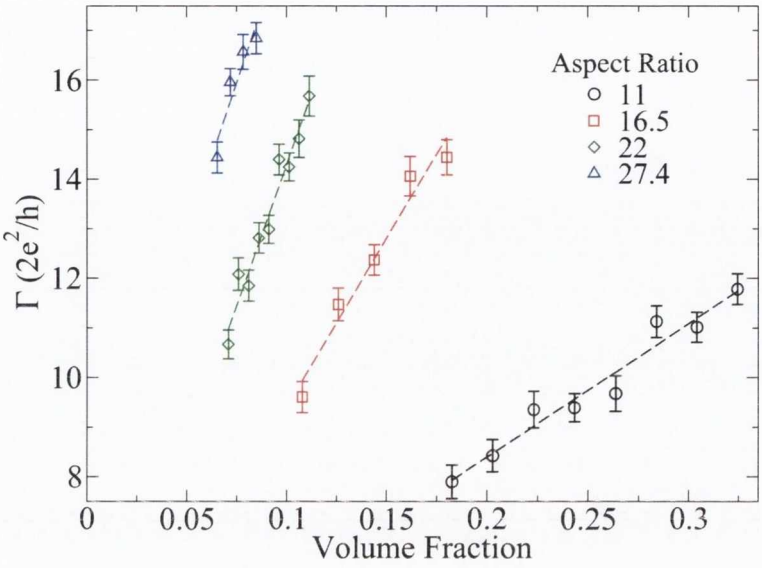

Figure 4.7: Conductance versus volume fraction for networks of $(5,5)$ armchair SWNTs. The legends indicate the aspect ratio of each data set. Higher aspect ratio CNTs provide better conductance, in accordance with experiments [46].

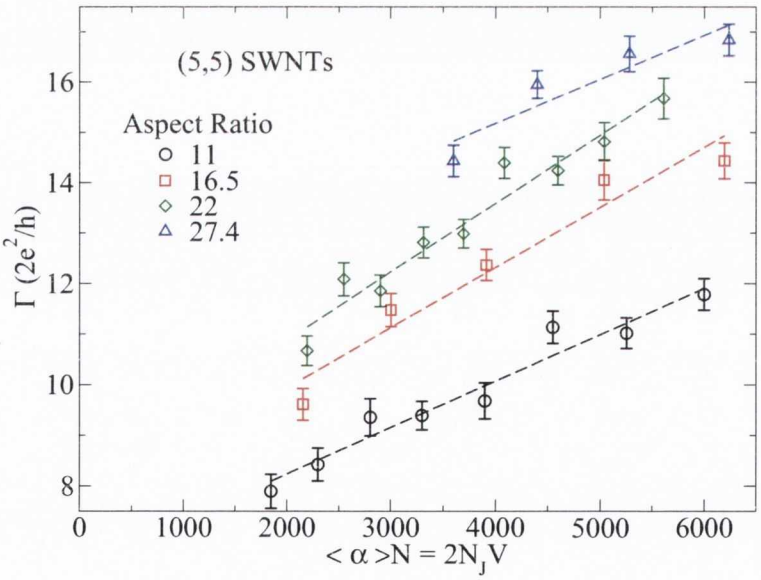

Figure 4.8: Averaged film conductance as a function of total number of nanotube junctions. Dashed straight lines are least-square linear fits to simulation data, in accordance with experimental results of ref. [122].

be done by considering the geometry of the films. Employing the usual relation between conductance and conductivity, it is possible to write

$$\sigma = \Gamma \frac{L}{A} = \Gamma \frac{4\ell}{4\ell^2} = \frac{\Gamma}{\ell}. \tag{4.19}$$

At this point, it is important to remember that Γ represents the conductance of an idealised network of finite-sized carbon nanotubes in a ballistic electronic transport regime. In the calculation of the conductance, we do not consider a series of decoherence-inducing factors which nonetheless are certainly present in experimental realisations. Therefore, the conductance we calculate is believed to be the upper limit for the conductance of a real film made of similar 1-dimensional conductors. Similarly, the conductivity calculated from our results, σ, represents an upper bound for the maximum electrical conductivity of real nanotube network films.

Based on an empirical analysis of the conductivity data, we find that it scales with a combined variable of the parameters V_f, ℓ and D. This dependence allows for a direct comparison of experimental data against our superior limit estimate. A comparison between experimental and simulation results, through the difference between the respective values, provides a direct indication of how much it is possible to further improve the transport performance of the laboratory produced films. Defining a scaled variable $x = V_f \times \ell / D^2$, we plot in figure 4.9 the dependence of the film conductivity (in units of siemens per meter) with x for nanotubes of varying aspect ratio. The data corresponding to networks of finite-sized $(5,5)$ SWNTs shows considerable dispersion, even after averaging over several configurations. Nonetheless, it is possible to identify a general trend on the data which stresses the linear dependence of the conductivity with x, represented by the least-squares linear fit indicated by the dashed (black) line. The dispersion on the data for CNTs is a direct consequence of the finite-length of the nanotubes considered. Since

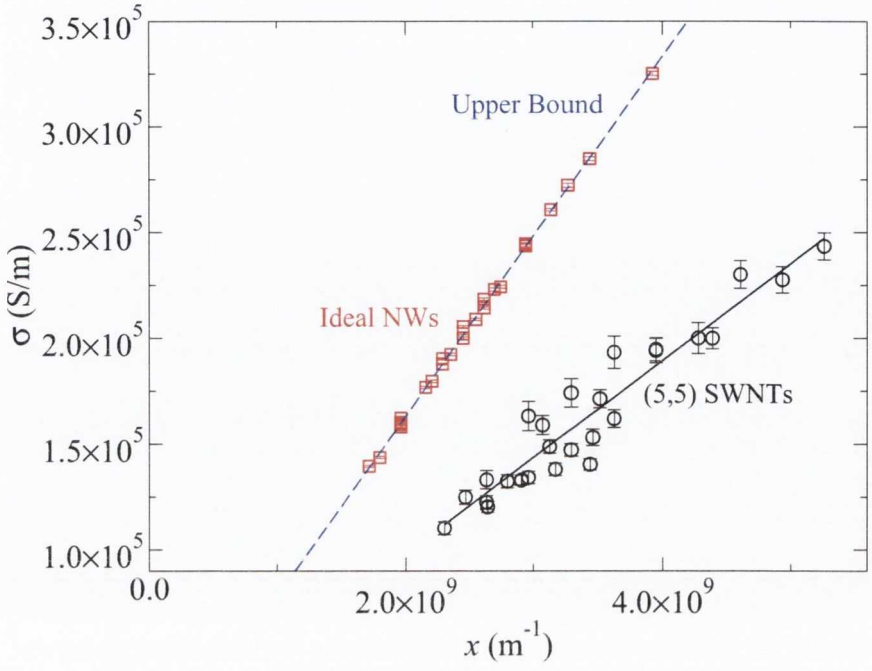

Figure 4.9: Maximum conductivity of carbon nanotube films as a function of scaled variable $x = V_f \times \ell/D^2$.

the Green function of independent nanotubes is calculated numerically, it quickly becomes too computationally demanding to increase the length of the nanotubes much further.

In order to overcome this computational limitation, we return to the case of linear monatomic chains, and investigate the conductance of networks made of idealised nanowires, represented by said linear monatomic chains. In order to compare the results with carbon nanotubes, we introduce an orbital degeneracy on the monatomic chain Hamiltonian and consider chains with two independent conducting channels. These monatomic chains present a maximum conductance of $4e^2/h$ at the Fermi energy, just like carbon nanotubes. Since we have an analytic expression for the Green function of linear chains (equation (4.4)), the computational limitations can be avoided, and we can consider very long chains. In order to minimise the finite-size effects on the local density of states, we study chains with $L = 16000$ atoms. Also shown in figure 4.9, is data obtained for the conduc-

tivity of networks composed of ideal nanowires, with varying volume fraction and aspect ratio. In this case we can see a much smaller dispersion on the calculated conductivity. Furthermore, by fitting a straight line to the nanowire conductivity we find

$$\sigma_u = M \times 4.25 \times 10^{-5} \times V_f \frac{\ell}{D^2} \quad (\text{in S/m}), \tag{4.20}$$

where the factor M accounts for the number of conduction channels in the wires. For the case considered here, we have defined $M = 2$. Because of all the idealisations applied to our calculations of the conductivity, the expression above is deemed to be the upper limit for the conductivity of random network films.

It is instructive to test the expression in equation (4.20) for typical SWNT values, namely $\ell = 1\mu$m and $d = 1.2$ nm. For $V_f = 30\%$, the predicted upper bound would be $\sigma_u = 1.8 \times 10^7$ S/m if CNTs of these dimensions could be fully dispersed to form the network. However, carbon nanotubes are known to bundle together, which means that in reality wire diameters are considerably larger. On the other hand, larger-diameter bundles have more nanotubes on the surface leading to more current-carrying channels per wire. Taking all this into consideration, we can compare our expression with the highest-conductivity case reported so far ($V_f = 30\%, \ell = 5\,\mu$m$, d = 20$ nm) [56, 86, 80]. Our prediction of $\sigma_u = 9 \times 10^6$ S/m is only one order of magnitude superior to the measured value of $\sigma = 6 \times 10^5$ S/m. Bearing in mind that the upper bound here obtained assumes a number of ideal conditions that are experimentally unavoidable, this might be a clear indication that we are approaching a saturation point in the conductivity of nanotube network films. It is interesting to notice that the calculated upper limit yields a ratio $\sigma_{dc}/\sigma_{op} \approx 530$ which, through equation (4.1), corresponds to a transmittance as high as 99% with a sheet resistance $R = 90\Omega$.

Finally, although our focus has been on disordered networks comprised of carbon nanotubes, we can extend our results to deal with other wires. This could

represent the case of networks made of other conducting materials, such as noble-metal nanowires, for instance. In this case the number of conducting channels M depends linearly on the wire diameter and the overall conductivity of the network is likely to scale inversely with D, with a proportionality constant that depends on the specifics of the material in question. If the conductivity of CNT network films is approaching its saturation point, it is likely that nanowires other than nanotubes may occupy the post of ideal components for disordered network films. Indeed, it has been shown recently [76] that silver nanowire network thin films might be a strong contender in the race for the next generation of transparent electrodes.

4.5 Summary and Conclusions

In this chapter we have shown how a quantum description of the electronic structure of individual carbon nanotubes nanotubes can be successfully coupled with the geometric features of rigid rod networks presented in the previous chapter. The resulting multiscale theoretical model provides a calculational tool capable of treating quantum electronic transport on disordered networks of generic nanoscale 1-dimensional conductors. The electrical conductivity of network films is fundamentally important for their performance as transparent electrodes, since this specific application requires a high ratio between the electrical conductivity and the optical conductivity.

We have shown that an electronic structure description based on semi-empirical tight binding Hamiltonians is capable of accounting for the heavily disordered environments found on nanotube networks. Based on this parametrised description we have developed a methodology based on single particle Green functions, which is general enough to account for a variety of nanostructured conductive networks. It has also been shown that it is possible to significantly reduce the computational resources required for the description of the problem, by selecting a convenient

way to express the Green function matrices of the system, and exploring a basic feature of sparse matrix products.

The general methodology developed has first been applied to idealised nanowire networks, and it has been shown how the connectivity of the wires, as well as the number of connections to the electrodes, control the conductance throughout the networks. In conjunction with results from the geometrical percolation model introduced in chapter 3, we have presented simulation results for the conductance of single-walled carbon nanotube networks.

Finally, by considering a fully ballistic transport regime on films of ideal nanowires, and comparing the ensuing results with typical experimental evaluations we have shown that carbon nanotube network films might be approaching their performance limit, and that perhaps metallic nanowires represent a more promising alternative to future developments.

The results presented in this chapter have been published in Refs. [153, 154].

Chapter 5

Further Applications

The methods developed in chapters 3 and 4 can be modified to tackle related problems involving network films. In the present chapter, two such related problems are considered. First, the possibility of utilising nanowire networks as a mediating spacer for magnetic coupling is investigated. Also known as Indirect Exchange Coupling, the interaction between magnetic moments separated by a non-magnetic material is known to be facilitated by conduction electrons in the non-magnetic spacer. As previously shown, nanowire networks present remarkable electronic conductance. The possibility of using network films in magneto-electronic devices, coupled with the computational tools we have developed to describe electronic transport in these networks, is a strong motivation to investigate networks as a magnetic coupling material.

The second extension of our methodology considered in this chapter is related to very recent experiments with silver nanowire films. Investigating the electronic transport characteristics of Ag NW films, by measuring $I - V$ curves, researchers found that a minimum voltage is required before a current can flow through the network. As the voltage bias is increased beyond this triggering voltage, the current eventually saturates. Decreasing the voltage from its maximum value down to zero, experimentalists have observed a hysteresis-like behaviour in the $I - V$

curves. It has been hypothesised that this hysteresis behaviour is caused by impurities reminiscent of the growth of Ag nanowires, or of the deposition process. These impurities are known to preferably locate themselves near junctions between nanowires. When the voltage is high enough the charge build-up will put the impurities under a high electric filed, which might cause an electrical breakdown. The impurities located at junctions behave like capacitors and a model capacitive network can be applied to study the onset of electrical activation in silver nanowire networks.

5.1 Magnetic Interactions Mediated by Random Networks

The interaction between magnetic moments has been a topic of study for several years. On the atomic scale, the exchange interaction between nuclear magnetic moments embedded in metallic systems has been investigated in detail, mainly due to its vast array of applications. Direct exchange interaction takes place when there is an overlap of the wavefunctions surrounding the respective magnetic moments, which decays rapidly as the distance separating the magnetic objects is increased. However, on the atomic scale, an indirect exchange interaction between nuclear magnetic moments embedded in metallic systems has also been observed. This indirect exchange coupling has been explained as being facilitated by conduction electrons in the metal. Unlike the direct interaction which decays rapidly and monotonically with the distance between the magnetic objects, indirect exchange coupling presents a characteristic oscillatory decay and can behave as a very long ranged interaction.

Theoretical approaches to indirect exchange coupling (IEC) were originally concentrated on understanding the behaviour of the coupling between magnetic impurities embedded in metallic structures [155]. Years later, theories were developed to

explain experimental observations of coupling between physically separated magnetic layers. In these experiments, two (or more) layers of a magnetic material are separated by layers of non-magnetic materials. It was clear from the beginning that the observed magnetic couplings could not be accounted for by direct exchange, and therefore should be a manifestation of IEC. The research on exchange coupling on magnetic multiplayers led to the discovery of the effect know as giant magneto resistance, which is the standard technology on current magnetic data storage devices [156, 157, 158]. The massive advancement of nanotechnology in recent years naturally led to the study of magnetic exchange coupling on nanometric systems. Carbon nanotubes present very low electronic spin-orbit coupling [159], and are believed to be a class of material which could present very long range magnetic interactions [147, 160]

Because IEC is mediated by the conduction electrons of a non-magnetic spacing material between magnetic moments, and since electronic transport on disordered networks is the major focus of this thesis, we decided to investigate if an indirect coupling mediated by random networks would arise. Previous theoretical approaches have been developed to provide a way of calculating the magnetic coupling from the Green function of the mediating system. In chapter 4 a general formalism was developed to express the Green function of a disordered network in a computationaly efficient fashion. Our approach to the problem of IEC mediated by networks aims at coupling the well established theoretical tools with our newly developed techniques. In what follows we introduce the general picture used to investigate IEC, and proceed to apply it to disordered networks. Our major motivation is to test whether nanowire networks can also be used to transmit magnetic information.

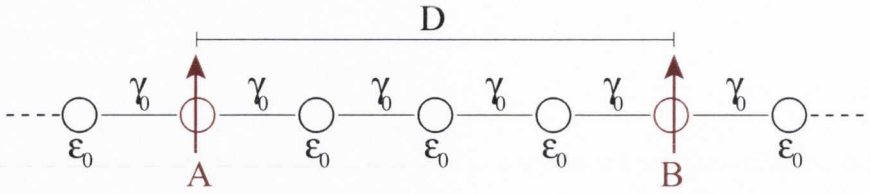

Figure 5.1: Indirect exchange coupling between magnetic moments located at A and B is mediated by the conduction electrons of the host structure, represented here as an infinite linear chain. The sign of the coupling changes with the distance D.

5.1.1 Indirect Exchange Coupling

A simple description of magnetic coupling in a multilayer system can be obtained within a one-dimensional picture. In figure 5.1, a one dimensional structure is represented by an infinite linear chain of atoms. There are two magnetic moments located at sites A and B, separated by a number of inter-atomic spaces given by D. Within a simple description, the magnetic moments can only be oriented parallel or anti-parallel to each other. The magnetic coupling between these two moments is given by the difference between the total energy of each configuration. Using the parallel configuration as reference, the coupling is given by

$$J(D) = E_T^{\uparrow\uparrow} - E_T^{\uparrow\downarrow}, \tag{5.1}$$

where $\uparrow$ and $\downarrow$ represent the spin orientation of each moment. Rather than calculating the total energy of each configuration, it is possible to calculate the energy difference directly with the use of Lloyd's formula [161, 162, 163, 164]. In its essence, the Lloyd formula gives the change in the density of states of a system caused by a given perturbation without having to diagonalise two different Hamiltonians. The Lloyd formula method is related to Dyson's equation, which was presented in chapter 2.

Using Lloyd's formula, it is possible to show that the indirect exchange coupling

between two magnetic moments, separated by a distance D, is given by [146, 165]

$$J(D) = -\frac{1}{\pi}\int_{-\infty}^{\infty} dE f(E) \mathrm{Im}\left\{\ln\left[1 + 4V_x^2 G^{\uparrow}_{AB}(E,D) G^{\downarrow}_{BA}(E,D)\right]\right\}, \tag{5.2}$$

where $f(E)$ is the Fermi function, V_x is the spin split potential, A and B specify the site or layer in which the moments are located, and $G^{\uparrow(\downarrow)}$ are the propagators for spin-up and spin-down electrons between the magnetic moments in the parallel configuration. The spin split potential lifts the degeneracy in the magnetic moment of conduction electrons, by giving a different on-site potential to each spin orientation in the impurity sites.

The spin-dependent propagators can be calculated directly from Dyson's equation, and are given by

$$G^{\sigma} = \mathcal{G} + \mathcal{G} V^{\sigma} G^{\sigma}, \tag{5.3}$$

where the propagator between A and B is given by

$$\mathcal{G} = \begin{pmatrix} \mathcal{G}_{AA} & \mathcal{G}_{AB} \\ \mathcal{G}_{BA} & \mathcal{G}_{BB} \end{pmatrix}, \tag{5.4}$$

and the spin-dependent potential is written as

$$V^{\sigma} = \begin{pmatrix} \lambda^{\sigma} & 0 \\ 0 & \lambda^{\sigma} \end{pmatrix}, \tag{5.5}$$

with $\lambda^{\uparrow} = -V_x$ and $\lambda^{\downarrow} = V_x$. Conduction electrons propagating along the linear chain feel a different on-site energy at sites A and B, which depends on the spin of the conduction electrons.

For a typical 3D layered structure the indirect exchange coupling decays with distance as $1/D^2$. However, for one-dimensional systems the coupling is long ranged and decays as $1/D$. Furthermore, the coupling shows a characteristic oscillatory

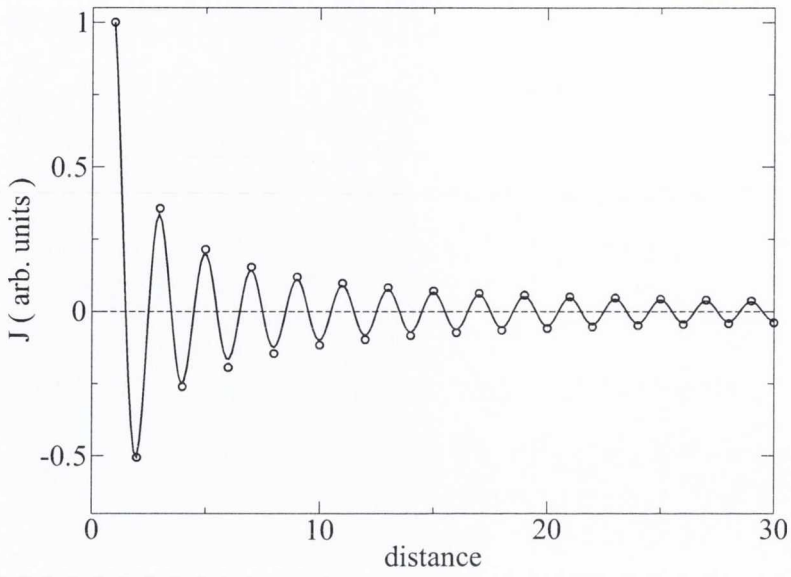

Figure 5.2: Indirect exchange coupling between magnetic moments embeded in a linear chain. The period of oscillation is determined by the Fermi energy of the host, in this case $E_F = 0.0\gamma_0$. The solid line is a guide to the eye.

behaviour as the separation between the magnetic moments is increased. Figure 5.2 shows the oscilatory decay of $J(D)$ on a monatomic linear chain, with magnetic impurities located at site A and B, a distance D apart. The period of oscillation is defined by the Fermi energy of the host material, in this case the linear chain. In the figure, the Fermi energy was set at $E_F = 0.0\gamma_0$. When the coupling is positive, the magnetic moments will be aligned in the anti-parallel configuration, whereas when $J < 0$ the coupling is ferromagnetic and the moments are aligned parallel to each other. In the figure shown, the period of oscillation is one atomic plane, such that the coupling oscillates between positive and negative as the separation is increased one plane at a time. In any crystalline system the distance will always be an integer number given by some lattice parameter, however, using an analytical expression it is possible to calculate the coupling at non-integer distance, as it is shown by the solid line in figure 5.2.

Since indirect exchange coupling is mediated by conduction electrons of the spacer system, it would be interesting to investigate the possibility of calculating the coupling between magnetic moments separated by a conductive random net-

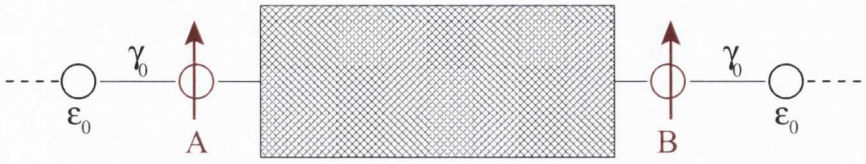

Figure 5.3: Schematic representation of the setup used for calculating the indirect magnetic coupling mediated by conduction electrons of a disordered network. The central rectangular area contains a network of N finite wires with average connectivity $\langle\alpha\rangle$.

work. Similarly to the construction used to study the conductivity of nanotube networks, the magnetic moments are placed at the end of semi-infinite structures, which are then connected to finite wires in the random network. Figure 5.3 illustrates in a schematic way the setup of the system. The magnetic coupling can be calculated directly from equation (5.2), where the network Green functions are calculated in the efficient numerical fashion described in chapter 4.

5.1.2 Results

A random network with $N = 100$ finite linear chains of length $L = 1000$ atoms each, and with an average connectivity equal to $\langle\alpha\rangle$ was used as spacing between two magnetic moments. Several samples are required to obtain statistically significant results, and figure 5.4 shows the histogram of couplings calculated for networks with increasing connectivities. Because of the disordered nature of the networks, the magnetic coupling is expected to be very small. However, a more important issue is apparent from the histograms. The calculated couplings are approximatelly equally distributed around zero. Depending on the connections throughout the network, the magnetic moments might couple parallel or anti-parallel to each other, whith almost equal probability. It is very hard to control the "distance" between the magnetic atoms on this system, and the statistical character of the networks causes the average coupling to vanish.

On a multilayer system, the period of oscillation of the indirect exchange coupling is controlled by the Fermi energy of the material hosting the magnetic mo-

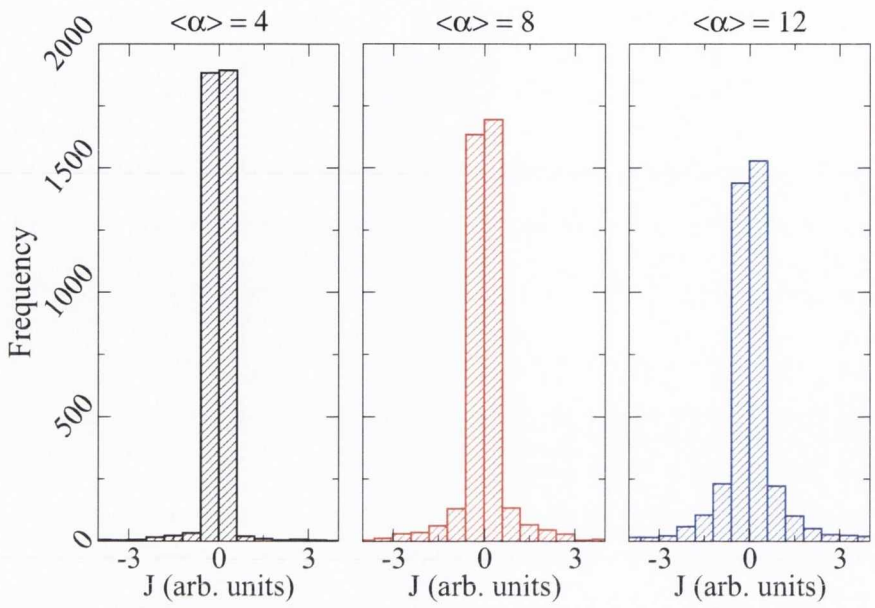

Figure 5.4: Histogram of the calculated values for the magnetic coupling mediated by random networks. As the connectivity of the network increases, the histograms become broader, but are approximatelly equaly distributed around $J = 0.0$.

ments. Furthermore, commensurability effects might suppress the characteristic oscillatory behaviour of J [166, 167], or even cause the coupling to vanish. It is therefore interesting to analyse the possible influence of the Fermi energy on the coupling mediated by a network. The indirect exchange coupling between two magnetic moments separated by a random network of idealised nanowires is shown in figure 5.5. For systems with three different values of the Fermi energy, networks of increasing connectivity were considered. Each data point is an average over at least 3000 samples. The dashed line indicates the location of $J = 0$. In spite of the large number of independent configurations generated, the error bars in each data point are still significant. Furthermore, almost all points lie within the dashed line $J = 0$ when error bars are considered. These preliminary results are an indication that unfortunately there is no magnetic coupling mediated by conduction electrons through the network. However, it is also possible that the vanishing average coupling is a consequence of the very own disordered nature of the network, which couples the moments parallel and anti-parallel with equal probability.

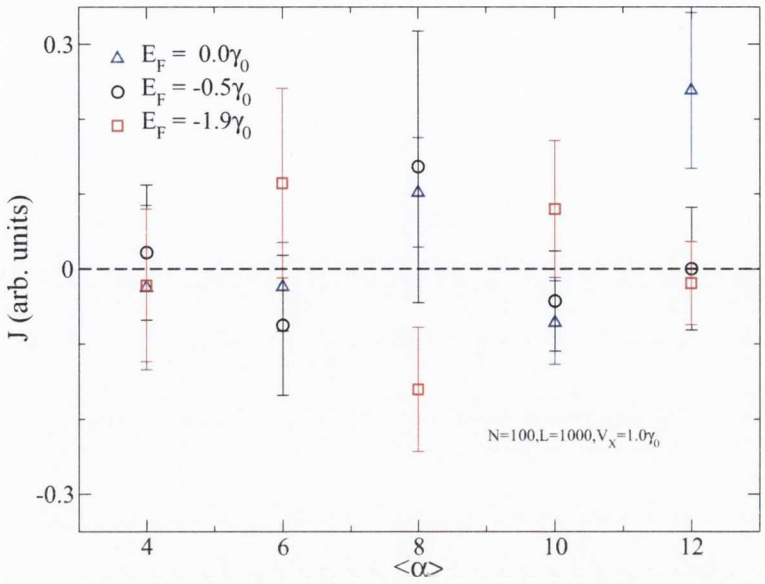

Figure 5.5: Indirect exchange coupling as a function of network connectivity. The Fermi energy of the mediating material controls the period of oscillation of the coupling. Within error bars, almost all points agree with the dashed line representing a vanishing coupling.

It is possible to show that the size of a random network is related to its total number of nodes. In a further attempt to observe indirect exchange coupling mediated by networks, systems with a increasing number of wires have been investigated. The results obtained do not show any sign of dependence with the size of the network considered, which is taken as further indication that the average coupling is in fact vanishingly small. It would be interesting to have experimental measurements performed in these systems in order to prove or disprove our predictions. To the best of our knowledge, this topic has not yet been considered by the experimental community.

Unfortunately, in the first application shown in this chapter we have obtained negative results. However, in the next section we consider yet another application of the methodologies developed in this thesis work. This time we consider recent experimental results and our model achieves considerable success.

5.2 Silver Nanowire Films as Capacitive Networks

Thin films fabricated by deposition of silver nanowire solutions can also be used as flexible transparent electrodes. As a matter of fact, based on the theoretical calculations of the upper limit for the conductivity of carbon nanotube films, presented in chapter 4, we have found that metallic nanowires present an excellent alternative to nanotubes in the production of network films. The number of conducting channels on a nanowire scales with its diameter, while for nanotubes the number of channels is limited to a maximum of two. Recent experiments have shown that silver nanowire thin films are indeed capable of achieving the minimum conductivity required for application in flexible displays [76]. Figure 5.6(A) shows a 3D micrograph of a typical silver nanowire film. The image was obtained with an Atomic Force Microscope (AFM) and shows the topographical structure of a silver nanowire film. The colour scale to the right of the micrograph indicates the height of each point in the image.

Very recent (yet unpublished) experiments performed by Nirmalraj et al. to address the transport properties of silver nanowire networks have shown intriguing results. Using atomic force microscopy to measure the electrical resistance between the AFM tip and an electrode deposited on one end of the film, it was found that a minimum voltage bias is required to "activate" current pathways in the network. Increasing the bias voltage between the AFM tip and the electrode it was found that it is possible to activate specific clusters of nanowires without affecting the whole film. Figure 5.6(B)-(F) shows current maps obtained at different voltage biases, with an electrode located on the right hand side of the images. In 5.6(B), a well connected current map was obtained by applying a voltage bias of 6 V. Analysing the same area of the film after electrical activation under lower bias conditions of 100 mV, 1 V, 2 V and 4 V results in well resolved current maps as shown in panels (C), (D), (E) and (F), respectively. Based on the AFM current

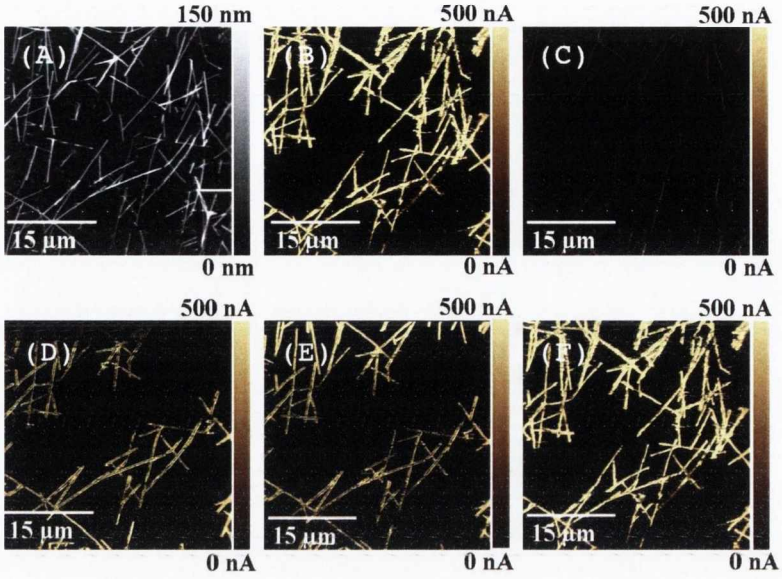

Figure 5.6: AFM analysis of electrical activation of silver nanowire networks. (A) Topography of a region of sparse Ag nanowire networks. A step wise increase in the applied bias voltage from 10 mV up to 5.5 V showed a threshold voltage at ≈ 6 V. After applying a 6 V bias the current pathways are triggered across the network and a well connected current map is obtained (B). The electrode is on the right hand side of the image. There is no obvious gradient across the current map, which is indicative of excellent electrical connectivity in the network. Analysis of the same area after electrical activation under lower bias conditions of 100 mV, 1 V, 2 V and 4 V provides well resolved current maps as shown in (C), (D), (E) and (F), respectively. Experimental measurements performed by P.N. Nirmalraj, Trinity College Dublin.

maps it is possible to infer that once a current pathway has been activated by a high enough voltage bias, it continues to conduct at lower biases.

Current–voltage curves measured at different tip–electrode distances show a hysteresis-like behaviour. Starting from low voltages, it was found that current only flows through the network for bias voltages higher than a *triggering voltage*, which activates specific current paths in the film. Retracing the measurement starting from high voltages, it was found that the $I - V$ curve is not the same. Figure 5.7 shows the current–voltage behaviour of silver nanowire networks, measured at increasing electrode–tip distance. Each set of data clearly shows that a minimum voltage is required to obtain an electrical current through the network. Furthermore, the measurements also show that the minimum voltage required to activate

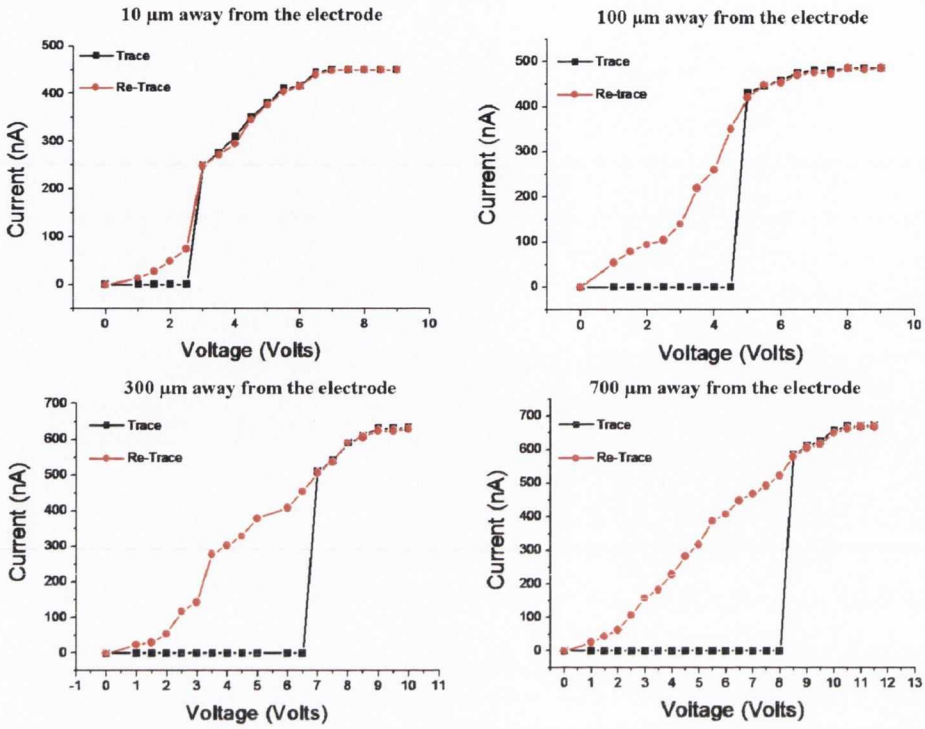

Figure 5.7: Local current voltage behaviour of Ag nanowire networks as a function of distance from electrode. Current is monitored as a function of an applied steady bias. A certain magnitude of voltage is required to activate current pathways, and the magnitude depends on the distance to electrode. Once a pathway has been activated it remains in place even at very low bias. Experimental measurements performed by P.N. Nirmalraj, Trinity College Dublin.

the current pathways, defined above as the triggering voltage, increases with the electrode–AFM tip distance. The hysteresis behaviour of the current–voltage maps shown in figure 5.7 has led to the hypothesis that impurities reminiscent from the film fabrication process block the current at nanowire junctions, up to the point when the charge build up is enough to cause an electrical breakdown of the impurity. In other words, impurities located at nanowire junctions suppress the current up to the point when the voltage is high enough to remove the impurities. Once the impurities have been removed, the current pathways are free to conduct down to very low bias voltages, as shown in figure 5.7 and figure 5.6(C)-(F).

Measuring current–voltage curves at increasing electrode–AFM tip distance

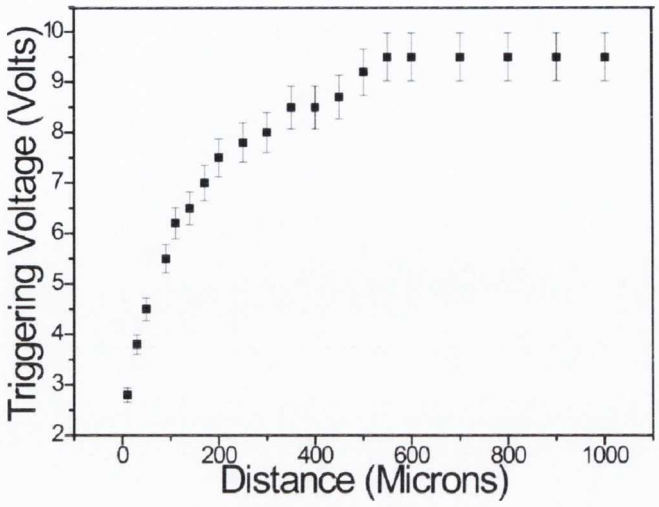

Figure 5.8: Magnitude of the triggering voltage as a function of the distance from the AFM tip to the electrode. Triggering voltage increases with the distance from the electrode up to a saturation point. Measurements also performed by P.N. Nirmalraj, Trinity College Dublin.

makes it possible to investigate the exact dependence of the triggering voltage with distance, as shown in Figure 5.8. The triggering voltage increases sharply at small distances, and saturates when the tip–electrode distance is large enough. For small distances, the charge build up will be concentrated on a few nanowire junctions, and a lower bias voltage will be enough to cause an electrical breakdown of the impurities. At larger distances much more junctions are involved in the charge build up, and a higher bias voltage will be required. Once an electrical breakdown occurs at a specific junction, it quickly expands to neighbouring junctions in a type of avalanche-like chain reaction. Silver nanowire networks are similar to nanotube networks, as shown by micrographs in figure 4.1. A model similar to the resistive networks developed to investigate electrical resistance in nanotube films might be able to shed some light on the phenomenon of local electrical activation in silver nanowire films. In particular, a simple model can be developed to test the hypothesis raised by the analysis of the experimental data for Ag network films.

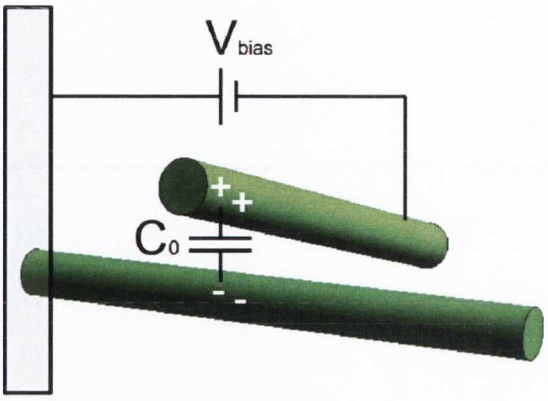

Figure 5.9: Schematic representation of the charge build up at a junction between two nanowires, represented by rods. A capacitor C_0 represents the impurities blocking the electrical current at the junction. A bias voltage is applied between the nanowires when one is connected to the electrode and the other one is in contact with the AFM tip.

5.2.1 Capacitive Network Model

The resistive network model was applied in chapter 3 to study the electronic transport on a nanotube network, where the onset of a triggering voltage is not observed. A modification of the model, where Ohmic resistors are replaced by capacitors, should be able to capture the onset of activation of electrical paths shown in the silver NW films. In essence, the hypothesis raised indicates that impurities are located at nanowire junctions such that direct contact between nanowires is physically blocked. By applying a voltage difference between the electrode and the AFM tip a charge build-up will occur at the junctions, as illustrated in figure 5.9. When the voltage bias is high enough, the impurities will be under a high electric field, and will eventually cause a breakdown. A similar behaviour is known to happen to capacitors, where an electrical breakdown is caused by high voltages.

In order to test the hypothesis, we have designed a model based on a capacitive network. The network consists of nodes connected by capacitors, such that the voltage difference between two adjacent nodes equals the voltage difference on the terminals of the respective capacitor. In analogy to equation (3.10) in chapter three, the voltage on every node of the network can be mapped through a matrix

equation written as

$$\mathbf{V} = \frac{1}{C_0}\mathbf{M}^{-1}\mathbf{Q}, \tag{5.6}$$

where C_0 is the capacitance of each capacitor, and $\mathbf{M}$ is exactly the same matrix as defined in chapter 3. The matrix $\mathbf{Q}$ represents the charge in each capacitor in the network, and is proportional to the bias voltage applied. The electrode is placed along the nodes on the top edge of the network, and the AFM tip can be represented by any other node in the network. The application of a bias voltage between the electrode and the AFM tip induces a positive charge distributed along the line of nodes representing the electrode, and an equal but negative charge is induced in the node representing the AFM tip, located a distance d from the top edge. Figure 5.10 illustrates the capacitive network, as well as the parameters of the model. In the experimental setup, the induced charge is controlled by the bias voltage between the electrode and the AFM tip. In our model, by varying the total charge induced it is possible to calculate the voltage across each capacitor in the network. When the voltage difference on the terminals of a given capacitor is larger than the maximum it can sustain, the capacitor breaks down, and that current path is now activated. As soon as one of the capacitors breaks down it starts a chain reaction throughout the network, and more and more capacitors connected to the original one also experience this electrical breakdown. A current pathway is formed when the first capacitor in the electrode breaks down. The respective voltage at which this occurs is defined as the triggering voltage.

For the sake of simplicity, we consider first a finite square lattice with identical capacitors located in each vertex. For each specified distance between the electrode and the AFM tip, we vary the total charge induced on the electrode and the node representing the AFM tip, and calculate the voltage difference on the terminals of each capacitor using equation (5.6). It is convenient to remind the reader that equation (5.6) is also valid for non-regular networks, as long as the appropriate

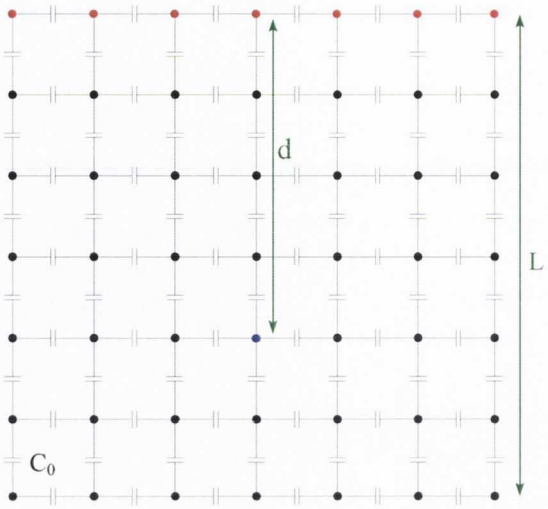

Figure 5.10: Schematic representation of a square capacitive network. A capacitor C_0 is placed between every two adjacent nodes. A bias voltage is applied between the nodes located on the top edge of the network and a node located a distance d away.

matrix $\mathbf{M}$ is written accordingly, and it can also be applied to analyse electrical breakdown on networks with a complex structure. The numerical value of the breakdown voltage V_{break} is chosen somewhat arbitrarily, and the triggering voltage is defined as the voltage at which the first capacitor in the electrode breaks down. The specific value of the triggering voltage will naturally depend on V_{break}, but the qualitative dependence of the triggering voltage with the distance from the electrode should not. In fact, this is all that is needed in order to verify the original hypothesis.

5.2.2 Results

We consider the square capacitive network of figure 5.10 with a lateral dimension $L = 80$ nodes. The vertical distance between the electrode and the AFM tip d, is measured as the number of capacitors between the two. Finally, the voltage bias between the electrode and the tip is proportional to the total charge induced on the electrode (positive) and the AFM tip (negative), and in our model is defined as having arbitrary units. Throughout this section we set the breakdown voltage

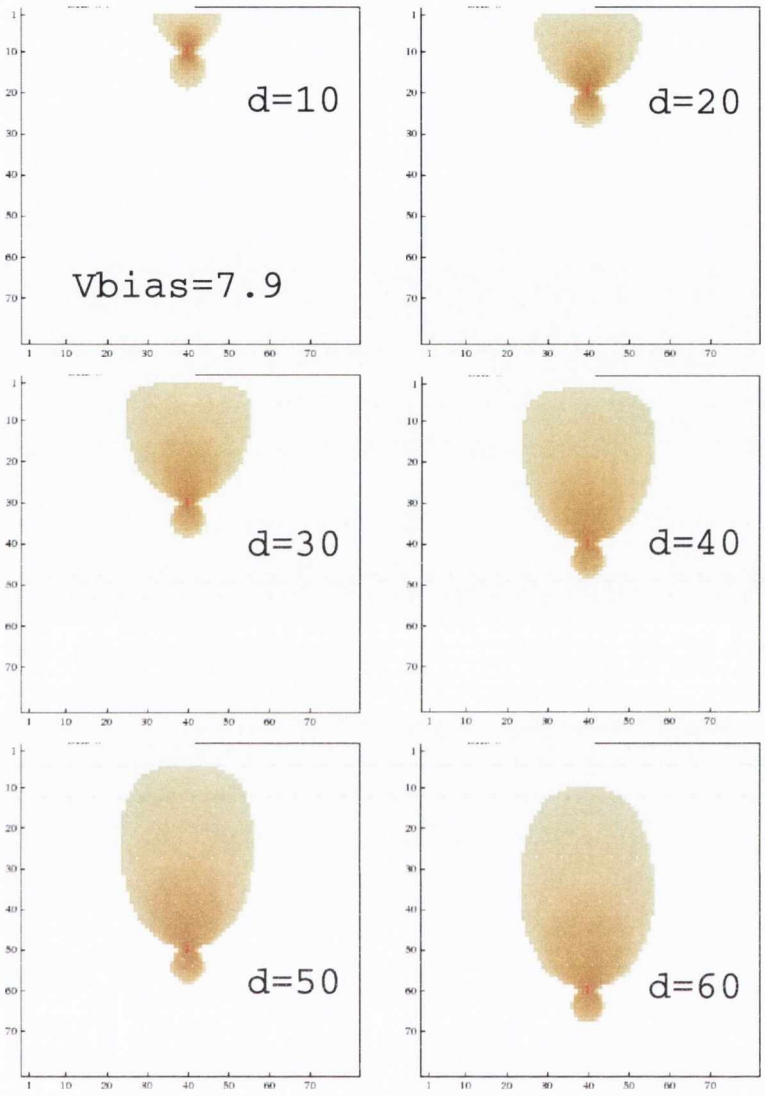

Figure 5.11: Colour plot of the voltage difference across capacitors in the network. Only capacitors above breakdown voltage are shown. Darker spots represent higher voltages. The electrode is located on the top of each panel, as indicated in figure 5.10.

$V_{break} = 0.1$, also in arbitrary units. As mentioned above, changes in this value bring no qualitative differences to our results.

Let us begin by submiting the system to a fixed bias voltage $V_{bias} = 7.9$. Solving equation (5.6) we obtain the electric potential in each node of the network. Figure 5.11 shows the cluster of capacitors whose voltage difference along the distance d is higher than $V_{break} = 0.1$. The voltage across each capacitor is proportional to the colour of each point. Darker spots mean higher voltages. The breakdown

cloud starts from the node representing the AFM tip, because this is the spot that concentrates the highest amount of induced charge in the whole network. The electrode is located on the top of each individual panel, as illustrated in figure 5.10. As the distance from the electrode is increased the shape of the breakdown cluster expands, and the number of capacitors subjected to a voltage difference higher than V_{break} increases. If the cloud reaches the electrode, then a direct current pathway to the AFM tip has been activated. For $d = 10, 20, 30$, the cloud clearly extends up to the electrode. As the distance reaches $d = 40$, the cloud does not touch the electrode anymore. At this point, the are no current pathways leading from the AFM tip to the electrode. The situation is the same for $d = 50, 60$, at this bias voltage. This preliminary analysis is in agreement with the experimental data, which shows a clear increase in the triggering voltage with the distance d, as in figure 5.7.

In figure 5.12 the distance from the AFM tip to the electrode is fixed at $d = 70$, while the bias voltage is slowly increased. Starting from $V_{bias} = 5$, it is possible to observe how the breakdown cloud expands as the voltage is increased, up to the point where it reaches the electrode. The transition from no current pathway, to fully formed current pathway is very sharp, and for the case shown, it happens between $V_{bias} = 7.9$ and $V_{bias} = 8.0$. The sharpness of this transition, allows us to determine the triggering voltage with very high precision. Once the breakdown cloud reaches the electrode, it quickly expands to all capacitors connected to the electrode, as shown in the figure for $V_{bias} = 8.02$, and $V_{bias} = 8.1$. The transition from the non-conducting state to the conducting one becomes sharper as the electrode–AFM tip distance increases. Preliminary studies of networks with different size have shown a similar qualitative behaviour near the transition, but a systematic study of size-dependent effects on the transition is not yet available.

Figure 5.13 is a plot of the fraction of capacitors in the network subject to a voltage difference higher than the breakdown voltage. As the bias voltage is

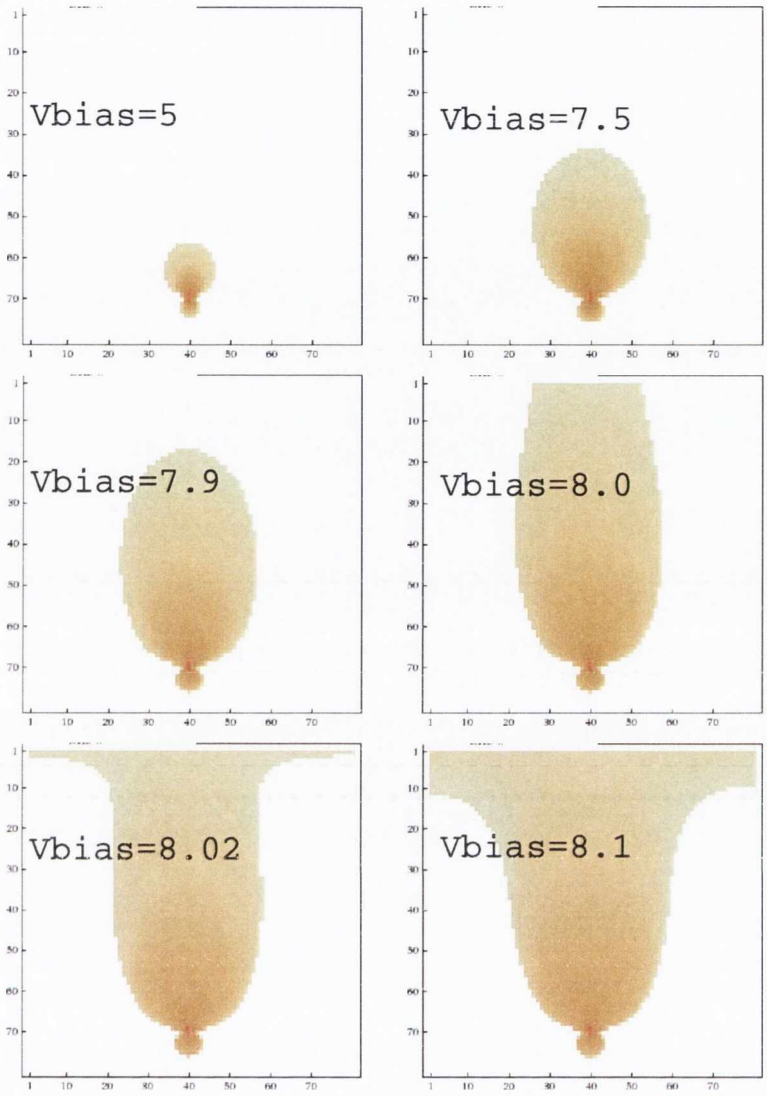

Figure 5.12: Breakdown cloud similar to figure 5.12, with electrode–AFM tip distance fixed at $d = 70$. Figure 5.10 shows a diagram of the underlying capacitive network. Triggering voltage for the network is defined as the bias voltage necessary to breakdown one of the capacitors connected to the electrode. In this case, $7.9 \leq V_{trigger} \leq 8.0$.

increased the fraction shows a sharp increase. The corresponding voltage bias is a very good indication of the location of the triggering voltage. In this particular case, we see it is very close to $V_{bias} = 8.0$. The exact determination of $V_{trigger}$ is done by finding the bias voltage at which the first capacitor connected to the electrode breaks down. The determination of $V_{trigger}$ for each value of d can be done with very high precision, and it is shown in figure 5.14. For a network of

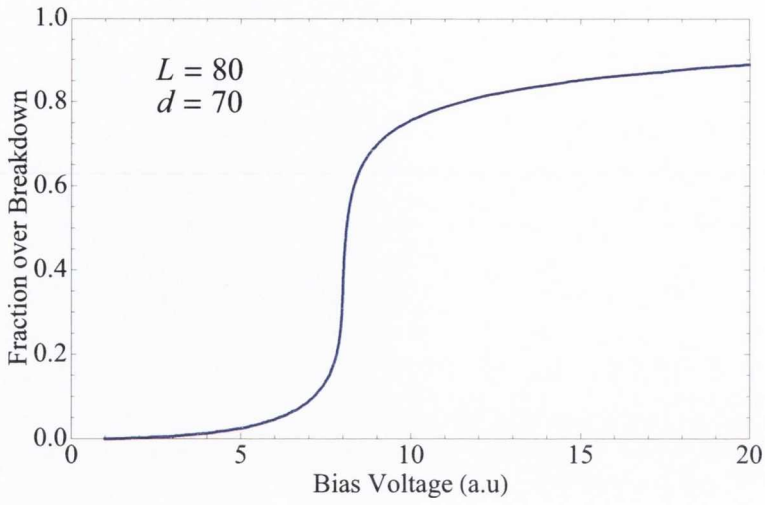

Figure 5.13: Fraction of capacitors in the network taking part on the breakdown cloud as a function of the bias voltage. The fraction increases sharply at the triggering voltage.

size $L = 80$, the triggering voltage saturates around $d = 40$. The model results clearly agree with the experimental data, shown in figure 5.8. This is a strong indication that the hypothesis formulated stating that current is initially blocked by impurities located at the junctions between nanowires is, in fact correct.

Networks generated by a random distribution of finite-sized rods in a two-dimensional plane have also been investigated. In this case, between every two rods in contact, a capacitor C_0 is placed. Once again the matrix $\mathbf{M}$ is constructed, and equation (5.6) is solved for $\mathbf{V}$. One of the edges of the two-dimensional area is chosen to represent the electrode, and rod crossing this specific edge are taken to be in contact with the electrode. A random rod a distance d from the electrode is chosen to represent the nanowire in contact with the AFM tip. Finally, the triggering voltage is calculated for that specific network. Several independent configurations are required in order to achieve good statistical averages, but the general behaviour of $V_{trigger}$ with the distance from the electrode shown in figure 5.14 was also observed. Due to its simplicity and computational inexpensive nature, the regular network case is preferred because it shows the same qualitative behaviour with much less computer power required.

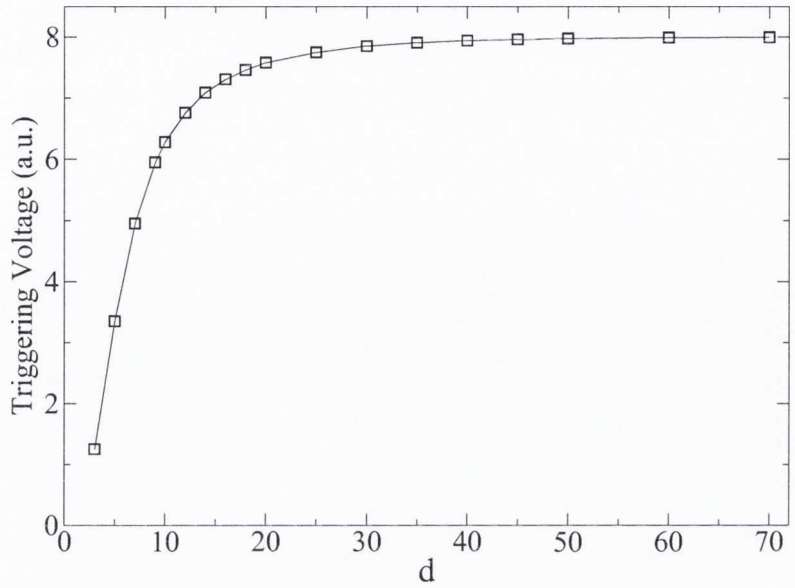

Figure 5.14: Triggering voltage as a function of the electrode–AFM tip distance d, for a square capacitive network with $L = 80$. Qualitative behaviour shows excellent agreement with experimental results in figure 5.8.

In this section, it has been shown how a simple model can be used to account for the onset of local electrical activation observed in silver nanowire networks. The modelling results validate the hypothesis that a triggering voltage is required in order to clear off impurities located at nanowire junctions. These impurities might have been leftover from the nanowire growth process, or from the deposition on the plastic substrate. In a similar fashion used to estimate the average junction resistance in carbon nanotube films, presented in chapter 3, it might be possible to calculate an average capacitance in silver nanowire films. The calculated average capacitance could be used to obtain information about the nature of the impurities, and the energy scales required to cause an electrical breakdown. This work is currently in progress.

5.3 Summary and Conclusions of the Chapter

The general methodology developed for the study of electronic transport on carbon nanotube networks has been applied to two related problems. First, the possibility

of using nanowire networks as a non-magnetic spacer between magnetic moments was considered. In typical magnetic–non-magnetic–magnetic layered systems, the interaction between magnetic layers is facilitated by conduction electrons of the non-magnetic spacer. The indirect exchange coupling between magnetic moments can be calculated through the Lloyd formula method, expressed in terms of specific Green function elements. In the case of magnetic impurities separated by nanowire networks, computer simulation results indicate that positive and negative couplings arise with approximately equal probability. When averaged over thousands of independent configurations, the calculated indirect coupling vanishes within error bars. Simulations with networks of increasing connectivity and increasing total number of wires return similar negative results.

On the second half of the chapter, the resistive network model presented in chapter 3 has been modified to account for hysteresis-type behaviour observed in current–voltage curves measured on silver nanowire networks. It has been hypothesised that a minimum voltage bias is required to remove impurities located at nanowire junctions. Once the triggering voltage is applied and the junctions are clean, the network conducts currents down to very low values of the bias voltage. The proposed modification in the model consists of considering a capacitive network, where every two adjacent nodes are connected by a capacitor C_0. A bias voltage is applied between one edge of the network and a single node, representing an electrode and an AFM tip respectively. Solving the linear equation to obtain the voltage at every node of the network, makes it possible to map the voltage difference on the terminals of each capacitor. A breakdown voltage for the capacitors is defined, such that any capacitor subject to a voltage higher than this one breaks down and becomes a conductor. It has been shown how the breakdown cloud expands on the networks as the electrode–AFM tip distance is varied, as well as the bias voltage. It was also shown that this simple model is capable of reproducing the experimentally observed behaviour of the triggering voltage increasing with the

distance. The agreement between experiment and simulation is a strong indication that the hypothesis originally raised is in fact correct, and impurities left over from the fabrication process block the conductance at nanowire junctions. The simulation results, in conjunction with experimental measurements, are currently under preparation for publication.

Chapter 6

Conclusions

Throughout the development of this work we have aimed at contributing to the understanding of electronic transport on carbon nanotube networks by means of computational models. A diligent effort has been made in order to design models capable of capturing all important features of the real physical systems, and which provide results in agreement with experimental studies. The computational models developed were explicitly designed to be combined with experimental results whenever possible in order to provide reliable estimates to quantities unavailable to experimental techniques, and to guide further experimental investigations on the development of highly conductive network films.

In chapter 1, carbon nanotubes were introduced along with their remarkable physical properties. Because of their mechanical strength and high electrical conductivity, carbon nanotubes appear as the natural material of choice for the development of flexible electronics. In particular, nanotube network films can be used to replace ITO in electronic displays, enabling the production of novel flexible devices. This particular application requires transparent CNT films with very high electrical conductivity, which has been very difficult to achieve in spite of the best efforts by research groups worldwide. The conductivity of CNT films is limited by the resistance at nanotube junctions and by the complex morphology of the

network. Chemical treatments can be applied to lower the junction resistance, but the role played by the network morphology needed to be clarified. Identifying a possible upper limit to the conductivity of nanotube films imposed by the network morphology was one of the major objectives of our work.

Chapter 2 introduced the tight binding method, which was chosen to describe the electronic structure of carbon nanotubes due to its low computational cost and suitability to carbon based materials. A tight binding Hamiltonian with one orbital per atom is sufficient to provide a good description of the electronic states near the Fermi energy of carbon based materials, which are the states responsible for the electronic transport properties. The Green function of a system was defined in terms of its Hamiltonian, and we have shown how it is related to the density of states of the system. The Kubo formula was derived in terms of specific Green function elements, and we have shown how it can be cast in a convenient form to calculate the conductance on nanotube networks. The theoretical tools presented in this chapter form the base of the microscopic electronic transport calculations presented in chapter 4.

A macroscopic model of nanotube networks was introduced in chapter 3. Our model is based on random networks of rigid rods and it can be applied to describe inter-tube connections on network films, as well as to describe the connections of nanotubes to metallic electrodes. We have found that the network connectivity scales universally with the volumetric fraction of the film occupied by rods, and with the aspect ratio of the rods. In spite of its simplicity, and not taking into account the bending and curling of nanotubes and bundles in real films, the model provides a good description of nanotube films within the range of interest. These findings are also important for the development of the microscopic transport simulations presented in chapter 4. By modelling nanotube films as resistive networks, we have shown how the conductance of the network scales with its volume fraction and with its density of junctions. Moreover, the percolation behaviour shown by

the network conductance is in agreement with independent experimental results reported by Hu et al. [77]. Comparing the conductance of model resistive networks with experimental measurements on nanotube films, we have estimated the average junction resistance, which was also found to be in agreement with independent measurements [73, 76]. Even though experiments show a large variation in the measured junction resistance, which depends on the diameter and chirality of nanotubes involved, the agreement between our results and the experiments is remarkable. The major results presented in this chapter have been published and can be found in reference [122].

The results of chapter 3 show how the network morphology affects the electronic transport properties of carbon nanotube films. However, in order to identify the existence of an upper limit to the conductivity of CNT networks, a microscopic investigation of nanotube films was required. On chapter 4, a microscopic model for quantum transport on carbon nanotube networks was presented, where individual nanotubes are described by a semi-empirical tight binding Hamiltonian, as introduced in chapter 2. In this model, a random network of tunnelling junctions is constructed by introducing electronic hopping terms connecting individual nanotubes, and the network conductance is calculated with the Kubo formula. A computationally efficient technique has been used to reduce the size of the Green function matrices, which allows for simulations with thousands of nanotubes, way beyond the reach of first principle calculations. Random networks are generated from the connectivities provided by the macroscopic model introduced in chapter 3, and both approaches (macroscopic and microscopic) are coupled into a single multiscale approach. This multiscale model was applied to networks in a ballistic transport regime, and by neglecting decoherence inducing scattering events, the upper bound for the conductivity of nanotube films was calculated. We have found that the maximum conductivity of a nanotube film scales universally with the density of the network, as well as with the average length and diameter of nanotubes in

the film. The best experimental results reported for the conductivity of nanotube films are only one order of magnitude lower than our theoretical prediction, and this is a clear indication that experiments are getting close to the limit of nanotube films conductivity. Our simulations show that metallic nanowire films might be better suited for applications in flexible displays, since the number of conducting channels in a nanowire increases with its diameter. The results presented in this chapter were published in references [153] and [154].

Chapter 5 presented further applications of the models presented in chapters 3 and 4. First, the microscopic approach of chapter 4 was applied to investigate if nanowire networks are capable of mediating magnetic coupling through their conduction electrons. Unfortunately, we have found that nanowire networks are not a good facilitating media for indirect exchange coupling. This negative result is probably caused by the very disordered nature of the networks. In the second part of the chapter, more successful results were obtained by modelling silver nanowire films as capacitive networks. Recent experiments have found that a minimum bias voltage is required to activate current pathways on newly produced silver nanowire films, and that once a region has been activated it continues to conduct electricity down to very low voltage biases. This hysteresis-like behaviour on current–voltage curves has led to the hypothesis that impurities located at nanowire junctions prevent electronic tunnelling, up to the point when charge build up at the junction causes an electric breakdown and burns the impurities. Motivated by these experimental results, the resistive network model of chapter 3 was used as a basis to develop a capacitive network model. Calculating the electrical potential at each node of the network, a complete mapping of the voltage difference across the capacitive network was produced. Defining a breakdown voltage for the capacitors in the network, we have shown that the voltage bias needed to activate current pathways in the network increases with the distance between the electrode and the AFM tip up to a saturation point, in good agreement with experiments. Our

results indicate that the original hypothesis is indeed valid, and are currently being prepared for publication, in conjunction with experimental data.

6.1 Possible Extensions of this Work

The models and results presented in this work are not meant to be the final word on the study of CNT network films. Instead, in many cases they are somewhat simple idealisations which are nonetheless capable of capturing the correct physical picture of each situation studied. The next few paragraphs outline some possible extensions which could be considered in order to guide further developments on the topics considered.

Modelling carbon nanotubes as interpenetrating rigid rods can be a very crude approximation, specially in cases where the volume fraction is high. The maximum volume fraction occupied by real objects inside a containing 3D space is limited to values smaller than the total volume of the enclosing space. The fact that real objects cannot freely overlap imposes constraints on the allowed positions of each new object added to the packing, which is neglected in our rigid rods model. Furthermore, carbon nanotubes are extended objects of very high aspect ratio and mechanical flexibility, which mean they can bend an curl in order to accommodate around certain constraints imposed by other nanotubes. The most realistic way to treat these features present in CNT films would be to consider the packing of non-interpenetrating flexible chain-like segments, similar to coarse-grained methods used in molecular dynamics simulations of polymeric systems and protein folding. This improvement could provide a more realistic description of how CNTs arrange in films of high volume fraction, but it is not expected to significantly improve the description of films with lower volume fraction.

In the introductory chapter of this thesis, it was argued how carbon nanotube films of different thickness can be applied to different types of electronic devices.

Very thin films can be used as transparent flexible transistors, films of intermediate thickness can be used as transparent electrodes on flexible electronic displays, and thick nanotube films can be used in energy storage devices. On very thin films, carbon nanotubes tend to align in layers parallel to the surface of the film, and each layer interacts mostly with the adjacent ones. In thicker films, layers are more interpenetrating and interactions between non-adjacent layers become more important. It would be interesting to perform a systematic theoretical study of the role played by the film thickness on its electronic transport properties. This study could be done considering the macroscopic model where the junction resistance is modelled by Ohmic resistors, and the microscopic one where the network connectivity is used to generate a random network of electronic hopping terms between individual nanotubes.

A recent study by Hicks et al. [168] has investigated electronic transport on graphene-based nanocomposites by employing a model similar to the ones used for carbon nanotube films. Instead of having sticks or rods representing CNTs, Hicks et al. have used sheets of varying aspect ratio to represent graphene flakes. It would be interesting to investigate if our method for calculating the resistance of disordered networks, introduced in chapter 3, would yield similar results to the ones obtained by Hicks et al. Furthermore, there have been indications in the recent literature that films made of a mixture of graphene flakes and carbon nanotubes would show better electrical conductivity than pure graphene films [169]. Building a macroscopic model capable of reproducing the geometric arrangement of nanotubes and flakes in such films would be an interesting way to theoretically investigate the performance of CNT–graphene mixed films.

A further aspect that would be of interest to consider, specially if one is interested in utilising nanotube films as flexible transistors, would be the investigation of electronic transport on networks composed of mixtures of metallic and semiconducting nanotubes [64]. In this case, the electronic hopping between different

species of carbon nanotubes would depend on the type of the tubes involved. In this situation, the presence of Schottky barriers at junctions between metallic and semiconducting nanotubes might play a significant role in the transport characteristics of the devices, and taking such effects into account in the simulations might prove a very challenging task.

On the development of the microscopic model presented in chapter 4, a very simple approach has been used to model the inter-tube electronic hopping, which considers only one carbon atom on each nanotube. The model could be further refined by including different types of hopping terms, possibly including more than one atom in each tube. Another way of accounting for more realistic inter-tube hopping terms would be to include parameters obtained from high precision *ab-initio* simulations in the tight binding Hamiltonian used. Performing such high-precision first principles calculations would be very time consuming, but the extra degree of sophistication introduced in the model should be capable of providing more realistic conductivity values, as opposed to concentrating on the upper limit as it was done in our work. This methodology presents an advantage over the one presented in chapter 3 because the electronic structure of individual CNTs is considered explicitly, rather than modelling CNTs as perfect conductors.

Even though an efficient computational method was developed in chapter 4, the final simulations with carbon nanotube networks were still limited with regard to the length of the nanotubes that composed the network. The Green function of finite nanotubes was calculated by a brute force numerical method, and even though efficient liner algebra libraries have been applied to this task, the size of the matrices involved is limited by the amount of memory available in the computers used. The existence of an analytical, or semi-analytical, expression for the Green function of finite carbon nanotubes would allow for the simulation of networks with much longer carbon nanotubes. These simulations could be used to independently verify the upper bound for the conductivity found in chapter 4

considering nanotubes of length comparable to the ones found in real experiments.

Finally, with regard to the capacitive networks studied in chapter 5, it is very desirable to perform systematic studies of finite-size effects on the transition from the non-conducting regime to the fully conducting one. Another natural extension of the model presented in chapter 5 is to consider fully disordered nanowire networks, generated by a macroscopic model similar to the one presented in chapter 3. A representation of the breakdown cloud obtained from a fully random model could, in principle, be compared directly with the AFM images obtained by experiments, and verify that this simple capacitive network model does capture all the important features present in real silver nanowire films.

Throughout this work we have made a diligent effort in order to develop the simplest models capable of capturing the correct physical picture in the systems considered. In many physical systems this approach would just be the usual search for the minimum effort method. In the case of the carbon nanotube networks considered in this thesis work, the approach through simple models is a fundamental requirement. Being in possession of a working model which reproduces, at least qualitatively, the observed behaviour of the system one can always introduce more levels of sophistication. Besides the suggestions outlined above, it is expected that the models presented in this thesis work can be further extend in a variety of ways. Each extension of the models could provide more accurate results, and perhaps show a better agreement with experimental data. However, to some extent at least, these would be refinements of the work presented here.

Bibliography

[1] H.W. Kroto, J.R. Heath, S.C. O'Brien, R.F. Curl, and R.E. Smalley. C60: Buckminsterfullerene. *Nature*, 318:162, 1985.

[2] S. Iijima. Helical microtubules of graphitic carbon. *Nature*, 354:56–58, 1991.

[3] R. Saito, M. Fujita, G. Dresselhaus, and M.S. Dresselhaus. Electronic structure of graphene tubules based on C60. *Physical Review B*, 46(3):1804, 1992.

[4] J.W.G. Wildoer, L.C. Venema, A.G. Rinzler, R.E. Smalley, and C. Dekker. Electronic structure of atomically resolved carbon nanotubes. *Nature*, 391:59, 1998.

[5] K.S. Novoselov, A.K. Geim, S.V. Morozov, D. Jiang, Y. Zhang, S.V. Dubonos, I.V. Grigorieva, and A.A. Firsov. Electric field effect in atomically thin carbon films. *Science*, 306:666–669, October 2004.

[6] R. Saito, G. Dresselhaus, and M.S. Dresselhaus. *Physical Properties of Carbon Nanotubes*. World Scientific Publishing Company, 1st edition, 1998.

[7] R.H. Baughman, A.A. Zakhidov, and W.A. de Heer. Carbon nanotubes-the route toward applications. *Science*, 297(5582):787–92, August 2002.

[8] A.K. Geim and K.S. Novoselov. The rise of graphene. *Nature materials*, 6(3):183–91, March 2007.

[9] Q. Cao and J.A. Rogers. Ultrathin Films of Single-Walled Carbon Nanotubes for Electronics and Sensors: A Review of Fundamental and Applied Aspects. *Advanced Materials*, 21:29–53, January 2009.

[10] A. Hirsch. The era of carbon allotropes. *Nature Materials*, 9(11):868–871, November 2010.

[11] S. Iijima and T. Ichihashi. Single-shell carbon nanotubes of 1-nm diameter. *Nature*, 363(6430):603, June 1993.

[12] D.S. Bethune, C.H. Klang, M.S. de Vries, G. Gorman, R. Savoy, J. Vazquez, and R. Beyers. Cobalt-catalysed growth of carbon nanotubes with single-atomic-layer walls. *Nature*, 363(6430):605, June 1993.

[13] S. Frank, P. Poncharal, Z. L. Wang, and W.A. de Heer. Carbon Nanotube Quantum Resistors. *Science*, 280(5370):1744–1746, June 1998.

[14] J. Kong, N.R. Franklin, C. Zhou, M.G. Chapline, S. Peng, K. Cho, and H. Dai. Nanotube Molecular Wires as Chemical Sensors. *Science*, 287(5453):622–625, January 2000.

[15] S.J. Tans, A.R.M. Verschueren, and C. Dekker. Room-temperature transistor based on a single carbon nanotube. *Nature*, 393:49, 1998.

[16] A. Javey, H. Kim, M. Brink, Q. Wang, A. Ural, J. Guo, P. McIntyre, P.L. McEuen, M. Lundstrom, and H. Dai. High-kappa dielectrics for advanced carbon-nanotube transistors and logic gates. *Nature materials*, 1(4):241, December 2002.

[17] A. Javey, J. Guo, Q. Wang, M. Lundstrom, and H. Dai. Ballistic carbon nanotube field-effect transistors. *Nature*, 424(6949):654, August 2003.

[18] S. Berber, Y.K. Kwon, and D. Tománek. Unusually High Thermal Conductivity of Carbon Nanotubes. *Physical Review Letters*, 84(20):4613–4616, May 2000.

[19] M. Fujii, X. Zhang, H. Xie, H. Ago, K. Takahashi, T. Ikuta, H. Abe, and T. Shimizu. Measuring the Thermal Conductivity of a Single Carbon Nanotube. *Physical Review Letters*, 95(6):065502, August 2005.

[20] P. Kim, L. Shi, A. Majumdar, and P.L. McEuen. Thermal Transport Measurements of Individual Multiwalled Nanotubes. *Physical Review Letters*, 87(21):215502, October 2001.

[21] S. Iijima, C. Brabec, A. Maiti, and J. Bernholc. Structural flexibility of carbon nanotubes. *The Journal of Chemical Physics*, 104(5):2089, 1996.

[22] A. Rochefort, P. Avouris, F. Lesage, and D.R. Salahub. Electrical and mechanical properties of distorted carbon nanotubes. *Physical Review B*, 60(19):13824–13830, November 1999.

[23] D. Tekleab, R. Czerw, D.L. Carroll, and P.M. Ajayan. Electronic structure of kinked multiwalled carbon nanotubes. *Applied Physics Letters*, 76(24):3594, 2000.

[24] P.M. Ajayan, L.S. Schadler, C. Giannaris, and A. Rubio. Single-Walled Carbon Nanotube-Polymer Composites: Strength and Weakness. *Advanced Materials*, 12(10):750–753, May 2000.

[25] E. Kymakis, I. Alexandou, and G.A.J. Amaratunga. Single-walled carbon nanotubepolymer composites: electrical, optical and structural investigation. *Synthetic Metals*, 127:59–62, March 2002.

[26] M.T. Byrne and Y.K. Gun'ko. Recent advances in research on carbon nanotube-polymer composites. *Advanced Materials*, 22:1672, May 2010.

[27] M.-F. Yu, B. Files, S. Arepalli, and R. Ruoff. Tensile Loading of Ropes of Single Wall Carbon Nanotubes and their Mechanical Properties. *Physical Review Letters*, 84(24):5552, June 2000.

[28] A. Wall, J.N. Coleman, and M.S. Ferreira. Physical mechanism for the mechanical reinforcement in nanotube-polymer composite materials. *Physical Review B*, 71(12):125421, March 2005.

[29] J.N. Coleman, U. Khan, W.J. Blau, and Y.K. Gun'ko. Small but strong: A review of the mechanical properties of carbon nanotubepolymer composites. *Carbon*, 44(9):1624–1652, August 2006.

[30] J.N. Coleman, M. Cadek, K.P. Ryan, A. Fonseca, J.B. Nagy, W.J. Blau, and M.S. Ferreira. Reinforcement of polymers with carbon nanotubes. The role of an ordered polymer interfacial region. Experiment and modeling. *Polymer*, 47(26):8556–8561, December 2006.

[31] W.A. de Heer, W.S. Bacsa, A. Châtelain, T. Gerfin, R. Humphrey-Baker, L. Forro, and D. Ugarte. Aligned carbon nanotube films: production and optical and electronic properties. *Science*, 268(5212):845, May 1995.

[32] W.A. de Heer, A. Chatelain, and D. Ugarte. A Carbon Nanotube Field-Emission Electron Source. *Science*, 270(5239):1179, November 1995.

[33] Z.F. Ren, Z.P. Huang, J.W. Xu, J.H. Wang, P. Bush, M.P. Siegal, and P.N. Provencio. Synthesis of large arrays of well-aligned carbon nanotubes on glass. *Science*, 282(5391):1105, November 1998.

[34] K. Xiao, Y. Liu, P. Hu, G. Yu, X. Wang, and D. Zhu. High-mobility thin-film transistors based on aligned carbon nanotubes. *Applied Physics Letters*, 83(1):150, 2003.

[35] C. Kocabas, N. Pimparkar, O Yesilyurt, S.J. Kang, M.A. Alam, and J.A. Rogers. Experimental and theoretical studies of transport through large scale, partially aligned arrays of single-walled carbon nanotubes in thin film type transistors. *Nano letters*, 7(5):1195, May 2007.

[36] S.J. Kang, C. Kocabas, T. Ozel, M. Shim, N. Pimparkar, M.A. Alam, S.V. Rotkin, and J.A. Rogers. High-performance electronics using dense, perfectly aligned arrays of single-walled carbon nanotubes. *Nature Nanotechnology*, 2(4):230, April 2007.

[37] E.S. Snow, J.P. Novak, P.M. Campbell, and D. Park. Random networks of carbon nanotubes as an electronic material. *Applied Physics Letters*, 82(13):2145, 2003.

[38] K. Bradley, J.C.P. Gabriel, and G. Gruner. Flexible Nanotube Electronics. *Nano Letters*, 3(10):1353–1355, October 2003.

[39] T. Takenobu, T. Takahashi, T. Kanbara, K. Tsukagoshi, Y. Aoyagi, and Y. Iwasa. High-performance transparent flexible transistors using carbon nanotube films. *Applied Physics Letters*, 88(3):033511, 2006.

[40] J. Lewis, S. Grego, B. Chalamala, E. Vick, and D. Temple. Highly flexible transparent electrodes for organic light-emitting diode-based displays. *Applied Physics Letters*, 85(16):3450, 2004.

[41] C.M. Aguirre, S. Auvray, S. Pigeon, R. Izquierdo, P. Desjardins, and R. Martel. Carbon nanotube sheets as electrodes in organic light-emitting diodes. *Applied Physics Letters*, 88(18):183104, 2006.

[42] E. Bekyarova, M.E. Itkis, N. Cabrera, B. Zhao, A. Yu, J. Gao, and R.C. Haddon. Electronic properties of single-walled carbon nanotube networks. *Journal of the American Chemical Society*, 127(16):5990, April 2005.

[43] E. Artukovic, M. Kaempgen, D.S. Hecht, S. Roth, and G. Gruner. Transparent and flexible carbon nanotube transistors. *Nano letters*, 5(4):757, April 2005.

[44] Q. Cao, S.-H. Hur, Z.-T. Zhu, Y.G. Sun, C.-J. Wang, M.A. Meitl, M. Shim, and J.A. Rogers. Highly Bendable, Transparent Thin-Film Transistors That Use Carbon-Nanotube-Based Conductors and Semiconductors with Elastomeric Dielectrics. *Advanced Materials*, 18(3):304–309, February 2006.

[45] H.E. Unalan, G. Fanchini, A. Kanwal, A. Du Pasquier, and M. Chhowalla. Design criteria for transparent single-wall carbon nanotube thin-film transistors. *Nano letters*, 6(4):677, April 2006.

[46] D.S. Hecht, L. Hu, and G. Gruner. Conductivity scaling with bundle length and diameter in single walled carbon nanotube networks. *Applied Physics Letters*, 89(13):133112, 2006.

[47] A. Behnam, L. Noriega, Y. Choi, Z. Wu, A.G. Rinzler, and A. Ural. Resistivity scaling in single-walled carbon nanotube films patterned to submicron dimensions. *Applied Physics Letters*, 89(9):093107, 2006.

[48] A. Kumar and C. Zhou. The race to replace tin-doped indium oxide: which material will win? *ACS nano*, 4(1):11, January 2010.

[49] C. Du and N. Pan. High power density supercapacitor electrodes of carbon nanotube films by electrophoretic deposition. *Nanotechnology*, 17(21):5314–5318, November 2006.

[50] J.E. Trancik, S.C. Barton, and J. Hone. Transparent and catalytic carbon nanotube films. *Nano letters*, 8(4):982, April 2008.

[51] A.-Y. Lo, C.-S. Sun, W.-S. Tseng, and C.-T. Kuo. Process and properties of the carbon nanotube assisted LiCoO[sub 2] thin-film battery electrode

by pulsed laser deposition. *Journal of Vacuum Science & Technology B: Microelectronics and Nanometer Structures*, 27(6):3067, 2009.

[52] J.N. Coleman, A. Fleming, S. Maier, S. O'Flaherty, A.I. Minett, M.S. Ferreira, S. Hutzler, and W.J. Blau. Binding Kinetics and SWNT Bundle Dissociation in Low Concentration PolymerNanotube Dispersions. *The Journal of Physical Chemistry B*, 108(11):3446–3450, March 2004.

[53] Y. Maeda, S.-i. Kimura, Y. Hirashima, M. Kanda, Y. Lian, T. Wakahara, T. Akasaka, T. Hasegawa, H. Tokumoto, T. Shimizu, H. Kataura, Y. Miyauchi, S. Maruyama, K. Kobayashi, and S. Nagase. Dispersion of Single-Walled Carbon Nanotube Bundles in Nonaqueous Solution. *The Journal of Physical Chemistry B*, 108(48):18395–18397, December 2004.

[54] J.-W. Song, J. Kim, Y.-H. Yoon, B.-S. Choi, J.-H. Kim, and C.-S. Han. Inkjet printing of single-walled carbon nanotubes and electrical characterization of the line pattern. *Nanotechnology*, 19(9):095702, March 2008.

[55] S. De and J.N. Coleman. Are there fundamental limitations on the sheet resistance and transmittance of thin graphene films? *ACS nano*, 4(5):2713–20, May 2010.

[56] E.M. Doherty, S. De, P.E. Lyons, A. Shmeliov, P.N. Nirmalraj, V. Scardaci, J. Joimel, W.J. Blau, J.J. Boland, and J.N. Coleman. The spatial uniformity and electromechanical stability of transparent, conductive films of single walled nanotubes. *Carbon*, 47(10):2466–2473, August 2009.

[57] C.L. Pint, Y.Q. Xu, E. Morosan, and R.H. Hauge. Alignment dependence of one-dimensional electronic hopping transport observed in films of highly aligned, ultralong single-walled carbon nanotubes. *Applied Physics Letters*, 94(18):182107, 2009.

[58] O.E. Omel'Yanovskii, V.I. Tsebro, O.I. Lebedev, A.N. Kiselev, V.I. Bondarenko, N.A. Kiselev, Z.J. Kosakovskaja, and L.A. Chernozatonskii. Temperature-dependence of the resistivity and structure of carbon nanotube films containing various kinds of tubules. *JETP LETTERS*, 62(6):503, 1995.

[59] N.F. Mott. *Conduction in Non-Crystalline Materials.* Oxford University Press, New York, 1987.

[60] P.G. Collins, M.S. Arnold, and P. Avouris. Engineering carbon nanotubes and nanotube circuits using electrical breakdown. *Science*, 292(5517):706, April 2001.

[61] S. Kumar, J.Y. Murthy, and M.A. Alam. Percolating conduction in finite nanotube networks. *Physical review letters*, 95(6):66802, 2005.

[62] S. Kumar, N. Pimparkar, J.Y. Murthy, and M.A. Alam. Theory of transfer characteristics of nanotube network transistors. *Applied Physics Letters*, 88:123505, 2006.

[63] N. Pimparkar, J. Guo, and M.A. Alam. Performance Assessment of Subpercolating Nanobundle Network Thin-Film Transistors by an Analytical Model. *IEEE Transactions on Electron Devices*, 54(4):637, April 2007.

[64] M.A. Topinka, M.W. Rowell, D. Goldhaber-Gordon, M.D. McGehee, D.S. Hecht, and G. Gruner. Charge transport in interpenetrating networks of semiconducting and metallic carbon nanotubes. *Nano letters*, 9(5):1866, May 2009.

[65] A. Behnam, J. Guo, and A. Ural. Effects of nanotube alignment and measurement direction on percolation resistivity in single-walled carbon nanotube films. *Journal of Applied Physics*, 102(4):044313, 2007.

[66] S. White, B. DiDonna, M. Mu, T. Lubensky, and K. Winey. Simulations and electrical conductivity of percolated networks of finite rods with various degrees of axial alignment. *Physical Review B*, 79(2):024301, January 2009.

[67] D.A. Jack, C.-S. Yeh, Z. Liang, S. Li, J.G. Park, and J.C. Fielding. Electrical conductivity modeling and experimental study of densely packed SWCNT networks. *Nanotechnology*, 21(19):195703, May 2010.

[68] J. Tersoff. Contact resistance of carbon nanotubes. *Applied Physics Letters*, 74(15):2122, 1999.

[69] R. Jackson and S. Graham. Specific contact resistance at metal/carbon nanotube interfaces. *Applied Physics Letters*, 94(1):012109, 2009.

[70] H. Xu, L. Chen, L. Hu, and N. Zhitenev. Contact resistance of flexible, transparent carbon nanotube films with metals. *Applied Physics Letters*, 97(14):143116, 2010.

[71] S.H. Han, S.H. Lee, J.H. Hur, J. Jang, Y.-b. Park, G. Irvin, and P. Drzaic. Contact resistance between Au and solution-processed CNT. *Solid-State Electronics*, 54(5):586–589, May 2010.

[72] Z. Yao, H.W.C. Postma, L. Balents, and C. Dekker. Carbon nanotube intramolecular junctions. *Nature*, 402(November):273–276, 1999.

[73] M.S. Fuhrer, J. Nygard, L. Shih, M. Forero, Y.G. Yoon, M.S.C. Mazzoni, H.J. Choi, J. Ihm, S.G. Louie, A. Zettl, and P.L. McEuen. Crossed nanotube junctions. *Science*, 288:494–497, April 2000.

[74] H. Stahl, J. Appenzeller, R. Martel, P. Avouris, and B. Lengeler. Intertube coupling in ropes of single-wall carbon nanotubes. *Physical review letters*, 85(24):5186, December 2000.

[75] Y.G. Yoon, M. Mazzoni, H. Choi, J. Ihm, and S.G. Louie. Structural Deformation and Intertube Conductance of Crossed Carbon Nanotube Junctions. *Physical Review Letters*, 86(4):688–691, January 2001.

[76] P.N. Nirmalraj, P.E. Lyons, S. De, J.N. Coleman, and J.J. Boland. Electrical connectivity in single-walled carbon nanotube networks. *Nano letters*, 9(11):3890, November 2009.

[77] L. Hu, D.S. Hecht, and G. Gruner. Percolation in Transparent and Conducting Carbon Nanotube Networks. *Nano Letters*, 4(12):2513–2517, December 2004.

[78] F.M. Blighe, Y.R. Hernandez, W.J. Blau, and J.N. Coleman. Observation of Percolation-like Scaling Far from the Percolation Threshold in High Volume Fraction, High Conductivity Polymer-Nanotube Composite Films. *Advanced Materials*, 19(24):4443–4447, December 2007.

[79] S. De, P.J. King, P.E. Lyons, U. Khan, and J.N. Coleman. Size effects and the problem with percolation in nanostructured transparent conductors. *ACS nano*, 4(12):7064, December 2010.

[80] Z. Wu, Z. Chen, X. Du, J.M. Logan, J. Sippel, M. Nikolou, K. Kamaras, J.R. Reynolds, D.B. Tanner, A.F. Hebard, and A.G. Rinzler. Transparent, conductive carbon nanotube films. *Science*, 305(5688):1273, August 2004.

[81] M. Dressel and G. Gruner. *Electrodynamics of Solids: Optical Properties of Electrons in Matter*. Cambridge University Press, 2002.

[82] S. De, T.M. Higgins, P.E. Lyons, E.M. Doherty, P.N. Nirmalraj, W.J. Blau, J.J. Boland, and J.N. Coleman. Silver Nanowire Networks as Flexible, Transparent, Conducting Films: Extremely High DC to Optical Conductivity Ratios. *ACS nano*, 3(7):1767–1774, June 2009.

[83] B.B. Parekh, G. Fanchini, G. Eda, and M. Chhowalla. Improved conductivity of transparent single-wall carbon nanotube thin films via stable postdeposition functionalization. *Applied Physics Letters*, 90(12):121913, 2007.

[84] L. Hu, D.S. Hecht, and G. Gruner. Carbon Nanotube Thin Films: Fabrication, Properties, and Applications. *Chemical Reviews*, 110(10):5790–5844, July 2010.

[85] B. Ruzicka and L. Degiorgi. Optical and dc conductivity study of potassium-doped single-walled carbon nanotube films. *Physical Review B*, 61(4):R2468–R2471, January 2000.

[86] H.-Z. Geng, K.K. Kim, K.P. So, Y.S. Lee, Y. Chang, and Y.H. Lee. Effect of acid treatment on carbon nanotube-based flexible transparent conducting films. *Journal of the American Chemical Society*, 129(25):7758, June 2007.

[87] J.C. Slater and G.F. Koster. Simplified LCAO Method for the Periodic Potential Problem. *Physical Review*, 94(6):1498–1524, June 1954.

[88] J.C. Charlier, X. Blase, and S. Roche. Electronic and transport properties of nanotubes. *Reviews of Modern Physics*, 79(2):677–732, May 2007.

[89] E.N. Economou. *Green's functions in quantum physics.* Springer, Berlin, third edition, 2006.

[90] C.J. Chen. *Introduction to Scanning Tunneling Microscopy.* Oxford University Press, second edition, 2008.

[91] S. Datta. *Electronic transport in mesoscopic systems.* Cambridge University Press, Cambridge, UK, 1997.

[92] S. Datta. *Quantum transport: atom to transistor.* Cambridge University Press, Cambridge, UK, 2005.

[93] N.S. Wingreen, A.-P. Jauho, and Y. Meir. Time-dependent transport through a mesoscopic structure. *Physical Review B*, 48:8487, 1993.

[94] M. Brandbyge, J.-L. Mozos, P. Ordejon, J. Taylor, and K. Stokbro. Density-functional method for nonequilibrium electron transport. *Physical Review B*, 65(16):165401, March 2002.

[95] A.R. Rocha, V.M. García-Suárez, S.W. Bailey, C.J. Lambert, J. Ferrer, and S. Sanvito. Towards molecular spintronics. *Nature materials*, 4(4):335, April 2005.

[96] M.S. Ferreira, G.E.W. Bauer, and C.P.A. Wapenaar. Recursive Green functions technique applied to the propagation of elastic waves in layered media. *Ultrasonics*, 40(1-8):355–9, May 2002.

[97] R. Kubo. Statistical-Mechanical Theory of Irreversible Processes. I. General Theory and Simple Applications to Magnetic and Conduction Problems. *Journal of the Physical Society of Japan*, 12(6):570–586, June 1957.

[98] P.A. Lee and D.S. Fisher. Anderson Localization in Two Dimensions. *Physical Review Letters*, 47(12):882, 1981.

[99] J. Mathon, A. Umerski, and M. Villeret. Oscillations with Co and Cu thickness of the current-perpendicular-to-plane giant magnetoresistance of a Co/Cu/Co (001) trilayer. *Physical Review B*, 55(21):14378, 1997.

[100] D.S. Fisher and P.A. Lee. Relation between conductivity and transmission matrix. *Physical Review B*, 23(12):6851, June 1981.

[101] L. Chico, L. Benedict, S.G. Louie, and M. Cohen. Quantum conductance of carbon nanotubes with defects. *Physical Review B*, 54(4):2600, July 1996.

[102] D. Grimm, A. Latge, R.B. Muniz, and M.S. Ferreira. Transport suppression in polymer-doped zigzag carbon nanotubes. *Physical Review B*, 71(11):113408, 2005.

[103] Y. Cui, Q. Wei, H. Park, and C.M. Lieber. Nanowire nanosensors for highly sensitive and selective detection of biological and chemical species. *Science*, 293(5533):1289–92, August 2001.

[104] C. Caroli, R. Combescot, P. Nozieres, and D. Saint-James. Direct calculation of the tunnelling current. *Journal of Physics C: Solid State Physics*, 4:916, 1971.

[105] C. Caroli, R. Combescot, P. Lederer, P. Nozieres, and D. Saint-James. A direct calculation of the tunnelling current II . Free electron description. *Journal of Physics C: Solid State Physics*, 4:2598, 1971.

[106] R. Combescot. A direct calculation of the tunneling current III. Effect of localized impurity states in the barrier. *Journal of Physics C: Solid State Physics*, 4:2611, 1971.

[107] C. Caroli, R. Combescot, P. Nozieres, and D. A direct calculation of the tunnelling current: IV. Electron-phonon interaction effects. *Journal of Physics C: Solid State Physics*, 5:21, 1972.

[108] M.B. Nardelli. Electronic transport in extended systems: Application to carbon nanotubes. *Physical Review B*, 60(11):7828–7833, 1999.

[109] H. Dai, E.W. Wong, and C.M. Lieber. Probing Electrical Transport in Nanomaterials: Conductivity of Individual Carbon Nanotubes. *Science*, 272(5261):523–526, April 1996.

[110] L. Chico, V. Crespi, L. Benedict, S.G. Louie, and M. Cohen. Pure Carbon Nanoscale Devices: Nanotube Heterojunctions. *Physical Review Letters*, 76(6):971, February 1996.

[111] Q. Cao, H.-S. Kim, N. Pimparkar, J.P. Kulkarni, C. Wang, M. Shim, K. Roy, M.A. Alam, and J.A. Rogers. Medium-scale carbon nanotube thin-film integrated circuits on flexible plastic substrates. *Nature*, 454:495, July 2008.

[112] A. Rochefort and P. Avouris. Electron Interference Effects on the Conductance of Doped Carbon Nanotubes. *The Journal of Physical Chemistry A*, 104(44):9807–9811, November 2000.

[113] D.C. DePackh. A Resistor Network for the Approximate Solution of the Laplace Equation. *Review of Scientific Instruments*, 18(10):798, 1947.

[114] R.E. Aitchison. Resistance between Adjacent Points of Liebman Mesh. *American Journal of Physics*, 32(7):566, 1964.

[115] M. Jevons. Square lattice resistance networks with diagonal elements. *Journal of Scientific Instruments*, 44(7):514–516, July 1967.

[116] F.J. Bartis. Let's Analyze the Resistance Lattice. *American Journal of Physics*, 35(4):354, 1967.

[117] G. Venezian. On the resistance between two points on a grid. *American Journal of Physics*, 62(11):1000, 1994.

[118] D. Atkinson and F.J. Van Steenwijk. Innite resistive lattices. *American Journal of Physics*, 67(6):486–492, 1999.

[119] J. Cserti. Application of the lattice Greens function for calculating the resistance of an infinite network of resistors. *American Journal of Physics*, 68(10):896, 2000.

[120] R. Albert and A.L. Barabási. Statistical mechanics of complex networks. *Reviews of modern physics*, 74(1):47, 2002.

[121] F.M. Blighe, P.E. Lyons, S. De, W.J. Blau, and J.N. Coleman. On the factors controlling the mechanical properties of nanotube films. *Carbon*, 46:41–47, January 2008.

[122] P.E. Lyons, S. De, F.M. Blighe, V. Nicolosi, L.F.C. Pereira, M.S. Ferreira, and J.N. Coleman. The relationship between network morphology and conductivity in nanotube films. *Journal of Applied Physics*, 104(4):044302, 2008.

[123] S. Kirkpatrick. Percolation and Conduction. *Reviews of Modern Physics*, 45(4):574–588, October 1973.

[124] B. Denardo, J. Earwood, and V. Sazonova. Experiments with electrical resistive networks. *American Journal of Physics*, 67:981, 1999.

[125] J. Cserti, G. David, and A. Piroth. Perturbation of infinite networks of resistors. *American Journal of Physics*, 70(2):153, July 2002.

[126] C. Li and T.-W. Chou. A direct electrifying algorithm for backbone identification. *Journal of Physics A: Mathematical and Theoretical*, 40(49):14679–14686, December 2007.

[127] D. Stauffer and A. Aharony. *Introduction to percolation theory*. Taylor & Francis, 1992.

[128] G. Pike and C. Seager. Percolation and conductivity: A computer study. I. *Physical Review B*, 10(4):1421–1434, August 1974.

[129] C. Seager and G. Pike. Percolation and conductivity: A computer study. II. *Physical Review B*, 10(4):1435–1446, August 1974.

[130] S. Munson-McGee. Estimation of the critical concentration in an anisotropic percolation network. *Physical Review B*, 43(4):3331–3336, February 1991.

[131] A. Celzard, E. McRae, C. Deleuze, M. Dufort, G. Furdin, and J.F. Marêché. Critical concentration in percolating systems containing a high-aspect-ratio filler. *Physical Review B*, 53(10):6209–6214, March 1996.

[132] M.C. LeMieux, M.E. Roberts, S. Barman, Y.W. Jin, J.M. Kim, and Z. Bao. Self-sorted, aligned nanotube networks for thin-film transistors. *Science*, 321(5885):101, July 2008.

[133] A.D. Pasquier, H.E. Unalan, A. Kanwal, S. Miller, and M. Chhowalla. Conducting and transparent single-wall carbon nanotube electrodes for polymer-fullerene solar cells. *Applied Physics Letters*, 87(20):203511, 2005.

[134] L. Xiao, Z. Chen, C. Feng, L. Liu, Z.-Q. Bai, Y. Wang, L. Qian, Y. Zhang, Q. Li, K. Jiang, and S. Fan. Flexible, stretchable, transparent carbon nanotube thin film loudspeakers. *Nano letters*, 8(12):4539, December 2008.

[135] A. Goldoni, R. Larciprete, L. Petaccia, and S. Lizzit. Single-wall carbon nanotube interaction with gases: sample contaminants and environmental monitoring. *Journal of the American Chemical Society*, 125(37):11329, September 2003.

[136] M.Z. Atashbar, B.E. Bejcek, and S. Singamaneni. Carbon nanotube network-based biomolecule detection. *IEEE Sensors Journal*, 6(3):524–528, June 2006.

[137] M.E. Roberts, M.C. LeMieux, and Z. Bao. Sorted and aligned single-walled carbon nanotube networks for transistor-based aqueous chemical sensors. *ACS nano*, 3(10):3287–93, October 2009.

[138] M. Yang, D.H. Kim, W.S. Kim, T.J. Kang, B.Y. Lee, S. Hong, Y.H. Kim, and S.H. Hong. H(2) sensing characteristics of SnO(2) coated single wall carbon nanotube network sensors. *Nanotechnology*, 21(21):215501, May 2010.

[139] M.W. Rowell, M.A. Topinka, M.D. McGehee, H.J. Prall, G. Dennler, N.S. Sariciftci, L. Hu, and G. Gruner. Organic solar cells with carbon nanotube network electrodes. *Applied Physics Letters*, 88(23):233506, 2006.

[140] S.I. Cho, W.J. Kwon, S.-J. Choi, P. Kim, S.-A. Park, J. Kim, S.J. Son, R. Xiao, S.-H. Kim, and S.B. Lee. Nanotube-Based Ultrafast Electrochromic Display. *Advanced Materials*, 17(2):171–175, January 2005.

[141] T. Sekitani, H. Nakajima, H. Maeda, T. Fukushima, T. Aida, K. Hata, and T. Someya. Stretchable active-matrix organic light-emitting diode display using printable elastic conductors. *Nature Materials*, 8(6):494, June 2009.

[142] X. Wang, L. Zhi, and K. Müllen. Transparent, conductive graphene electrodes for dye-sensitized solar cells. *Nano letters*, 8(1):323, January 2008.

[143] D. Mowbray, C. Morgan, and K.S. Thygesen. Influence of O2 and N2 on the conductivity of carbon nanotube networks. *Physical Review B*, 79(19):195431, May 2009.

[144] S. Latil, S. Roche, D. Mayou, and J.C. Charlier. Mesoscopic Transport in Chemically Doped Carbon Nanotubes. *Physical Review Letters*, 92(25):256805, June 2004.

[145] C.G. Rocha, A. Wall, A.R. Rocha, and M.S. Ferreira. Modelling the effect of randomly dispersed adatoms on carbon nanotubes. *Journal of Physics: Condensed Matter*, 19:346201, August 2007.

[146] M.S. Ferreira. *Oscillatory Interlayer Exchange Coupling in Metallic Magnetic Multilayers.* Phd thesis, Imperial College of Science, Technology and Medicine, 1997.

[147] A.T. Costa, D.F. Kirwan, and M.S. Ferreira. Indirect exchange coupling between magnetic adatoms in carbon nanotubes. *Physical Review B*, 72(8):085402, August 2005.

[148] D.F. Kirwan. *Theoretical Studies of Carbon Nanotubes Interacting with Magnetic Atoms.* PhD thesis, Trinity College Dublin, 2009.

[149] J. Mathon. Tight-binding theory of tunneling giant magnetoresistance. *Physical Review B*, 56(18):11810, 1997.

[150] A.P. Sutton. *Electronic Structure of Materials.* Oxford University Press, Oxford, 1993.

[151] P. Erdos and A. Renyi. On random graphs I. *Publicationes Mathematicae (Debrecen)*, 6:290–297, 1959.

[152] D.H. Shin, H.C. Shim, J.-W. Song, S. Kim, and C.-S. Han. Conductivity of films made from single-walled carbon nanotubes in terms of bundle diameter. *Scripta Materialia*, 60(8):607–610, April 2009.

[153] L.F.C. Pereira, C.G. Rocha, A. Latge, J.N. Coleman, and M.S. Ferreira. Upper bound for the conductivity of nanotube networks. *Applied Physics Letters*, 95(12):123106, 2009.

[154] L.F.C. Pereira, C.G. Rocha, A. Latge, and M.S. Ferreira. A computationally efficient method for calculating the maximum conductance of disordered networks: Application to one-dimensional conductors. *Journal of Applied Physics*, 108(10):103720, 2010.

[155] M.A. Ruderman and C. Kittel. Indirect Exchange Coupling of Nuclear Magnetic Moments by Conduction Electrons. *Physical Review*, 96(1):99–102, October 1954.

[156] C. Carbone and S. Alvarado. Antiparallel coupling between Fe layers separated by a Cr interlayer: Dependence of the magnetization on the film thickness. *Physical Review B*, 36(4):2433–2435, August 1987.

[157] M. Baibich, J. Broto, A. Fert, F. Van Dau, F. Petroff, P. Etienne, G. Creuzet, A. Friederich, and J. Chazelas. Giant Magnetoresistance of (001)Fe/(001)Cr Magnetic Superlattices. *Physical Review Letters*, 61(21):2472–2475, November 1988.

[158] G. Binasch, P. Grünberg, F. Saurenbach, and W. Zinn. Enhanced magnetoresistance in layered magnetic structures with antiferromagnetic interlayer exchange. *Physical Review B*, 39(7):4828–4830, March 1989.

[159] F. Kuemmeth, S. Ilani, D.C. Ralph, and P.L. McEuen. Coupling of spin and orbital motion of electrons in carbon nanotubes. *Nature*, 452(7186):448–52, March 2008.

[160] O. Céspedes, M.S. Ferreira, S. Sanvito, M. Kociak, and J.M.D. Coey. Contact induced magnetism in carbon nanotubes. *Journal of Physics: Condensed Matter*, 16(10):L155–L161, March 2004.

[161] P. Lloyd. Wave propagation through an assembly of spheres: II. The density of single-particle eigenstates. *Proceedings of the Physical Society*, 90(1):207–216, January 1967.

[162] P. Lloyd and P.V. Smith. Multiple scattering theory in condensed materials. *Advances in Physics*, 21(89):69–142, January 1972.

[163] R. Zeller. An elementary derivation of Lloyd s formula valid for full-potential multiple-scattering theory. *Journal of Physics: Condensed Matter*, 16:6453–6468, September 2004.

[164] C.G. Rocha and M.S. Ferreira. A simple theoretical approach to designing nanotube-based sensors. *physica status solidi (b)*, 8:doi:10.1002/pssb.201046015, August 2010.

[165] J. dAlbuquerque E Castro, M.S. Ferreira, and R.B. Muniz. Theory of the exchange coupling in magnetic metallic multilayers. *Physical Review B*, 49(22):16062–16065, June 1994.

[166] D.F. Kirwan, C.G. Rocha, A.T. Costa, and M.S. Ferreira. Sudden decay of indirect exchange coupling between magnetic atoms on carbon nanotubes. *Physical Review B*, 77(8):085432, February 2008.

[167] D.F. Kirwan, C.G. Rocha, A.T. Costa, and M.S. Ferreira. Suppression of long ranged coupling between magnetic atoms on carbon nanotubes. *physica status solidi (b)*, 245(10):2169–2172, October 2008.

[168] J. Hicks, A. Behnam, and A. Ural. A computational study of tunneling-percolation electrical transport in graphene-based nanocomposites. *Applied Physics Letters*, 95(21):213103, 2009.

[169] G. Xin, W. Hwang, N. Kim, S.M. Cho, and H. Chae. A graphene sheet exfoliated with microwave irradiation and interlinked by carbon nanotubes for high-performance transparent flexible electrodes. *Nanotechnology*, 21(40):405201, October 2010.